DISSERTATION

submitted to the
Combined Faculty of Natural Sciences and Mathematics
of Heidelberg University, Germany
for the degree of
Doctor of Natural Sciences

Put forward by
Jonas Tauch
born in: Tübingen, Germany

Oral examination: June 2nd, 2021

NEW APPROACHES FOR COOLING MOLECULAR ANIONS TO THE KELVIN RANGE

Referees: Prof. Dr. Matthias Weidemüller
Prof. Dr. Andreas Wolf

Abstract. This thesis presents two anion cooling techniques based on their interaction with photons or ultracold atoms, pushing the frontier of anion cooling beyond state-of-the-art experiments. A hybrid atom-ion trap (HAITrap) is presented, combining an octupole radio frequency (rf) trap and a dark spontaneous-force optical trap for rubidium. The anions and atoms are probed via photodetachment tomography, time-of-flight thermometry and saturation absorption imaging, respectively. The anion photodetachment via a focused far-threshold laser beam removes anions selectively by their energy. This thesis reports forced evaporative cooling of OH^- via dynamically moving the beam, below 4 Kelvin in 2 seconds. A derived thermodynamic model describes the evolution of anion temperature and number, including the importance of ion-ion thermalization and resulting rf-heating in such traps. It shows experimental and theoretical framework to prepare any anionic specie in a vast energy range. This thesis also reports the sympathetic cooling and the collision dynamics of anions with ultracold rubidium in a HAITrap. The cooling is experimentally demonstrated to $30(2)$ Kelvin for O^- and $135(8)$ Kelvin for OH^-. The different cooling behavior is explained by their dissimilar loss channels, which are identified and quantified. These limitations can be overcome in future experiments, providing a tool to cool anions translationally and internally.

Zusammenfassung. In dieser Arbeit werden zwei Kühltechniken für Anionen vorgestellt, die auf deren Wechselwirkung mit Photonen oder ultrakalten Atomen beruhen und die Kühlung unter das bisherige Limit ermöglicht. Es wird eine Hybrid-Atom-Ionenfalle (HAITrap) vorgestellt, die eine Oktupol-Radiofrequenzfall und eine dunkle magneto-optische Falle für Rubidiumatome kombiniert. Die Anionen und Atome werden mittels *Photodetachment*-Tomographie, Flugzeitthermometrie beziehungsweise Sättigungsabsorptionsabbildung charakterisiert. Durch einen fokussierten Laserstrahl über der *Photodetachment*schwelle können Anionen energieabhängig aus der Falle entfernt werden. Diese Arbeit berichtet über erzwungen Verdunstungskühlung von OH^- durch Bewegen des Laserstrahls in Richtung der Fallenmitte zu einer Temperatur unter 4 Kelvin in 2 Sekunden. Ein hergeleitetes thermodynamisches Modell beschreibt die Änderung der Anionentemperatur und -zahl. Das Modell hebt die Wichtigkeit der Ionen-Ionen-Thermalisierung und des daraus resultierenden Radiofrequenzheizens in diesen Ionenfallen hervor. Es wird experimentell und theoretisch gezeigt, dass die Präparation jeglicher Anionen in einem großen Energiebereich möglich ist. Die Arbeit berichtet ebenfalls über sympathetisches Kühlen und Kollisionsdynamiken von Anionen mit ultrakaltem Rubidium in einer HAITrap. Die Kühlung wird experimentell bis 30 Kelvin für O^- und 135 Kelvin für OH^- demonstriert. Die unterschiedliche Kühldynamik erklärt sich durch unterschiedliche Verlustkanäle, die identifiziert und quantifiziert wurden. Die gezeigte Limitierung sympathetischen Kühlens kann in zukünftigen Experimenten überwunden werden, wodurch Kühlen der Translations- und Rotationsfreiheitsgrade möglich ist.

Contents

1

INTRODUCTION

The trapping and cooling of atoms [1, 2], ions [3] and molecules [4] to ultracold temperatures has opened up new frontiers of research, yielding a quantum mechanical playground for experimental physicists and chemists. With the decrease in energy, the control over the quantum state increases, thus providing a key tool for exploring diverse phenomena in fundamental physics and chemistry. The cooling close to the absolute zero temperature facilitates the preparation of these systems in well-controlled states, resulting in an enhanced understanding of many-body quantum physics [5], linking various research fields as quantum optics and atomic physics with molecular [6], solid-state [7], high-energy physics [8] and quantum information processing [9].
Despite these ground-breaking research into the field of cooling atoms, cations and molecules to ultracold temperatures, anions have yet not been cooled below helium cryostat temperatures. Since the discovery of anions in Titan's atmosphere [10, 11] and even outside the solar system [12], pushing the frontier of anion cooling further is of great interest in laboratory astrochemistry [13, 14]. Collisional studies and precision spectroscopy of cold molecular anions can give information about their creation and destruction paths. Measuring the reactivity of these astrochemically relevant anions in well-controlled conditions, provides insight to improve simulations governing the evolution and composition of these extraterrestrial environments [15, 16]. Sophisticated studies on energy-dependent reactive collision dynamics have been done for various astrochemical anions, i.e. investigating the growth of the anionic carbon chains in a crossed-beam velocity map imaging setup with energy ranging from 0.3 eV to 3 eV [17]. Additionally, studies have been performed to explore the fundamental class of associative detachment reactions of hydrogen in the early universe, measured in a merged anion-neutral apparatus [18] and in a cryogenic multipole radio frequency ion trap, for relative collision energies between 10 and 135 Kelvin [19]. In a similar setup, the proton exchange formation of ammonium, occuring in interstellar media, has also been investigated in a well-controlled temperature range [20, 21].
A dominant destruction process of anions in space is via photodetachment [22, 13, 14]. Thus, light-particle interaction leads to a neutralization of the anion. Photodetachment measurements with photon energies close to the binding energy of the excess electron reveal rich information about a molecular anion's and the resulting neutral's internal degrees of freedom [23, 24]. The key pre-requisite to investigate near-threshold photodetachment of a molecular anion is an internally cold anionic specie to provide a well-controlled internal state population. This control is achieved in a cryogenic multipole radio frequency trap [25, 26] and in a cryogenic storage ring [27, 28], via state-changing collisions with a cold buffer gas and thermalization to black

body radiation, respectively.
Although, a great interest in cold and ultracold anions exists, they have resisted the attempts to reach these regimes. The lack of multiple stable electronic states prevents the possibility of laser-cooling. There are a few promising candidates, with La^- [29, 30] and C_2^- [31, 32], which have an electronic structure suitable for traditional Doppler cooling. However, the direct laser-cooling has not been experimentally accomplished. A key-requirement for laser cooling anions, is an efficient pre-cooling technique in ultrahigh vacuum conditions. The cooling of one anionic specie to cold or ultracold temperatures would be a pivotal breakthrough, since any other anionic particle could be sympathetically cooled via Coulomb interaction. For instance, in the field of anti-hydrogen production [33, 34] and the study of CPT violation [35], the provision of ultracold anions would be a critical milestone, because the repelling electric charge would allow to cool the anti-protons sympathetically, but prevent their annihilation.
In the field of anion cooling, the state-of-the-art cooling technique is via collisions with a cryogenic buffer gas. However, it is limited by the temperature and high densities of the buffer gas to achieve sufficient cooling rates. Common temperatures that can be achieved using a multipole radio frequency ion trap mounted on a cryostat are on the order of 10 K [19].
This limitation can be overcome by using the well-established techniques of laser-cooling of atoms to obtain an ultracold buffer gas, manifested in the development of the hybrid atom-ion traps. The principles of both ion and atom traps are combined to gain control over studying and tuning the interactions between the two species in the system, leading to a tremendous growth of the atom-ion collision community in the last decade [36, 37]. The sympathetic cooling of cations via collisions with ultracold atoms is shown for atomic and molecular cations [38, 39, 40]. In the case of molecular cations, the cooling of both, the vibrational and the rotational degrees of freedom, was achieved [41, 42], offering full control over the quantum state of the molecular cations. In this manner, reaction dynamics have been studied at low relative collision energies, revealing the quantum nature of the two collision partners, with only few partial waves contributing to the collision dynamics [43, 44, 45]. These measurements in addition to providing physical insights into such atom-ion systems, also allow to benchmark theoretical quantum chemistry calculations[46].
The fascinating results observed in cation-atom systems motivated the development of first experiments combining a rubidium magneto-optical trap with OH^- anions in an octupole wire trap [47] and theoretical studies on the cooling dynamics in such multipole ion traps with a high atom-to-ion mass ratio [48, 49], reveal interesting thermalization behavior. In such hybrid systems, it is possible that an ion can gain energy, even in a collision with an atom at rest, yielding non-thermal energy distributions, well-described by a power law distribution [48, 50, 51]. These distributions were experimentally observed for ions trapped in a linear Paul trap overlapped with atoms in a dipole trap [52, 53]. Thus, with the flexibility to overlap ions with photons or/and atoms, hybrid atom-ion traps have proven to be a great platform to

study anion-atom interaction dynamics.
Building on the principles of laser-induced evaporative cooling and sympathetic cooling via collisions with an ultracold buffer gas, this thesis presents two novel anion cooling techniques, which will make the cold anion regime accessible from a gas, that is initially at room temperature.
The first cooling technique is based on forced evaporative cooling via far-threshold photodetachment. Although, these ideas had been proposed more than three decades ago [54], they have never been experimentally demonstrated. The advantage of photodetachment forced evaporative cooling, compared to lowering the trap potential [55, 56], is that the thermalization collision rate is not lowered and therefore the efficiency is not depreciated. Cerchiari et al. showed that they can reduce the translational energy of an O^- cloud by about a factor of 3.5 via photodetachment at a static position [57]. However, by dynamically moving the photodetachment beam one can improve in both, the cooling rate and the final temperature of the anions. This thesis presents a cooling measurement of an ensemble of OH^- ions, initially at 370(12) K, cooled down to temperatures below the one of cryogenic helium in less than 2 seconds. The cooling dynamics are well-described by a developed thermodynamic model governing the photodetachment loss and ion-ion radio frequency heating.
The second anion cooling technique is based on sympathetic cooling via a laser-cooled cloud of rubidium atoms in a dark spontaneous force optical trap. The sympathetic cooling in a hybrid atom-ion trap is a well-established technique for cations [38, 39, 40], but investigations of anion cooling via a heavy buffer gas are rather limited [47]. The hybrid atom-ion trap (HAITrap) presented in this work is developed as part of an international collaboration between the research groups of Prof. Matthias Weidemüller in Heidelberg and Prof. Roland Wester in Innsbruck. This thesis presents the sympathetic cooling of atomic, O^-, and molecular, OH^-, anions. The non-trivial dynamics of anion-atom interactions were experimentally explored and discussed. Despite their similar coolant-to-anion mass ratio, the anions exhibit different cooling dynamics, due to their dissimilar loss mechanisms. The loss channels of these systems were also identified and quantified. Several cooling measurements are shown, in which the relative overlap between both clouds was changed to show the dependency of the cooling dynamics on the relevant collision rates in the system.
This thesis is divided into three main chapters.
In Chapter 2 the experimental setup is introduced. This chapter is separated in three parts, in which the anion trapping, the atom trapping and the co-trapping is explained. The first two parts are structured similarly, first discussing the trapping principle, followed by the implementation in the hybrid atom-ion trap (HAITrap) setup in Heidelberg and subsequently, the atom and ion cloud characterization methods. Finally, in the third part the co-trapping of both species, the evolution of their overlap and the calibration of their relative position is discussed.
Chapter 3 presents the technique of forced evaporative cooling via energy-

selective photodetachment. First the theoretical framework of evaporative cooling and heating via photodetachment is introduced. Followed by experimental data showing that photodetachment at a fixed beam position is altering the anions' energy distribution. Finally, forced evaporative cooling of anions via far-threshold photodetachment is presented for the first time. The cooling dynamics are well-described by the introduced thermodynamic model, including an ion-ion radio frequency heating term, determined independently.
In Chapter 4 the sympathetic cooling of O^- and OH^- is shown. In the first section the collision dynamics of an ion inside a radio frequency trap overlapped by an ultracold atom cloud is discussed theoretically. The driven radio frequency system leads to non-thermal final energy distributions. The expected energy distribution for this system is presented. However, further investigations show that about 100 collisions are required to reach this steady state. Therefore, in the second section anion loss channels, which limit the maximum number of elastic collisions reached, due to reactive collisions and photodetachment, are measured and quantified. Finally sympathetic cooling of O^- and OH^- co-trapped with rubidium is shown. By varying the relative overlap between both clouds, the cooling dynamics were altered to investigate the influence of the ion-ion and atom-ion collision rates. For high ion-ion thermalization rate, the cooling could be well described by a thermodynamic model, including the transfer of the ions' micromotion to the atoms' frame of reference.
In the final chapter 5 the key results from this work are summarized and future prospects for these cooling techniques are outlined.

2

HYBRID ATOM ION TRAP

This chapter summarizes the working principle and the implementation of the key components of the hybrid atom-ion trap (HAITrap) experiment in Heidelberg. The experiment combines an octupole radio frequency (rf) wire trap and a dark spontaneous force optical trap (darkSPOT). In this chapter both traps are explained separately. First the trapping principle is explained, following the implementation in the experimental setup and lastly the diagnostics to derive the ions' or atoms' energy and spatial distribution. Thus, the chapter is divided in section 2.1 explaining the linear rf trap for ion trapping and in section 2.2 discussing the magneto-optical atom trap for trapping ultracold atoms. The third section 2.3 governs the co-trapping of both species, discussing the time-dependent overlap integral and the calibration of the atom and ion spatial diagnostics.
The HAItrap experiment is an international collaboration between two research groups in Heidelberg, Germany and Innsbruck Austria. The planning and execution of the first generation of this HAITrap was carried out in the group of Prof. Dr. Roland Wester, where a trapped ensemble of OH^- anions was overlapped with laser-cooled Rb atoms in a magneto-optical trap [47].
Within this collaboration, the characterization of the ions' energy distribution in the octupole radio frequency trap after thermalization to room temperature helium buffer gas and development of a detection scheme to determine the ions' energy distribution via their time of flight to the detector, was achieved [58].

2.1 TRAPPING OF ANIONS

In this section, the principle of a linear radio frequency trap and its implementation in th HAITrap experiment is discussed. Section 2.1.1 explains the trajectory of a charged particle in a rf trap and the dependency of the particle's motion on the number of rf electrodes. In section 2.1.2, the realization of the ion system following an ion's path through one experimental cycle, is discussed. Starting with the ion creation in a plasma discharge source, mass selection in a Wiley-McLaren mass spectrometer, loading into the octupole wire trap and the detection via a multi channel plate. The following two subsections discuss two ion distribution diagnostic techniques. First the far-threshold photodetachment tomography in section 2.1.3 and second the distribution of ions' time of flight (TOF) from the trap to the detector in section 2.1.4.

2.1.1 MOTION OF AN ION IN A RADIO FREQUENCY TRAP

Charged particles in an electric or magnetic field experience a force, which can then be used to confine these particles. Unfortunately, one can not create a three-dimensional potential minimum by a constant electric or constant magnetic field (Earnshaw's theorem). However, this limitation can be overcome by either combining static magnetic fields with static electric fields, or via time-varying electric fields with static ones, thus, stabilizing the charged particles dynamically. The commonly used ion traps are on one side Penning traps [59, 60], which are based on the first approach, the combination of static magnetic and static electric fields. And on the other side Paul traps [61], which are based on the second approach. Hans Dehmelt and Wolfgang Paul were honored by the Nobel prize in 1989 for the development of these types of traps. The following section will focus on the explanation of a charged particle in an oscillating electric field, because in this experimental setup, the ion trap utilizes the time-varying electric field for trapping.

The classical motion of a charged particle, with a mass m and a charge q, in an electromagnetic field is described by:

$$m\ddot{\mathbf{r}} = q\mathbf{E}(\mathbf{r},t) + q\dot{\mathbf{r}} \times \mathbf{B}(\mathbf{r},t). \tag{1}$$

$\mathbf{E}$ ($\mathbf{B}$) being the electric (magnetic) field vector. For the understanding of the Paul trap, the Lorentz force can be neglected, due to the absence of a magnetic field. Assuming an homogeneous oscillation electric field $\mathbf{E}(\mathbf{r},t) = \mathbf{E}_0 \cos(\omega t)$, with ω as the angular frequency, the solution of the equation of motion is simple. It is described by an oscillatory motion around a constant position in space:

$$\mathbf{r}(t) = \mathbf{r}(0) - \frac{q\mathbf{E}_0}{m\omega^2}\cos(\omega t), \tag{2}$$

as shown in Figure 1 **a**. This motion is called micromotion.
In the case of a homogeneous electric field the solution is quite simple. However, for inhomogeneous fields the equation of motion can be solved analytically only in special cases. The ideal quadrupole trap is one of those rare cases, for which an analytical solution exists, as will be discussed later. In a more general perspective, a multipole field of the n'th order is described in the radial plane with the n'th term of the multipole expansion [62]:

$$\begin{pmatrix} E_x \\ E_y \\ E_z \end{pmatrix} = E_0 n \left(\frac{r}{R_0}\right)^{n-1} \begin{pmatrix} -\cos[(n-1)\phi] \\ \sin[(n-1)\phi] \\ 0 \end{pmatrix}. \tag{3}$$

with r, ϕ being the cylindrical coordinates in the radial plane and R_0 the distance of the electrodes to the trap center. Thus the force ($\mathbf{F}(\mathbf{r}) = q\mathbf{E}(\mathbf{r},t)$) on the charged particle becomes dependent on the radius, leading to a time-averaged force towards the trap center and an additional drift motion. This

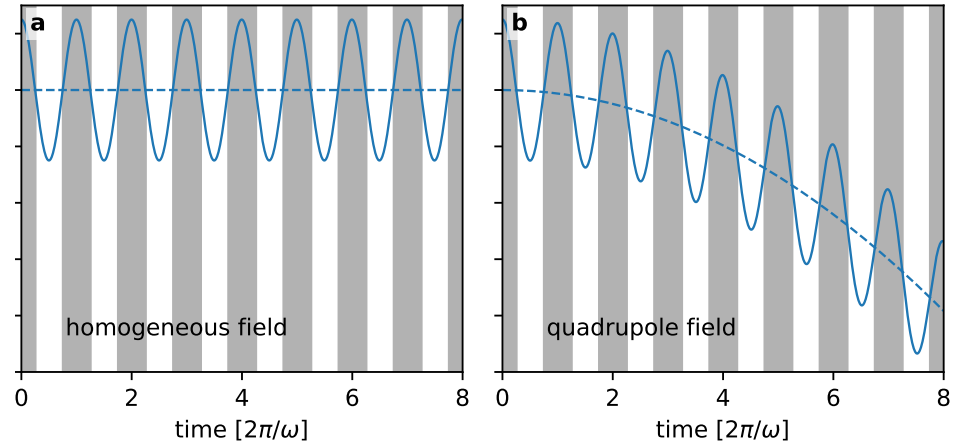

Figure 1: Trajectory of a charged particle in an oscillating field, namely, **a**, in a homogeneous field (see equation 2) and **b**, in a quadrupole field. The dashed blue lines represent the mean position and the background shading illustrates the alternating polarity of the electric field.

slow drift motion is called macromotion. Figure 1 **b** shows the movement of a charged particle in a quadrupole field and the resulting drift motion. The amplitude of the electric field strength in a trap of the order n is given by $E_0 = \frac{U_0}{R_0^n}$, with U_0 being the applied voltage. For the special case of a quadrupole field ($n = 2$), the equation of motion has an analytical solution, because the two radial degrees of freedom are decoupled as followed:

$$m \begin{pmatrix} \ddot{x} \\ \ddot{y} \\ \ddot{z} \end{pmatrix} = \frac{qU_0}{R_0^n} n r^{n-1} \begin{pmatrix} -\cos[(n-1)\phi] \\ \sin[(n-1)\phi] \\ 0 \end{pmatrix} \overset{n=2}{=} \frac{qU_0}{R_0^2} \begin{pmatrix} -x \\ y \\ 0 \end{pmatrix}. \tag{4}$$

For an applied voltage with a constant and an oscillating term ($U_0 = U_{DC} + U_{AC}\cos\omega t$) this results in a well-known set of differential equations by substituting $\omega t = 2\tau$:

$$\begin{aligned} \frac{d^2x}{d\tau^2} + (\lambda + 2\gamma\cos(2\tau))x = 0 \\ \frac{d^2y}{d\tau^2} - (\lambda + 2\gamma\cos(2\tau))y = 0, \end{aligned} \tag{5}$$

with $\lambda = \frac{8qU_{DC}}{mR_0^2\omega^2}$ and $\gamma = \frac{4qU_{AC}}{mR_0^2\omega^2}$. Note, in the ion trapping community, these parameters are also often referred to as a and q, respectively. These equations are known as the Mathieu equations and λ, γ are the stability parameters. The Mathieu theory is well-studied and provides a stability diagram with sets of λ and γ, for which the trajectory is stable in both dimensions. An example for such a trajectory in a quadrupole field is shown in Figure 2. The field is generated by four hyperbolically shaped electrodes. The applied rf voltage of opposing electrodes are in phase. Neighboring ones are shifted by 180°. This electrode configuration is called ideal Paul trap. Often the hyperbolically

shaped electrodes are replaced by cylindrical rods, which makes the trap construction easier and the field deviations are negligible in the trapping region. The ideal rod diameter to approximate the hyperbolic curvature is given by:

$$d = \frac{2R_0}{n-1}. \tag{6}$$

Corresponding to the Paul trap shown in Figure 2, the rods are illustrated as white dashed circles.

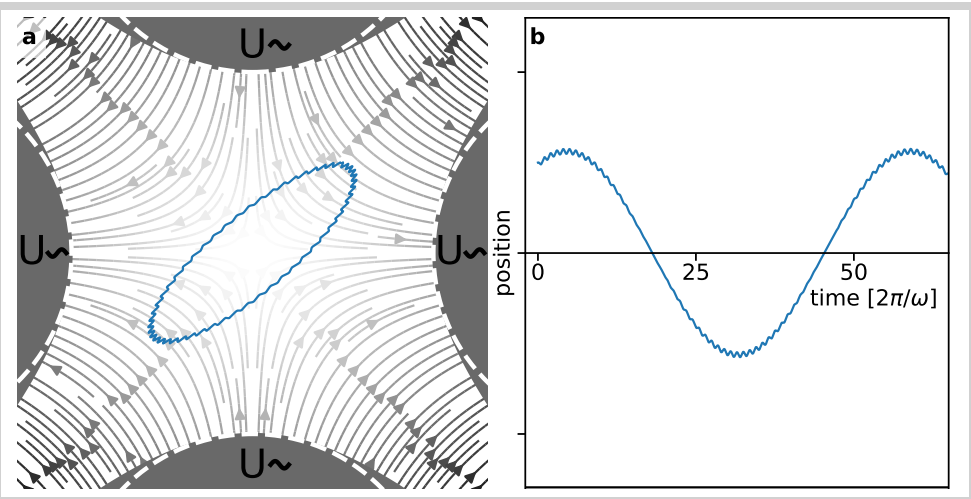

Figure 2: Ion motion in a rf trap. **a**, radial geometry of an ideal Paul trap ($n = 2$). The hyperbolic shaped electrodes are depicted in gray. The white dashed half-circles represent the cylindrical electrodes, which approximate the ideal electrodes best. The arrowed lines represent the electric quadrupole field at one point in time. Their shading illustrates the electric field strength, being the lowest for the lowest opacity. The blue line is a stable trajectory of a charged particle in the trap. **b**, the ion's position as a function of time.

For traps with higher order ($n > 2$) the dimensions can not be decoupled and an ion's trajectory can only determined via numerical integration. A more computation friendly approach is to separate between the two timescales of micro- and macromotion, called adiabatic approximation. This separation is only valid if the rf frequency is much larger than the trapping frequency of the drift motion:

$$\mathbf{r}(t) = \mathbf{r}_\mathrm{d}(t) + \mathbf{r}_\mathrm{rf}(t), \tag{7}$$

where $\mathbf{r}_\mathrm{rf}(t)$ is the fast motion following the rf field and $\mathbf{r}_\mathrm{d}(t)$ the drift motion, due to the inhomogeneity of the rf field. Assuming that the amplitude of the macromotion is much larger than the micromotion ($\mathbf{r}_\mathrm{d}(t) \gg \mathbf{r}_\mathrm{rf}(t)$), it is possible to describe the force $\mathbf{F}(\mathbf{r}) = m\ddot{\mathbf{r}}$ as a Taylor series expansion around $\mathbf{r}_\mathrm{d}(t)$ truncated after the linear term:

$$m\ddot{\mathbf{r}}_\mathrm{d}(t) + m\ddot{\mathbf{r}}_\mathrm{rf}(t) = \mathbf{F}(\mathbf{r}_\mathrm{d}) + (\mathbf{r}_\mathrm{rf}\boldsymbol{\nabla})\,\mathbf{F}(\mathbf{r}_\mathrm{d}) + \ldots \tag{8}$$

The applied assumption was introduced as the adiabaticity parameter by Teloy and Gerlich [63, 62], which is in the limit of a quadrupole trap ($n = 2$), the AC stability parameter $\gamma_n = \frac{2nqU_{AC}}{mR_0^2\omega^2}$, derived in the Mathieu formalism:

$$\eta = \frac{2|\left(\mathbf{r}_{rf}\boldsymbol{\nabla}\right)\mathbf{F}(\mathbf{r}_d)|}{|\mathbf{F}(\mathbf{r}_d)|} = \gamma_n(n-1)\left(\frac{r}{R_0}\right)^{n-2} \overset{n=2}{=} \gamma. \tag{9}$$

As long as $\eta \ll 1$, it is possible to truncate the Taylor series after the linear term. For short times, comparable to the rf period, the first and the fourth term in equation 8 are negligible, resulting in two separate equations for the micro and the macromotion. The micromotion is then given by the second and the third term in equation 8:

$$m\ddot{\mathbf{r}}_{rf}(t) = \mathbf{F}(\mathbf{r}_d) \tag{10}$$

$$\Rightarrow \mathbf{r}_{rf}(r,\phi,t) = \frac{\gamma_n R_0}{2}\left(\frac{r}{R_0}\right)^{n-1}\cos(\omega t)\begin{pmatrix} -\cos[(n-1)\phi] \\ \sin[(n-1)\phi] \\ 0 \end{pmatrix}. \tag{11}$$

Plugging this into equation 8 and averaging over one rf period results in the following equation of macromotion:

$$\ddot{\mathbf{r}}_d(t) = \frac{\gamma_n^2\omega^2}{8R_0}(n-1)\left(\frac{r}{R_0}\right)^{2n-3}\begin{pmatrix} \cos[(n-1)\phi] \\ \sin[(n-1)\phi] \\ 0 \end{pmatrix}. \tag{12}$$

Thus, in the adiabatic approximation the macromotion can be described as the motion in a quasi-static potential $\mathbf{F}(\mathbf{r}_d) = \boldsymbol{\nabla}V_{eff}$, also called the effective potential:

$$V_{eff}(r) = \frac{m\gamma_n^2 n^2\omega^2 R_0^2}{16}\left(\frac{r}{R_0}\right)^{2n-2} = \frac{n^2q^2U_{AC}^2}{4mR_0^2\omega^2}\left(\frac{r}{R_0}\right)^{2n-2} \tag{13}$$

Equation 11 and 13 yield that the effective potential is, in fact, the time-averaged mean kinetic energy of the micromotion:

$$V_{eff}(r) = \left\langle \frac{1}{2}m\dot{\mathbf{r}}_{rf}^2 \right\rangle. \tag{14}$$

For a quadrupole trap, the effective potential has a quadratic dependency on the radius. With increasing pole order the micromotion is becoming more and more suppressed and in the limit of $n \to \infty$ the potential is box shaped. Figure 3 **a** shows the ions' motion in time, calculated via numerical integration of equation 4 for three different pole orders. In Figure 3 **b** one can see the effective potential corresponding to the pole orders. In blue the Paul trap is shown and in orange the octupole trap, which is the trap configuration used in the HAITrap experimental setup. The 22-pole trap is shown in green. This trap is a commonly used trap because not only the micromotion is greatly suppressed, it is also easier to construct, because for an inner trap diameter of

1 cm the ideal rod diameter is 1 mm [64]. Although, the micromotion in higher pole order traps is suppressed more, an octupole configuration is chosen in the HAITrap setup, because the optical access to the ion trap center is needed for the implementation of the atom trap.

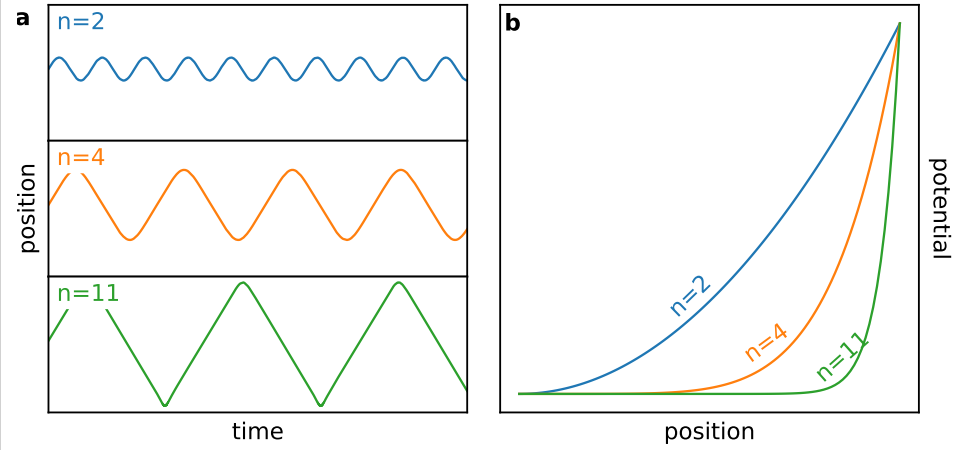

Figure 3: Ion motion inside rf traps of different order n. **a**, radial position of a charged particle as a function of time for different multipole orders. The blue trajectory corresponds to a Paul trap ($n = 2$) and the trajectory shown in Figure 2. The orange and green curve are numerical solutions of equation 11 for an octupole trap ($n = 4$), as used in this HAITrap setup, and a commonly used 22-pole trap ($n = 11$). **b**, the corresponding effective potential for different pole orders, see equation 13.

2.1.2 SETUP FOR CREATION, GUIDING AND TRAPPING OF ANIONS

In this section, the implementation of the ion setup is discussed, starting with the creation of O^- and OH^- anions and selecting the specie of choice. The technical drawing of the experiment in Figure 4 represents all important parts of the experiment, involving the ions, from a laboratory perspective. It also comprises the ultra high vacuum system, which is imperative to decouple the experiment from the environment. The system consists of two chambers, which are separated by a differential pumping stage between the two turbo pumps The left cross is call source chamber. Attached to this chamber is a 80 L/s turbo pump, the ion source flange and the Wiley-McLaren accelerator flange. After the differential pumping stage there is a second cross, with a 685 L/s turbo pump, followed by the trap chamber. With this pump setup, a vacuum of 10^{-9} mbar in the trap chamber was created, although, a lot of gas is introduced into the system in course of the ion creation. In this section, the ions path is followed from creation and selection to trapping and detection.

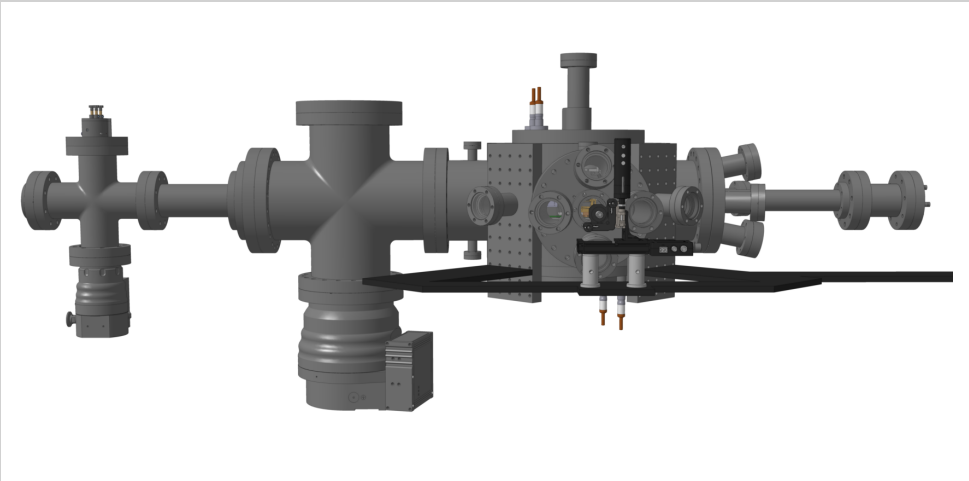

Figure 4: Laboratory perspective onto the HAITrap experimental setup. In the following subsections, the parts relevant for ion trapping are discussed and highlighted in red. The complete setup, including the atom trapping apparatus, will be described later.

2.1.2.1 *Creation of molecular anions*

The ion source used in the HAITrap experiment is based on plasma discharge of injected gas pulses. This technique has been established by Osborn et al. [65]. The design used in this setup follows the one presented in [66] and was further developed in earlier work in the group [67], why it is called the *Lopez valve*. A more detailed description and characterization can be found in [68].
A great advantage of this source is the compact design. As shown in Figure 5, the entire source is mounted on one CF100 flange. The flange includes a gas reservoir filled by a carrier gas, which is mixed with a small amount of another gas to create the ion of choice. For the creation of O^- and OH^-, argon gas mixed with water vapor is used. The pressure in this container is typically 1 bar and the water vapor is included by a small water reservoir in the pressure tubing before the ion source flange. A constant argon pressure and laboratory temperature leads to a stable vapor pressure in the carrier gas.
The zoom-in in Figure 5 shows schematically a cut through the central plane of the flange. There is a hole from the gas reservoir to the ultra high vacuum region. This hole has a diameter of 200 µm and is sealed by a small VMQ silicon rubber patch. This rubber patch is attached to a piezo element (PTZ503), which can be bent by applying a voltage on one side of the element. The injection hole is closed applying 180 V and opens up by around 200 µm for the opposite polarity, −190 V. This displacement allows a sufficient gas flow into the vacuum chamber. One of the before mentioned development of the design are three fed-through micrometer screws, which allow an adjustment of the piezo position and angle during operation. This way, the alignment of the rubber patch on the injection hole can be optimized, without needing to break the vacuum of the source chamber.

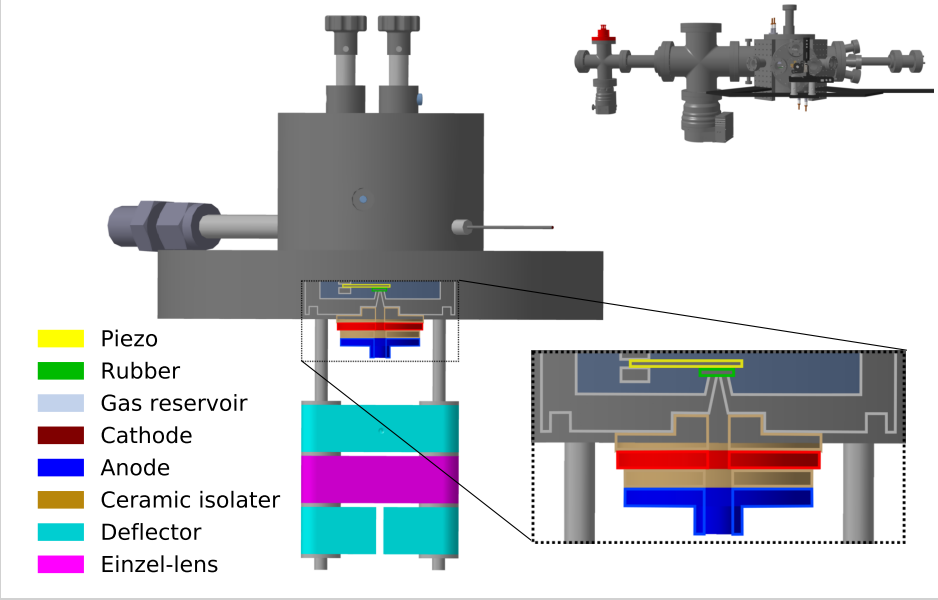

Figure 5: Ion source flange, marked in red in the overview inset. Shown is the CF100 flange, which includes the gas reservoir and a conical hole towards the ultra high vacuum chamber. The hole is sealed by a rubber patch, which is attached to a piezo crystal. The piezo can be lifted by a voltage applied to it. The injected gas is ignited by a cylindrical plasma electrode stack and the produced ions are guided by ions optics towards the mass selection region.

The gas injection is followed by the plasma ignition in a cylindrical electrode stack. After about 140 µs a voltage of −830 V between cathode and anode is switched on rapidly. The strong electric field is switched on for 80 µs, accelerating free charges and leading to the ignition of a glow plasma. O^- and OH^- are then created capturing low energy secondary electrons [69]. The injection hole is funnel shaped (increasing diameter along the gas flow) is proven to minimize the free expansion perpendicular to the flow, leading to a high number of ion-neutral collisions after the strong electric field is switched off. These collisions cool the internal degrees efficiently [65]. 2 cm behind the ignition region there is an ion optics stack, which allows to guide and focus the ions into the mass-selection region. A detailed description of this compact ion optics design can be found in [70].

2.1.2.2 *Mass-selection of various anions*

In the above mentioned glow discharge of Argon carrier gas and water vapor a variety of different ions are created, even multiple orders of hydrated O^- and OH^- clusters [71, 72]. The selection of the ion specie is based on the time of flight after the acceleration in a linear electric field. The mass resolution is improved using a design from Wiley and McLaren [73]. This design consists of three parallel plate electrodes. In Figure 6 these electrodes are shown as green plates, mounted on a flange stack perpendicular to the ion source flange. The

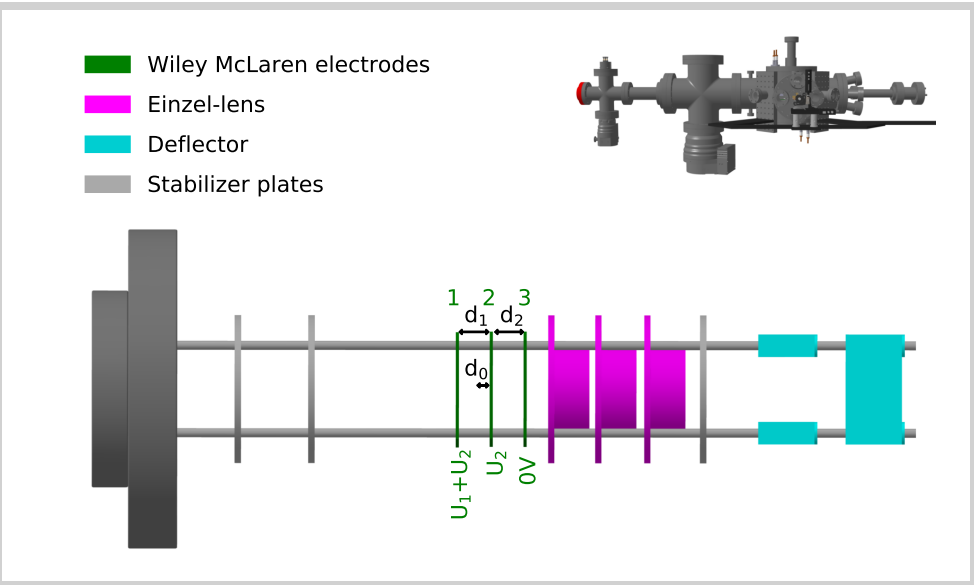

Figure 6: Mass selection flange. The mass spectrometer design by Wiley and McLaren is realized by the three plates (green) with relative distances d_1 and d_2. From the source flange, the ions enter between electrode 1 and 2, with the distance d_0 to the second plate. When they reach the setup center the electrodes 1 and 2 are switched from ground to the voltages $U_1 + U_2$ and U_2. The ions are accelerated to the right, with a TOF depending on their charge to mass ratio. After passing the electrode 3 the trajectories can be further manipulated with an Einzel lens and deflectors to guide ions through the following differential pumping stage.

ions are guided and focused between plate **1** and **2**. In the moment they arrive the voltages $U_1 + U_2$ and U_2 are applied to those plates. There is a cut out in the center of the second and third electrode, which is covered by a fine metal mesh. Thus the three electrodes generate two linear electric field regions, in which the ions are accelerated towards the rf trap. Initially the ions are place at a distance of d_0 from the second plate and their velocity towards the trap is negligible. The ions are accelerated and reach the second field region with a velocity of

$$v_1 = \sqrt{\frac{2q}{m}\frac{d_0}{d_1}U_1}, \tag{15}$$

with $\frac{q}{m}$ being the ions charge to mass ratio. At the end of the second acceleration region the ions' velocity is

$$v_2 = \sqrt{\frac{2q}{m}(\frac{d_0}{d_1}U_1 + U_2)}. \tag{16}$$

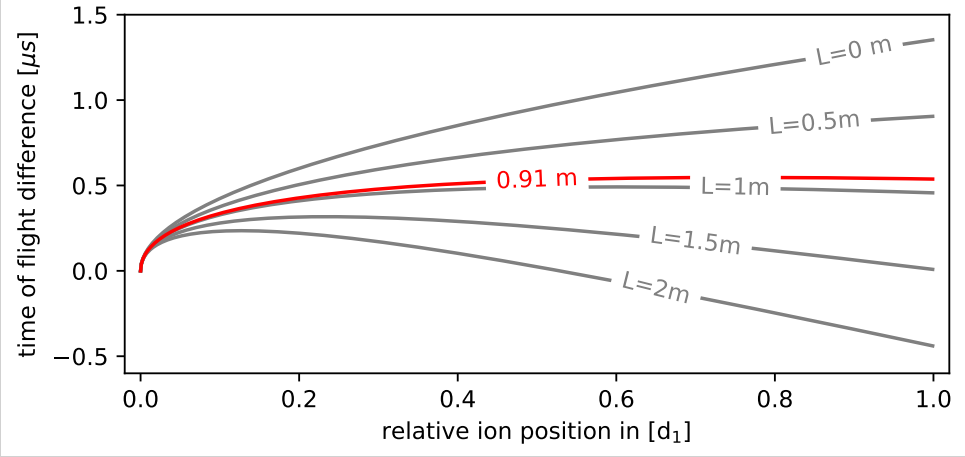

Figure 7: Time of flight of OH^- to a distance L from the third electrode as a function of the starting position d_0. The red line corresponds to a distance of $L = 0.91$ m, which is the distance between the third Wiley-McLaren electrode and the rf trap center.

After passing the third electrode the ions fly with the velocity v_2 towards the trap, which is placed in a distance L. The total time of flight (TOF) from the position d_0 into the trap can be calculated as following:

$$t_{\text{tot}} = \frac{m}{q}\frac{d_1}{U_1}v_1 + \frac{m}{q}\frac{d_2}{U_2}(v_2 - v_1) + \frac{L}{v_2} \propto \sqrt{\frac{m}{q}}. \tag{17}$$

Thus, ions with different charge to mass ratio get separated in time. In the HAITrap setup the plate distances are $d_1 = d_2 = 11$ mm. To improve the trap loading the electrode voltages are adjust to $U_1 = 24$ V and $U_2 = 239$ V for a distance to the trap $L = 0.91$ m. Figure 7 shows the deviation of the arrival time as a function of the position between the electrode **1** and **2** for different trap positions, relative to the Wiley-McLaren electrodes. The set configuration and trap distance $L = 0.91$ m is highlighted in red. One can see that ions spread over a large range between the two electrodes are focused in time into the trap.

The final ion selection is done by switching a deflector in front of the trap. Thus only when the ion of choice is passing the deflector, it is switched to guide them into the trap. A second stage of selection is to opening time of the trap, which follows the same principle.

The Wiley McLaren electrodes follow an Einzel lens, a horizontal and a vertical deflector. These are needed to guide the ions through a pinhole into the trapping chamber. The pinhole between source and trapping chamber creates a pressure difference of one order of magnitude. Although, the injection of the carrier gas increases the pressure in the system, a vacuum below 10^{-9} mbar can be reached in the trap chamber.

2.1.2.3 *Radio frequency octupole wire trap*

The radio frequency trap in our HAITrap experiment is a thin wire octupole trap ($n = 4$), originally designed and build in the group of Prof. Roland Wester in Innsbruck. The octupole trap has the advantage of a reduced micromotion in the trap center as discussed in section 2.1.1. The reduction of the micromotion results in lesser heating processes, which are discussed in detail in section 3.3.2 for the evaporative cooling and in section 4.1 for the sympathetic cooling, especially with a heavy buffer gas.
An even higher pole order would favor the cooling. Unfortunately, additional electrodes would also block the optical access needed for the realization of the magneto-optical atom trap. Thus, the pole order is a trade-off between optical access and rf heating. More optical access can be achieved by replacing the hyperbolically shaped rf electrodes with thin wires. As discussed in section 2.1.1 an ideal multipole field is generated by hyperbolically shaped electrodes. By replacing the electrodes with wires, the ideal multipole field is disturbed close to the electrodes. However, for large distances to the electrodes, the deviation from the ideal field is negligible. To ensure that the ions are in this trap region, they are cooled down by a 300 K helium buffer gas pulse. In a molecular dynamic simulation, it was shown that indeed for the thermalized ions the deviations are negligible [58].
Figure 8 illustrates the implementation of the rf-wire trap in the trap chamber. The ion optics in front and after the trap, as well as the trap itself are mounted on a CF160 cluster flange, including electric and buffer gas feed-throughs and the ion detector. The threaded rods, which serve as mount for all components, are stabilized by eight circular metal plates. This way the entire trapping and detection system is mounted on one flange, which makes it easily accessible.
The purpose of the ion optics in front of the trap is to guide the incoming ion beam from the left through the hollow-core endcap (yellow) into the trap. The trap itself consists of eight gold-coated molybdenum electrodes, placed on a circle with a diameter of 6 mm. The wires' diameter is 100 µm. To ensure stable trapping, the rf voltage for O^- and OH^- a peak-to-peak voltage of $U_{AC} = 340$ V is chosen at an angular frequency of $\omega = 2\pi \cdot 6.8$ MHz. The axial confining potential is generated via endcap electrodes (yellow), which can be switched during loading from the left and extraction to the right. The total trap length between the two endcaps is 32.5 mm. Due to the kinetic energy the ions gained in Wiley-McLaren mass spectrometer (≈ 250 eV), the entire trap is set to an offset of $U_{\text{off}} = 250$ V. Thus, while entering the trap, the kinetic energy is transferred into potential energy and the ions slow down. During loading, the voltage of the front endcap is lowered to 80 V. After the ions pass the endcap, the voltage is switched to $U_{\text{ec}} = 260$ V and the trap is closed. In addition to the confining electrodes, there are two sets of shielding electrodes. The vertical ones (red) are designed to shield the trap from the coils used for the magneto-optical trap. These grounded coils would pull down the potential in the trap center. The voltage applied to those electrodes correspond to the trap offset ($U_{\text{vs}} = 250$ V). The horizontal set of shielding plates function as shaping electrodes. They are used to create an approximately harmonic

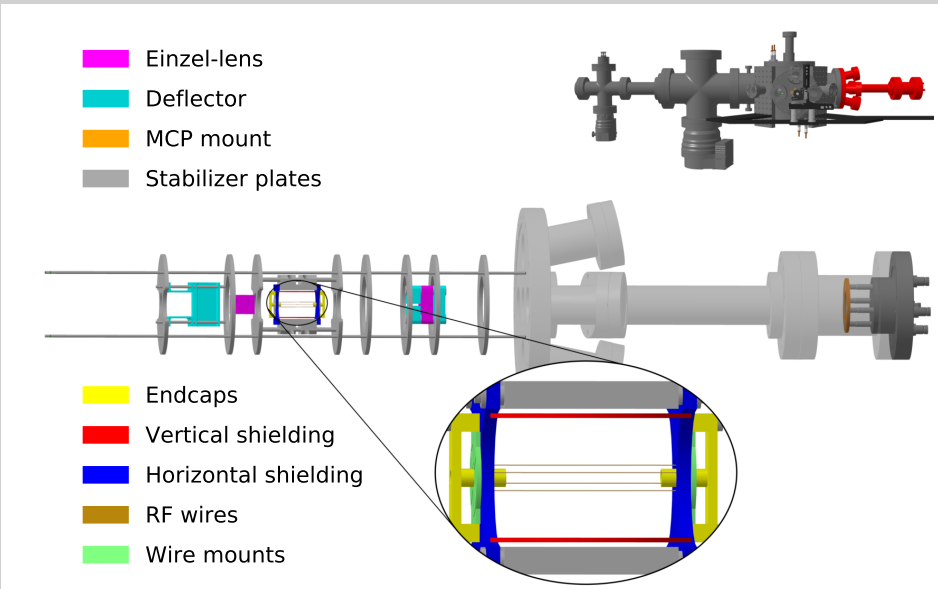

Figure 8: Radio frequency trap flange. The entire radio frequency trap, including guiding ion optics, the multi channel plate detector, electric and buffer gas feed-throughs are mounted on one CF160 flange. The stack is mounted via four threaded rod attached to flange and stabilized by eight grounded circular metal plates. The zoom in shows the rf wire trap, the hollow-core endcap electrodes (yellow) for loading and unloading the ions from the trap. Blue and red are horizontal and vertical static shielding electrodes, respectively.

trapping potential in axial direction ($U_{\mathrm{hs}} = 300$ V) and shape the extraction potential, needed for the time of flight thermometry, which will be discussed in section 2.1.4.
A schematic illustration of the potential along the axial axis is shown in Figure 14, where the extraction potential landscape is discussed.

2.1.2.4 *Thermalization to room temperature Helium buffer gas*

After the loading of the ions into the trap, they are thermalized by a helium buffer gas pulse. A second piezo valve is mounted below the wire trap to flood the trap with the buffer gas at room temperature. The resulting ion temperature, however, is higher than the one of the buffer gas. The main heating mechanism can be attributed to rf heating collisions with the helium atoms. As explained in section 2.1.1 the radial confinement is created by a fast oscillating rf field. Energy of the fast oscillatory motion of an ion can be transferred to the macromotion, by a collision with an atom. To determine the initial energy distribution, a Monte-Carlo buffer gas simulation was performed for the HAITrap design and the potential landscape is simulated by the COMSOL software [58]. This way, the trajectory of a single ion in the trap is calculated solving Newton's equations of motion. The collision of an ion with a buffer gas atom is modeled as a random event. In case of a collision,

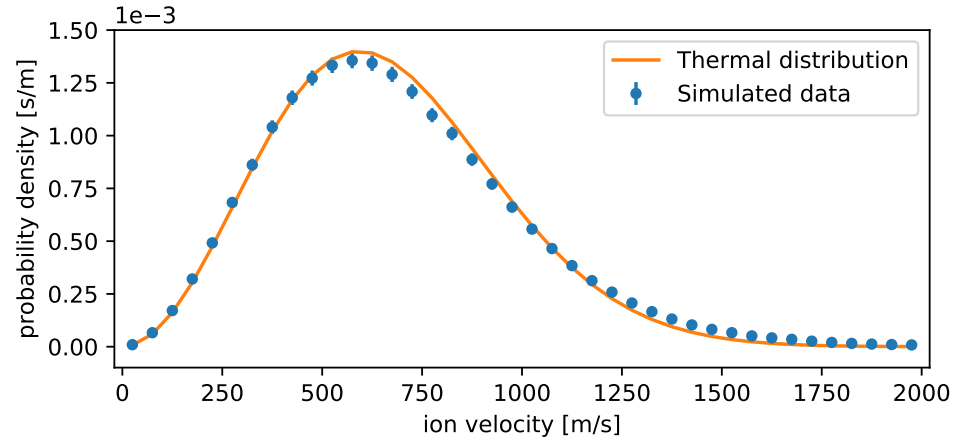

Figure 9: Simulated velocity distribution for OH^- ions thermalized to a 293 K buffer gas in the potential landscape of the HAITrap setup, shown in Figure 8. The orange curve is a fitted Maxwell-Boltzmann velocity distribution with $T = 359(3)$ K.

the atoms' kinetic energy is extracted from a Maxwell-Boltzmann distribution and the resulting change of the ions' velocity and momentum is modeled by a hard-sphere collision. The ions' position and velocity is recorded after a time-average of 25 collisions. Figure 9 shows the ions' velocity distribution after the thermalization to a helium buffer gas with a temperature of 293 K in the HAITrap setup. The orange solid curve corresponds to a fitted Maxwell distribution of $T = 359(3)$ K. One can see that the rf heating results in a non-thermal distribution with a higher probability of fast ions than in a thermal ensemble. For the non-thermal distribution the temperature is typically defined by the ions' mean velocity $\bar{v}$ [74]:

$$T = \frac{\pi m \bar{v}^2}{8 k_B}. \tag{18}$$

With this definition the inital temperature of the ion ensemble in the HAITrap experiment can be estimated to be $T = 366$ K. In the course of these simulations the effect of ion-ion collisions are neglected, which can lead to a rethermalization of the ion ensemble.

2.1.2.5 *Detection of anions*

Opening the right endcap, the ions are extracted and guided via the second optics stack onto a multi channel plate (MCP), where they are counted individually. The MCP (Hamamatsu) is designed to provide a fast rise time, thus it can resolve the single ion impacts and the time of flight from the trap to the detector is saved for each ion. An ion hitting a MCP channel starts an electron avalanche resulting in a voltage peak on the detectors anode. This signal is amplified by a factor of 20 (Ortec) and digitized via a fast USB oscilloscope (PicoScope). The ion counting is done digitally by applying a threshold algorithm, shown in Figure 10 for a typical TOF trace. The threshold is generated

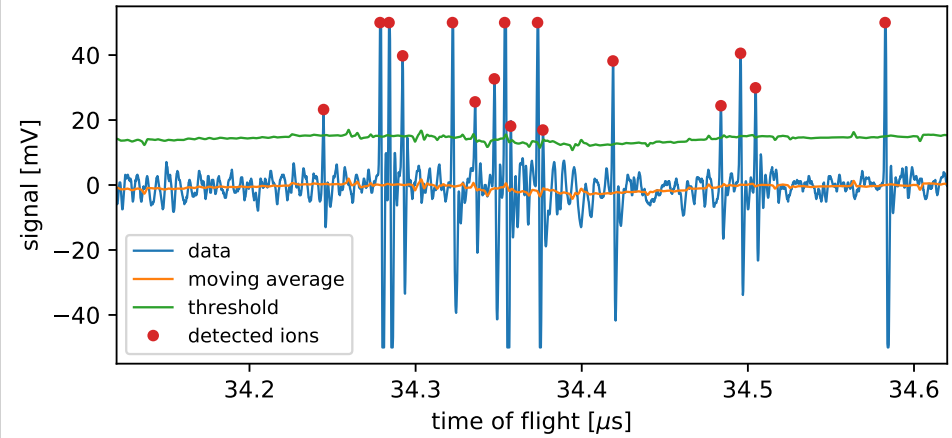

Figure 10: Ion detection algorithm. The raw amplified signal is digitized by a USB oscilloscope. For the threshold, a moving average (orange) is calculated and shifted by an offset (green). An ion impact is counted (red), if the signal exceeds the threshold.

by calculating the moving average of the trace and adding an offset above the noise level. The moving average accounts for slow drifts in the signal.

2.1.3 DIAGNOSTICS VIA PHOTODETACHMENT TOMOGRAPHY

The absorption of a photon by a negatively charged particle can lead to a neutralization of the latter:

$$A^- + h\nu \rightarrow A + e^- \tag{19}$$

This process is called photodetachment. First measurements were already performed in the 1950s, to determine the photodetachment cross section for O^- and OH^- by using a hot tungsten filament light source and band-pass filters [75, 76]. The near-threshold photodetachment is a powerful tool to investigate the level structure of an anion [77]. For molecular anions, the structure becomes even more complex, due to their vibrational and rotational degrees of freedom. Therefore the photodetachment spectrum consists of multiple thresholds corresponding to the possible transitions from an anion to a neutral. By scanning the frequency of the photodetachment light, one can not only map out the level structure, but it is also possible to determine the energy level population, thus perform a thermometry of the internal degrees of freedom of a molecule [25, 27, 28].

In the course of this work, the photodetachment frequency is placed way above the threshold. Hence, the photodetachment cross section is not dependent on the population of the internal degrees of freedom and the ions' velocity. The resulting photodetachment loss rate is then dependent only on the overlap then the photo and the ion distribution [78].

2.1.3.1 *Photodetachment tomography*

The depletion of anions by far-threshold photodetachment light can be described by a first order differential equation of the ion number N:

$$\dot{N} = -\sigma_{\mathrm{pd}} \int_{dV} \Phi(x,z) n(x,y,z) dx dy dz - \nu_{\mathrm{bgr}} N. \tag{20}$$

σ_{pd} being the absolute photodetachment cross-section, $\Phi(x,z)$ the photon flux, assuming it is constant along the propagation direction, y, and $n(x,y,z)$ the ion density. ν_{bgr} is the background loss rate of the trap, which is experimentally determined to be $\nu_{\mathrm{bgr}} = 0.009(1)$ Hz.
Assuming a narrow photon distribution compared to the ions, one can simplify the photon flux by delta functions:

$$\Phi(x,z) = \frac{P}{h\nu} \delta(x - x_{\mathrm{L}}) \delta(z_{\mathrm{L}}), \tag{21}$$

with P being the power of the light, $h\nu$ the photon energy and (x_L, z_L) as the beam position. Plugging the simplified photon flux into equation 20 results in:

$$\dot{N} = -\sigma_{\mathrm{pd}} N \frac{P}{h\nu} \underbrace{\int \rho(x_{\mathrm{L}}, y, z_{\mathrm{L}}) dy}_{\rho_{\mathrm{col}}(x_{\mathrm{L}}, z_{\mathrm{L}})} - \nu_{\mathrm{bgr}} N. \tag{22}$$

The ion density n is the product of the ion number and the normalized ion density distribution $\rho(x,y,z)$. The integration of the density distribution along the beam propagation direction y is called the column density $\rho_{\mathrm{col}}(x,y)$. The solution of equation 22 is an exponential decay:

$$N(t) = N_0 \exp\left[-k_{\mathrm{pd}}(x_{\mathrm{L}}, z_{\mathrm{L}}) t\right], \tag{23}$$

with:

$$k_{\mathrm{pd}}(x_{\mathrm{L}}, z_{\mathrm{L}}) = \sigma_{\mathrm{pd}} \frac{P}{h\nu} \rho_{\mathrm{col}}(x_{\mathrm{L}}, z_{\mathrm{L}}) + \nu_{\mathrm{bgr}}. \tag{24}$$

For a high laser beam power the background loss rate is negligible and the rate becomes directly proportional to the normalized column density. Figure 11 **a** shows a photodetachment loss measurement for four different detachment beam positions along the axial axis, including the fitted exponential decays (see equation 23). Figure 11 **b** illustrates the technical drawing of the photodetachment setup, including an optical fiber coupler mounted on a horizontal and a vertical stage. The photodetachment light is transferred via an optical fiber to the setup. The light propagates perpendicular to the rf-trap axis through the chamber and is focused down to a diameter of 180 µm ($1/e^{-2}$) in the trap center. The detachment light is created by a laser-diode with a photon energy of ≈ 1.88 eV, which is far above the photodetachment threshold for O^- (1.46 eV) and OH^- (1.83 eV) [79].
As the background loss rate is much smaller, the induced photodetachment loss, it can be ignored and the spatial distribution can be directly derived from a position-dependent photodetachment loss measurement. In axial direction

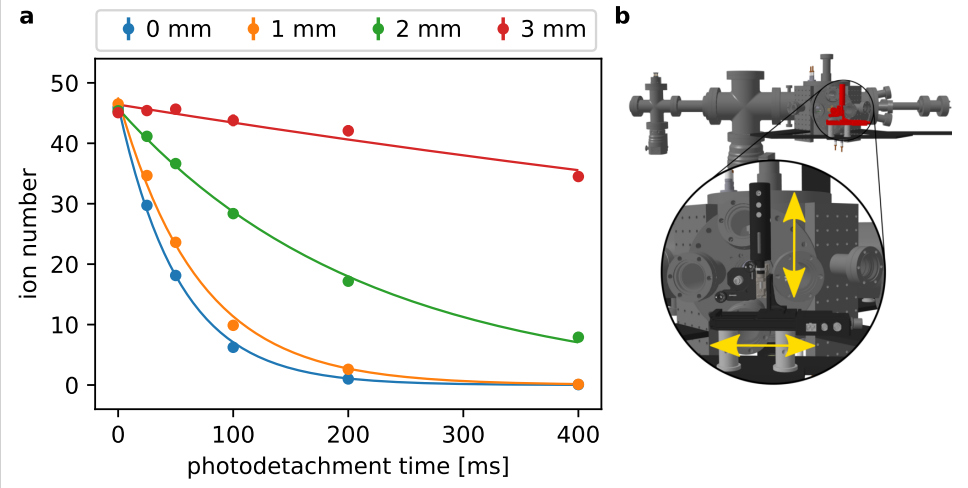

Figure 11: Ion diagnostics via photodetachment tomography. **a**, ion loss as a function of interaction time with the photodetachment light. The different colors correspond to different axial positions, whereas 0 mm is the trap center. Radially the laser beam position is for all measurements the same. The solid lines correspond to fitted exponential decays (see equation 23) to derive the photodetachment loss rate. **b**, illustrates the photodetachment setup, including an optical fiber coupler mounted on a vertical and a horizontal mechanical stage.

the potential, created by the endcaps and the horizontal shielding electrodes, is approximately harmonic, which results in a Gaussian shaped column density distribution:

$$\rho_{\mathrm{col}}(0,z) \propto \exp\left[-\frac{(z-z_0)^2}{2\sigma_z^2}\right]. \tag{25}$$

The effective potential of an octupole trap follows a r^6-dependency, which results in the following column density distribution along the vertical photodetachment axis:

$$\rho_{\mathrm{col}}(x,0) \propto \int_{-\infty}^{\infty} \exp\left[-\frac{((x-x_0)^2+y^2)^3}{8\sigma_{\mathrm{r}}^6}\right] dy. \tag{26}$$

Figure 12 shows two photodetachment tomography measurements for OH^- after the initialization with the helium buffer gas pulse. The axial tomography is measured by moving the laser beam horizontally and the derived data is fitted with function 25. The radial tomography is measured moving the beam vertically. The data is well-represented with function 26. The widths for OH^- are determined to be $\sigma_{\mathrm{z,OH}} = 1.16(2)$ mm in the axial and $\sigma_{\mathrm{r,OH}} = 0.735(3)$ mm in the radial direction. For O^- the axial and radial widths were respectively measured as $\sigma_{\mathrm{z,O}} = 1.14(1)$ mm and $\sigma_{\mathrm{r,O}} = 0.700(7)$ mm.

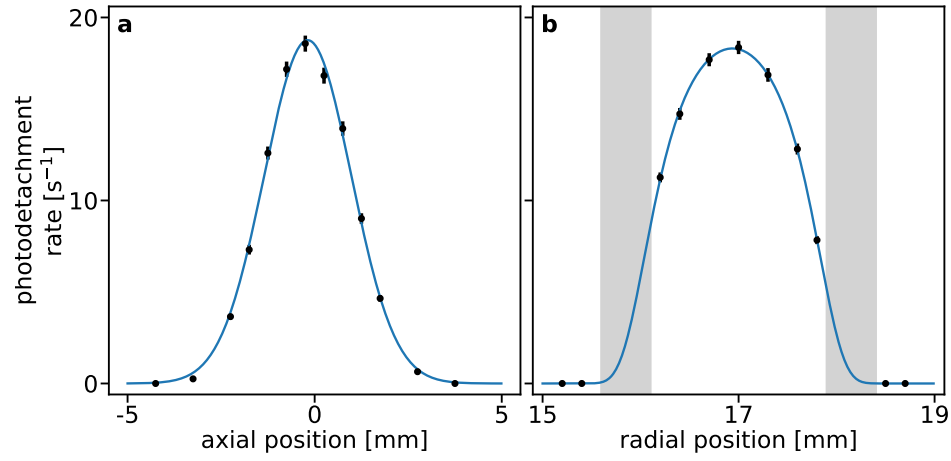

Figure 12: Photodetachment tomography along **a** the axial direction and **b** the radial direction. The black solid points are measured experimental data. The axial tomography is fitted by a Gaussian function as expected from equation 25 (blue curve). The axial width is $\sigma_{z,OH} = 1.16(2)$ mm. The radial tomography is fitted by a 2D distribution in a r^6-potential integrated along one dimension, see equation 26 (blue curve). The width is determined to be $\sigma_r = 0.735(3)$ mm. The gray areas shown in panel **b** illustrate the region, where the photodetachment light is blocked by the wires.

The zero in the axial tomography corresponds to the trap center. One can see that the ion cloud is therefore slightly displaced from the trap center. This can be explained by the surface charges on the wire mounts, which is discussed in the following section.

2.1.3.2 *Influence of surface charges on the wire mounts*

In the course of this work, a shift in the axial direction of more than 2 mm from the trap center was observed. This does not correspond to the symmetry of the trap's electrodes. Figure 13 **a** shows the zoomed in trap design under an angle and illustrates a construction flaw, as the plastic card boards (PCBs) to mount the wires are not properly shielded. These plastic pieces can accumulate charges, which alter the potential landscape. As discussed in [58], the COMSOL software allows to include dielectrics and add surface charges to both PCBs. Figure 13 **b** shows two photodetachment tomographies, in which only the relative voltage on the endcaps are changed. Thus for a higher voltage the ions are pushed more to the trap center and the cloud's width is smaller. The charges on both PCBs are adjusted such that the axial ion distribution fits the tomography with an relative endcap voltage of 50 V at a temperature of 373 K. The temperature is determined as explained above via a molecular dynamics simulation calculating the thermalization to room temperature helium buffer gas (see section 2.1.2.4). Once the charges are calibrated, the potential landscape for a relative endcap voltage of 10 V including those charges is determined.

The change in the simulated ion distribution for 373 K fits very well with the measured tomography for the lower endcap voltage.

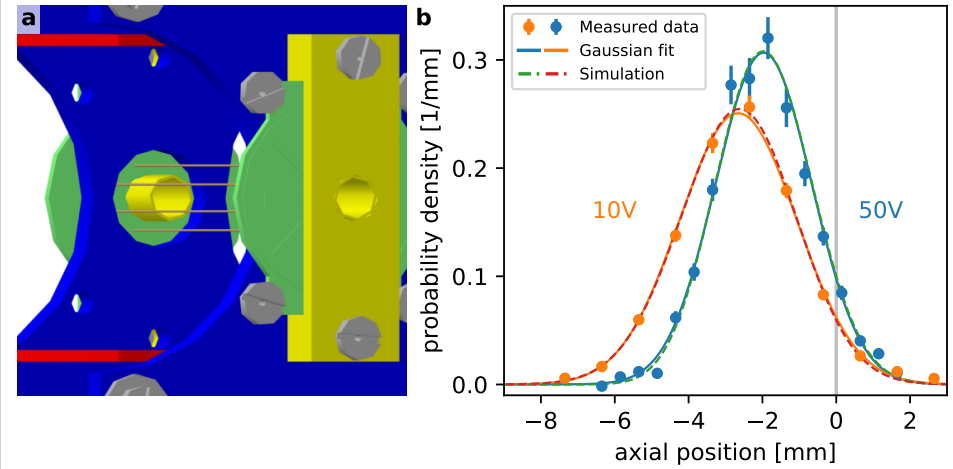

Figure 13: Charges on the wire mounts. **a**, the plastic card board wire mounts (green) are not completely shielded. These dielectrics can accumulate surface charges, which have an influence onto the potential landscape in the ion trap. For highly asymmetric charge ups, this results in a displacement of the ions from the axial trap center. **b**, photodetachment tomography for two endcap voltages, relative to the trap offset. The surface charges lead to different shifts of the ions' spatial distribution. These charges can be added to the COMSOL simulation by taking the blue tomography measurement (endcap at 50V above the trap offset) matching a thermal distribution with $T = 373$ K as a calibration. Once the charges are determined, they are fixed and the potential landscape with the lower endcap voltage can be calculated. The spatial distribution in this potential (red dashed line) matches very well with the measured tomography.

To reduce the charges on the plastic pieces, the entire vacuum system was flooded with air and a hot filament ion gauge was removed, because it was suspected to be the main source for free charges in the chamber. However, a final shift of $\Delta z = -0.17(2)$ mm remains, the charges were reduced successfully and stayed constant. The resulting initial ion distribution for OH^- is shown in Figure 12. These settings are the basis for all following measurements and were not changed anymore. The residual charges on the PCBs are calculated according to the calibration before and are included into the following extraction simulations.

2.1.4 DIAGNOSTICS VIA TIME OF FLIGHT

A disadvantage of the thermometry via photodetachment tomography is the time needed to measure it. A faster approach is the mapping of the ions' energy onto their time of flight from the trap to the detector. Figure 14 shows the potential manipulation during one experimental cycle. As mentioned above,

during the loading process the entire trap is on an offset of 250 V to slow the ions down while entering the trap. To open the trap, the front endcap is at 80 V and the moment the ions have passed the endcap, it is switch up to 260 V. After the ions are thermalized to the room temperature helium buffer gas pulse, the offset is ramped down slowly to 30 V. The ramp of all electrodes is done parallely within 3 seconds, thus the ions' temperature is not affected. The lower offset has two main advantages. First the influence of grounded parts close to the trap is reduced. The second advantage is that the extraction potential height can be adjusted as needed. In Figure 14 **d** the extraction potential along the trap axis is shown.

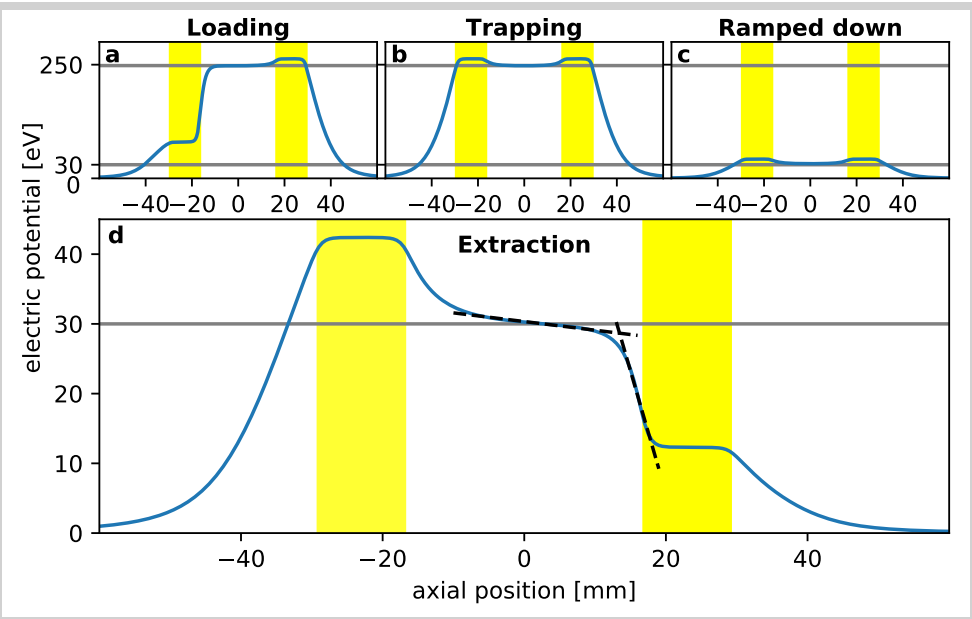

Figure 14: Potential along the axial axis during one measurement cycle. They yellows regions represents the endcap positions. **a**, the ions are loaded by opening the left endcap. The entire trap is on an offset of 250 eV to slow down the ions, which were accelerated by the Wiley-McLaren spectrometer. **b**, after the mass selected ions passed the endcap it is closed by applying a voltage 10 V above the offset. In this configuration the ions are thermalized to the 293 K helium buffergas. **c**, to reduce the influence of grounded metal parts into the trap and to optimize the extraction potential the entire trap potential is ramped down to an offset of 30 eV. This ramp is slow enough that the ions energy distribution is not effected. **d**, for extraction the right endcap is switched to 12 V and the left shaping electrode from 103 V, which generated a small slope in the trap center and a high one close to the endcap (dashed black lines).

The potential landscape is similar to the one encountered in the Wiley-McLaren mass spectrometer. By adjusting the horizontal electrodes (endcaps and shieldings), the potential can be optimized to make the time of flight independent of the starting position (see Figure 7 in section 2.1.2.2). Approximating the extraction potential by linear functions, the only difference to the Wiley-McLaren spectrometer is the initial ion velocity along the axis of extraction. For small

ion velocities compared to the velocity gained by the electric field, one can add another term to the total time of flight, derived for a Wiley-McLaren mass spectrometer, equation 17:

$$t_0 = \frac{m}{E_0 q} v_0, \tag{27}$$

where E_0 is the electric field strength in the first acceleration region and v_0 the initial ion velocity along the extraction axis. This way one can directly map the axial velocity distribution onto the ions time of flight to the detector, which allows us to determine the ion ensembles' temperature much quicker than it is possible via photodetachment tomography.
The right endcap is set to 10 V to make use of the lensing effect of a cylindrical electrode and the following grounded mount. This way, the extraction efficiency was improved.

2.1.4.1 *COMSOL and Monte-Carlo simulation of extraction*

A more detailed look into the extraction is done by a full trajectory simulation from the trap to the detector. Therefore, it also includes the radial degrees of freedom, the non-linearity of the extraction potential, the ions optics after the trap and the detector's acceleration field. The ions' velocity vector are randomly sampled from a Maxwell-Boltzmann distribution. The position is also randomly sampled from a thermal distribution in the trapping potential ($\rho(x,y,z) \propto \exp\left[-\frac{V(x,y,z)}{k_B T}\right]$). For each sampled ion, the full trajectory is calculated by solving Newton's equation of motion and the time of flight to the detector is saved. The calculated times are binned and fitted by a Gaussian function. Figure 15 shows the simulated variance in the TOF as a function of initial ion temperature in the trap. As expected the velocity is mapped linearly to the time of flight and therefore the temperature linearly mapped to the TOF's variance. However, deviations are seen at lower temperatures and the linear fit through all simulated points above 100 K is not matching a variance of zero at 0 K. This can be explained by neglecting the radial degrees of freedom in the earlier very simplified approach. In case of an ion distribution including only the axial position and the axial velocity, one could not see this deviation from the linear fit. In the following measurements, the ions' temperature is determined via measuring the arrival time of the ions at the detector, binning those times and fitting it with a Gaussian function. The temperature is then calculated by the two linear fits, shown in Figure 15. Temperature above 60 K are described by:

$$\sigma^2_{\mathrm{TOF}} = 0.00100(2)\ [\mu s^2/K] \cdot T + 0.025(3)\ [\mu s^2], \tag{28}$$

and below 60 K down to 1 K are well described by:

$$\sigma^2_{\mathrm{TOF}} = 0.00120(3)\ [\mu s^2/K] \cdot T + 0.0118(5)\ [\mu s^2]. \tag{29}$$

Figure 15 **b** shows the TOF distribution corresponding to the tomography measurements in the earlier section (see Figure 12). The resulting temperature

determined from this TOF is $T = 370(12)$ K, which is in accordance with the temperature calculated by the molecular dynamics simulation in the potential landscape $T = 373$ K (section 2.1.2.4).

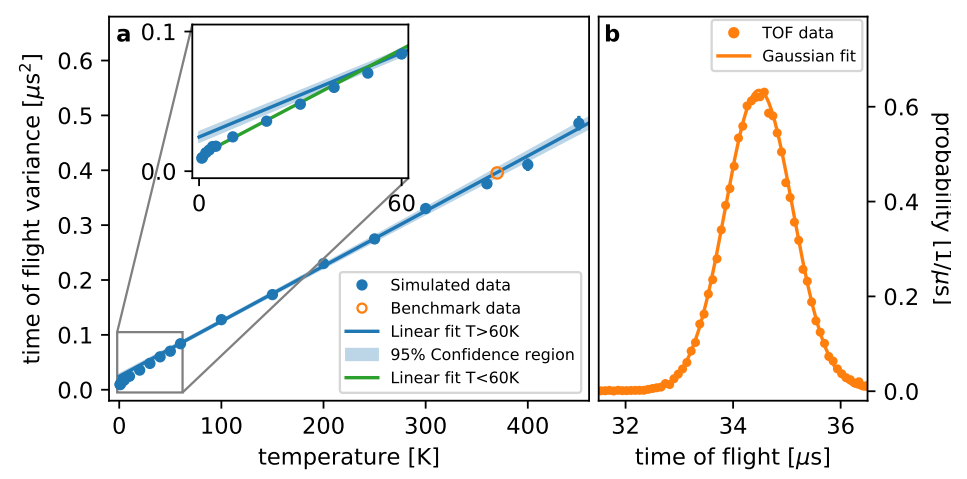

Figure 15: Time of flight thermometry. **a**, the simulated time of flight variance, i.e. the squared width of a Gaussian function, as a function of the ions' initial temperature in the trap before extraction. For temperatures below 60 K the calculated TOF variance deviates from the linear dependency at higher temperatures, (see inset). This dependency is well described down to 1 K by a second linear fit (green). The orange open circle corresponds to the measured time of flight distribution, shown in **b**, which results in $T = 370(12)$ K, matching very well with the expected value $T = 373$ K (see section 2.1.2.4).

2.1.4.2 *Detection efficiency*

The total ion number in the ion trap can be estimated by the ion-ion thermalization rate, which is dependent on the ion density. To determine this thermalization rate, the system was brought out of equilibrium by a high intensity photodetachment pulse of 200 ms. For high intensities, the photodetachment loss rate is much larger than the thermalization rate, which results in a depletion of distinct region in the energy distribution. The photodetachment laser beam is positioned axially at σ_z of the Gaussian shaped distribution. In the inset of Figure 16 one can see, that the TOF distribution of the ions extracted directly after the photodetachment pulse deviates from the Gaussian distribution, expected for a thermal distribution. This distribution is well represented by a q-Gaussian function, which is defined as following:

$$P(t) = \left(1 + (1-q)\left(-\frac{(t-t_0)^2}{2\sigma_q^2}\right)\right)^{\frac{1}{1-q}}, \tag{30}$$

with σ^2 being a measure for the energy, similar to the TOF thermometry. With increasing time, the ions are trapped after the photodetachment pulse, the ions

rethermalize and the TOF can be represented by a normal distribution again. Figure 16 shows the evolution of σ_q^2 with increasing trapping time after the photodetachment pulse. To determine the rethermalization rate the measured data is fitted by an exponential fit, which yields a rate of $k = 0.431(2)\ \mathrm{s}^{-1}$. For like-particle plasma the thermalization rate can be approximated by the Chandrasekhar-Spitzer self-collision rate [80]:

$$\nu_{\mathrm{ii}} = \frac{N e^4 \log \Lambda_{\mathrm{ii}}}{12 V_{\mathrm{i}} \epsilon_0^2 \sqrt{\pi^3 m_{\mathrm{i}} (k_{\mathrm{B}} T)^3}}, \tag{31}$$

with
- N → number of ions,
- $\log \Lambda_{\mathrm{ii}}$ → Coulomb logarithm,
- V_{i} → ion cloud volume,
- m_{i} → ion mass,
- ϵ_0 → vacuum permittivity.

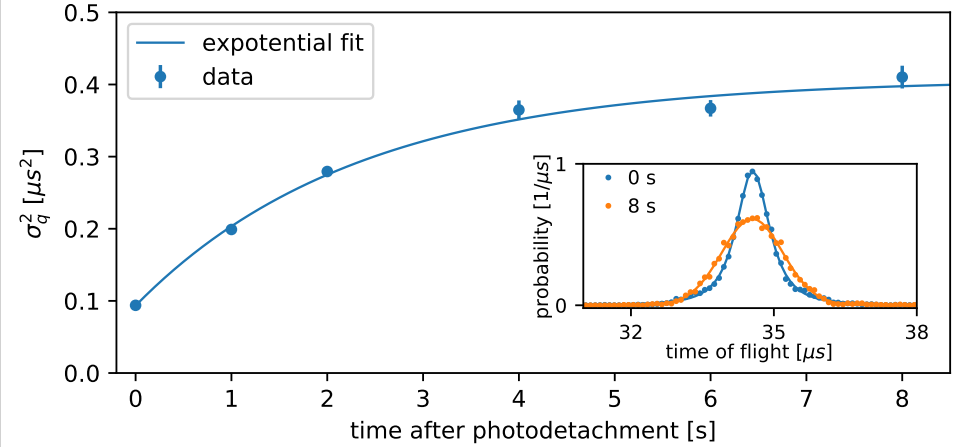

Figure 16: Width of the ions' time of flight distribution as a function of time after a 200 ms high-intensity photodetachment light pulse, which brings the ion cloud out of equilibrium. The width is determined by fitting a q-Gaussian to the TOF distribution (see equation 30). The inset shows the measured TOF distribution and the corresponding q-Gaussian, directly after the pulse and after 8 seconds. The thermalization is fitted by an exponential function, yielding a thermalization rate of $k = 0.431(2)\ \mathrm{s}^{-1}$.

The ion volume is measured via photodetachment tomography and the thermal energy $k_{\mathrm{B}}T$ can be estimated to be constant, because the energy of the ions, which were depleted, corresponds to the mean energy (see in detail section 3.1.1). Therefore the only free parameter is the absolute number of ions in the trap. With the mean detected amount of ions ($\bar{N}_{\mathrm{det}} = 11.7$ ions), the detection efficiency of the setup can be estimated to be 7.9 %. This rather low efficiency matches the efficiency calculated in the extraction trajectory simulations. The ion loss is caused by the large distance between the ion trap and the guiding ion optics after it. The ions leave the trap in a divergent

manner and therefore, only a small amount of them reach the Einzel lens, which focuses the ions onto the detector.

2.2 TRAPPING OF ATOMS

This section explains the fundamental principle of a magneto-optical trap (MOT) and discusses the implementation of a dark spontaneous force optical trap (darkSPOT) for rubidium in the HAITrap setup. Section 2.2.1 gives an introduction into atom cooling by light and how the atoms can be trapped, adding an inhomogeneous magnetic field. An overview of the atom trap setup is presented in section 2.2.2. It includes the description of the atom source and the darkSPOT design. The laser light preparation, however, is not discussed in the work. A detailed description of it can be found in an earlier work [81]. The third section 2.2.3 discusses the atom cloud characterization, based on saturation absorption imaging of ultracold dense atom clouds [82, 83]

2.2.1 CREATION OF AN ULTRACOLD ATOM CLOUD

Each photon carries a momentum $\hbar\mathbf{k}$, which gets transferred to the atom in case of absorption, when the two particle collide. The excited atom stores the momentum until the moment of spontaneous or stimulated emission. In case of spontaneous emission the recoil direction is random. Now for an atom in a laser beam, which is near-resonant but slightly detuned by $\delta = \omega_l - \omega_a$, where ω_a is the atomic resonance frequency and ω_l the laser frequency. The frequency the atom sees depends, however, on the atoms velocity in the direction of the propagating light. In the atoms reference frame, the laser frequency is Doppler shifted by $\delta = \mathbf{k}\mathbf{v}_a$, with $\mathbf{v}_a$ being the atoms velocity and $\mathbf{k}$ the wave vector. Therefore the absorption probability is dependent on the atom's velocity and is the highest, when the Doppler shift equals the detuning of the laser light from the atom's resonance frequency. For a red-detuned laser light, the atom's probability of absorbing a photon is higher, if it moves towards the propagation direction of the light, than in the opposite direction. Adding one red-detuned laser beam, with an opposing propagation direction, the atom is decelerated along this dimension. This principle can be expanded in three dimensions, that the optical forces always work against the movement of the atom. An atom gas with a strongly damped motion in such a configuration is called "optical molasses". Although, the atoms are cooled and can stay for a long time in the intersection region of the six laser beam, there is no restoring force, which traps the atoms. The spatial confinement can be introduced by superimposing the six laser beams with a magnetic quadrupole field, generated by an anti-Helmholtz configuration. The coils are placed such, that the field-free region of the quadrupole field is at the position, where the laser beams intersect. The linear inhomogeneous magnetic field causes a position-dependent Zeeman splitting of the atomic sub-levels and therefore, different transition frequencies depending on the laser light's polarization. For circular polarized light, this results in a position-dependent transition frequency.

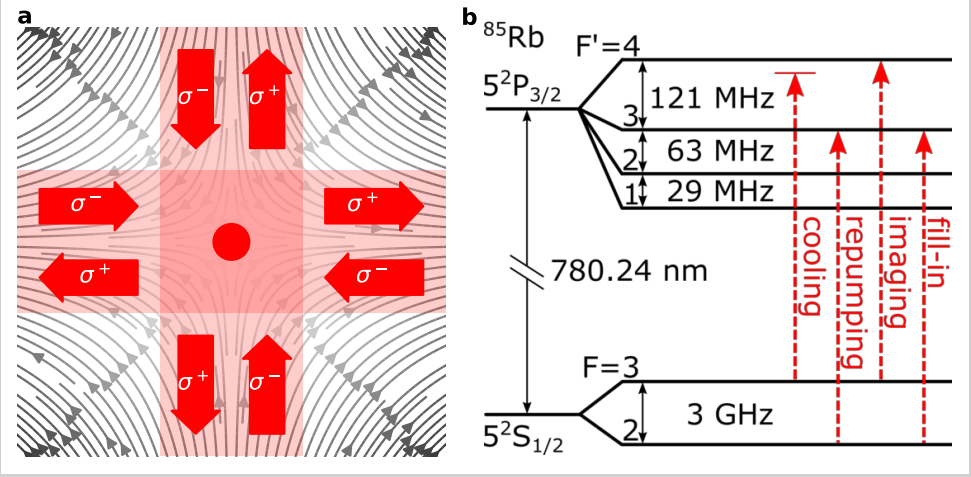

Figure 17: Principle of a magneto-optical trap. **a**, two dimensional illustration of a magneto-optical trap. The arrowed gray lines represent the magnetic quadrupole field generated by an anti-Helmholtz configuration. The red areas schematically show the counter-propagating laser beams and the red arrows show the direction of light propagation and its polarization with respect to the local magnetic field. The red circle illustrates the trapped atom cloud. **b**, laser frequencies required in the realization and detection of a MOT, trapping ^{85}Rubidium. Adapted from [84].

Figure 17 shows schematically a quadrupole field in the central plane between the two coils and the opposing laser beams. The circular polarization of the light is labeled with σ^- and σ^+ to indicate the rotation direction in respect to the local magnetic field. With increasing magnetic field the σ^+ transition becomes more unlikely than the σ^-, because the transition frequency for σ^+ polarized light is shifted up and for σ^- down, closer to the laser light frequency. This results in a net force, which points towards the magnetic field free region. This combination of light forces and an inhomogeneous magnetic field is called magneto-optical trap (MOT).
In the HAITrap experiment, the ultracold atom specie is the Rubidium 85 isotope. Figure 17 b shows the relevant energy levels and laser frequencies for optical cooling via the D_2 line:

$$5^2S_{1/2}(F=3) \rightarrow 5^2P_{3/2}(F'=4), \tag{32}$$

which is called the cooling transition. The cooling light frequency is, as mentioned above, red-detuned in respect to the transition frequency. Unfortunately, the excited state levels $(F'=4)$ and $(F'=3)$ are separated by only 121 MHz, which allows the excitation also into the lower state. In contrast to $F'=4$, $F'=3$ can relax to the lower ground state $5^2S_{1/2}(F=2)$. These atoms are then lost, because they are not addressed by the cooling light. With a second laser light frequency this problem can be overcome. The second frequency is on-resonance with the following transition:

$$5^2S_{1/2}(F=2) \rightarrow 5^2P_{3/2}(F'=3), \tag{33}$$

and is called repumper. This way the atoms in the lower ground state (dark state) are pumped back into the cooling cycle. The other frequencies shown Figure 17 are the ones of the imaging light, used in section 2.2.3 to characterize the atom cloud. The other one is similar to the repumper, but differs in its purpose.

2.2.2 DARK SPONTANEOUS FORCE OPTICAL TRAP

The atom trap used in the HAITrap experiment is in a dark spontaneous force trap (darkSPOT) configuration [85]. This special configuration allows to increase the atom density and reduce the amount of excited atoms. The density in a classic MOT designs is limited by two effects. First during a two-body collision of an excited and a ground state atom, the excitation energy can be transferred into kinetic energy, which would lead to an atom loss from the trap. The second effect is caused by spontaneously emitted photons, of random direction and polarization, which can excite neighboring atoms and therefore transfer random momenta. At a certain density, the isotropic force of the spontaneous photons balance the trapping force of the MOT.
In the darkSPOT configuration, the repumping light in the atom trap center is reduced and therefore the amount of atoms in the dark state ($5^2S_{1/2}(F = 2)$) is increased. As long as the atoms are in the dark state, they can not scatter the cooling light. This way, both limitations of the standard MOT are overcome, because both the amount of excited atoms and the spontaneously emitted photons are reduced. As long as the atoms are in the dark state, they are technically not trapped anymore. That's why the repumping light is only reduced in the trap center. The moment the dark atoms are falling out of this region, they are pumped back into the cooling cycle.
Figure 18 represents the technical drawing of the HAITrap experiment in Heidelberg including the optics required for the realization of the Rubidium magneto-optical trap. The lower sketch schematically illustrates a cut through the trap chamber, showing all relevant parts of the atom trap. The two coils in the anti-Helmholtz configuration are generating the magnetic quadrupole field. Each coil has 12 windings and an inner diameter of 7 cm. With a distance of 12 cm, they generate a magnetic field gradient of 45 G/cm, operating with 80 Ampere current

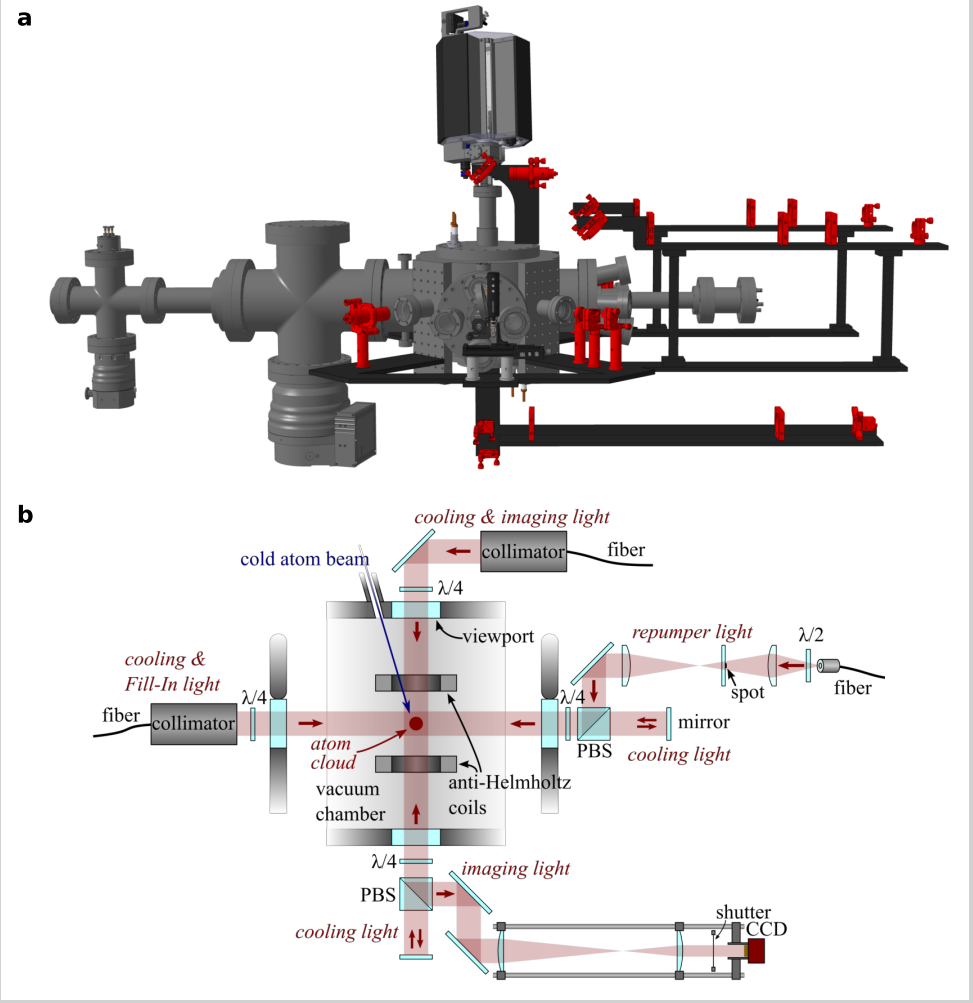

Figure 18: Atom trapping in the HAITrap setup. **a**, technical drawing of the HAItrap experiment, including all relevant optics, highlighted in red, required for the implementation of the atom trap in the trapping chamber. **b**, schematic cut through the trapping chamber, showing all necessary components of the atom trap. The prepared cooling light is transferred via optical fibers to fiber couplers at the experiment. The drawing shows, how the imaging setup and the darkSPOT arms are coupled in the MOT setup. Adapted from [82].

The atom source is a 2D-MOT attached to the cluster flange at the top of the trapping chamber. This source configuration is described in detail in [86]. It is also based on the principle of magneto-optical trapping in two dimensions. Figure 19 shows the setup used in the experiment. It consists of three trapping regions. The magnetic field, however, is in this case generated by permanent magnets, not shown in this graph. In the third dimension, the atoms can leave the glass cell through a differential pumping stage. This differential pumping stage creates a pressure difference of three orders of magnitude between the glass cell and the trapping chamber. This way the atom density in the glass cell is high enough to provide a sufficient atom flux. One might think that the velocity distribution in the third dimension is not effected, however, there is

a passive selection of colder atoms, because their time spent in the trapping regions is much larger than for hot atoms. The advantage of the 2D-MOT is that it provides a high flux of pre-cooled atoms, which allows a fast loading of a dense darkSPOT.

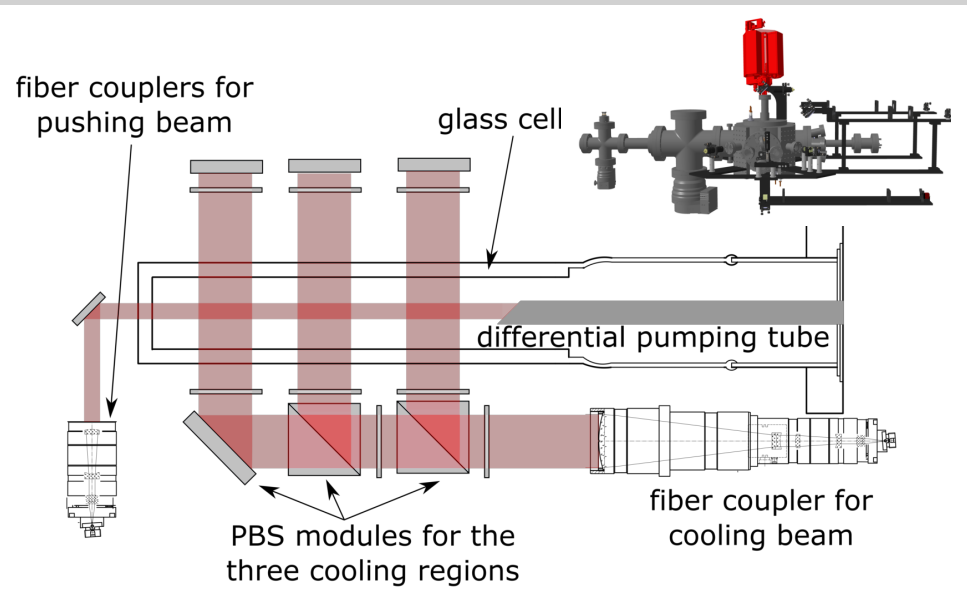

Figure 19: The 2D MOT is positioned at the top flange of the trapping chamber (highlighted in red in the inset). The drawing shows a cut through the central plane of the 2D MOT setup. The cooling and repumping light from an optical fiber is collimated and split into three arms via PBS cubes to generate three cooling regions. Adapted from [86].

The laser light preparation is done on a separate optical table, which is discussed in detail in [81]. From the optical table, the light is transported via optical fibers connected to fiber collimators at the setup. The collimated beams have a diameter of 24 mm ($1/e^2$). A quarter waveplate after the collimator is used to create a circularly polarized light. The light is passing through the chamber and another quarter waveplate and is retro-reflected. On the optical table, the cooling light and the fill-in light (repumping frequency) can be coupled into three fibers, which result in a classic three dimensional MOT.

The trap configuration can be switched into the darkSPOT mode, by switching off the fill-in light and coupling the two darkSPOT arms into the horizontal trapping beams via polarizing beam splitter (PBS) cubes. Figure 20 shows the optical setup of these darkSPOT arms and where they are placed in the technical drawing of the entire experiment. Repumping light is transferred via optical fibers to the darkSPOT arms. The fibers are mounted via a free-space fiber mount. Therefore the light exiting the fiber is divergent. A two lens setup allows to collimate the repumping light and image a mask into the trap center. The mask, being a spot in a glass plate, results in a reduction of repumping light in the atom trap center. To reduce scattered light from the ion trap's wires, the wires were added to the spot mask. The linearly polarized repumping

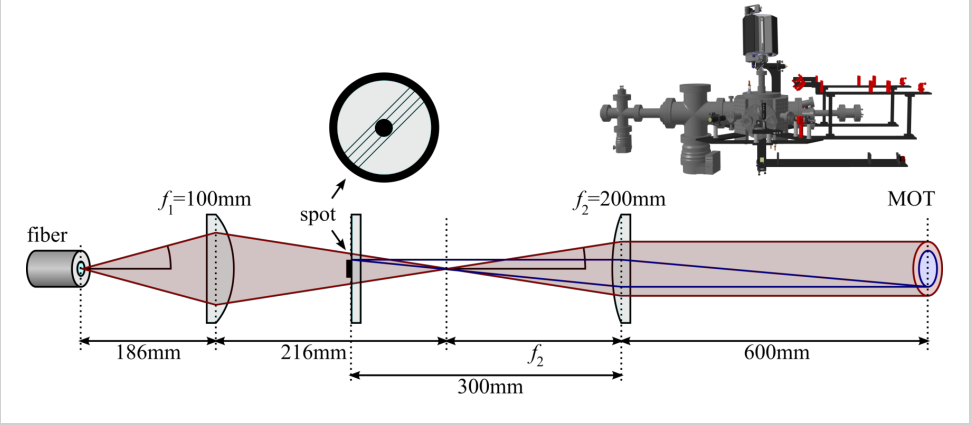

Figure 20: The darkSPOT arm setup is highlighted in red in the technical drawing. The divergent repumping light from an optical fiber is collimated by a two lens setup. This way, the mask placed between the lenses is imaged onto the plane of the MOT, reducing the repumping light in the atom trap center and on the ion trap's wires. Adapted from [82].

light can than be included into the 3D-MOT design by PBS cubes between the quarter waveplate and the retro-reflecting mirror.

2.2.3 DIAGNOSTICS VIA SATURATION ABSORPTION IMAGING

In order to investigate the atom-ion collision dynamics, a characterization of the atom cloud is needed. Two methods to determine the important parameters, as atom cloud size, atom number and density, are based on atom-light interaction. One approach is to count the photons scattered by the atoms. The other one is to image the shadow, created by atoms absorbing photons of a probe beam. In the HAITrap experiment, the latter method is used. The absorption imaging is coupled into the optical fiber to the vertical fiber coupler. In comparison to the cooling light, the imaging light's polarization is turned by 90°. This way, the light for both purposes, can be separated via a PBS cube after passing the trapping chamber. The cooling light is retro-reflected and the probe light is imaged by a 4f-system onto a CCD camera (see Figure). The following sections explain, how the atom cloud parameters are derived from these shadow images.

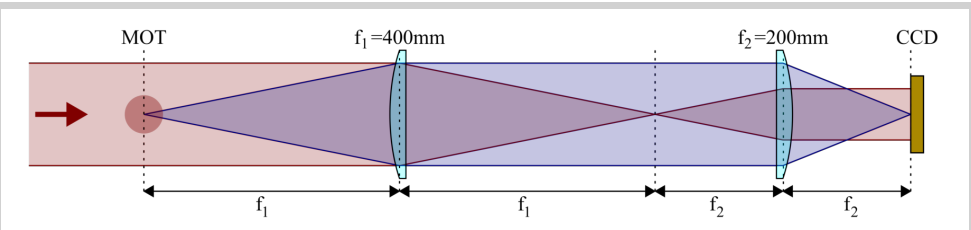

Figure 21: Schematic representation of the 4f absorption imaging setup used for the characterization of the atom cloud. Adapted from [82].

2.2.3.1 *Atom-light interaction*

Assuming a two-level energy system and a monochromatic light field, the population dynamics can be described by the optical Bloch equations [87]. In the steady state case the population of the excited state is given by:

$$\rho_{ee}(t \to \infty) = \frac{(\Omega/\Gamma)^2}{1 + 4(\Delta/\Gamma)^2 + 2(\Omega/\Gamma)^2}, \tag{34}$$

with $\Omega \quad \to$ Rabi frequency,
$\Gamma \quad \to$ natural linewidth,
$\Delta = \omega_l - \omega_a \quad \to$ detuning from resonance.

Since in steady state, the decay rate Γ equals the excitation rate, the total scattering rate is described by:

$$R_{sc} = \Gamma\rho_{ee}(t \to \infty) = \left(\frac{\Gamma}{2}\right) \frac{(I/I_{sat})}{1 + 4(\Delta/\Gamma)^2 + (I/I_{sat})}, \tag{35}$$

with $I \quad \to$ light intensity,
$I_{sat} = \frac{c\epsilon_0\Gamma^2\hbar^2}{4\|\hat{\epsilon}\cdot\mathbf{d}\|^2} \quad \to$ saturation intensity,
$c \quad \to$ speed of light,
$\epsilon_0 \quad \to$ vacuum permittivity,
$\hat{\boldsymbol{\epsilon}} \quad \to$ unit polarization vector
$\mathbf{d} \quad \to$ atomic dipole moment.

Therefore, the scattering rate does not only depends on the light intensity and detuning, but the atomic alignment and the polarization of the light also influence the rate. That becomes particularly relevant, if multiple magnetic sub-levels are populated. For example, the cooling transition in ^{85}Rubidium the ground state ($5^2S_{1/2}(F = 3)$) consists of seven degenerate sub-levels and the excited state ($5^2P_{3/2}(F' = 4)$) of nine. For the purpose of a well-defined quantization axis, one applies a homogeneous magnetic field, by switching the current of the two coils. The atoms are pumped into the stretched state ($m_F = 3$) by shining in σ^+ polarized light, because the angular momentum has to be conserved during absorption of a photon. The procedure is called optical pumping and it generates a two-level probe transition between ($F = 3$, $m_F = 3$) and ($F' = 4$, $m_F = 4$).
In the darkSPOT configuration (see section 2.2.2) a large amount of atoms are in the dark state ($F = 2$), which can not absorb the probe light. For this reason, before the imaging process the cooling light is switched off and all dark state atoms are pumped back into the bright state($F = 3$) by the so called fill-in light on the repumping transition. Including this step all atoms are probed. Excluding it probes only the atoms in the bright state. The difference between both measurements gives an estimate of the atoms in the dark state.

2.2.3.2 *Standard absorption imaging*

The intensity of a probe beam on-resonance with the atomic transition is changed while passing through an atom cloud. This change in intensity is caused by photon scattering in consideration with equation 35, is given as:

$$\frac{\mathrm{d}I(x,y,z)}{\mathrm{d}z} = n_\mathrm{a}(x,y,z)\left(\frac{\Gamma}{2}\right)\frac{\hbar\omega_\mathrm{l}(I/I_\mathrm{sat})}{1+(I/I_\mathrm{sat})} \tag{36}$$

with $I \rightarrow$ light intensity distribution,
$n_\mathrm{a}(x,y,z) \rightarrow$ atom density distribution.

In the case of absorption imaging setup in the HAITrap experiment, the probe light propagates along the z-axis and is imaged onto a CCD camera. Thus, a shadow appears on the image, where the light passes the atom cloud. For small probe light intensities ($I \ll I_\mathrm{sat}$) the intensity decay passing through the atom cloud is described by an exponential decay along the z-direction, as follows:

$$I(x,y,z) = I_0(x,y)\exp\left[-\frac{\Gamma\hbar\omega_\mathrm{l}}{2I_\mathrm{sat}}\int_{-\infty}^{z} n_\mathrm{a}(x,y,z')\mathrm{d}z'\right], \tag{37}$$

with $I_0(x,y)$, being the probe beam intensity distribution before the atom cloud. Thus, by taking an image with and without atoms, one can derive atom cloud parameters, like the width along x- and y-direction and the atoms column density $n_\mathrm{col}(x,y) = \int_{-\infty}^{\infty} n_\mathrm{a}(x,y,z)\mathrm{d}z$. The atom's column density is directly proportional to the optical density:

$$\mathrm{od}(x,y) = -\ln\left[\frac{I(x,y)}{I_0(x,y)}\right] = \frac{\Gamma\hbar\omega_\mathrm{l}}{2I_\mathrm{sat}} n_\mathrm{col}(x,y). \tag{38}$$

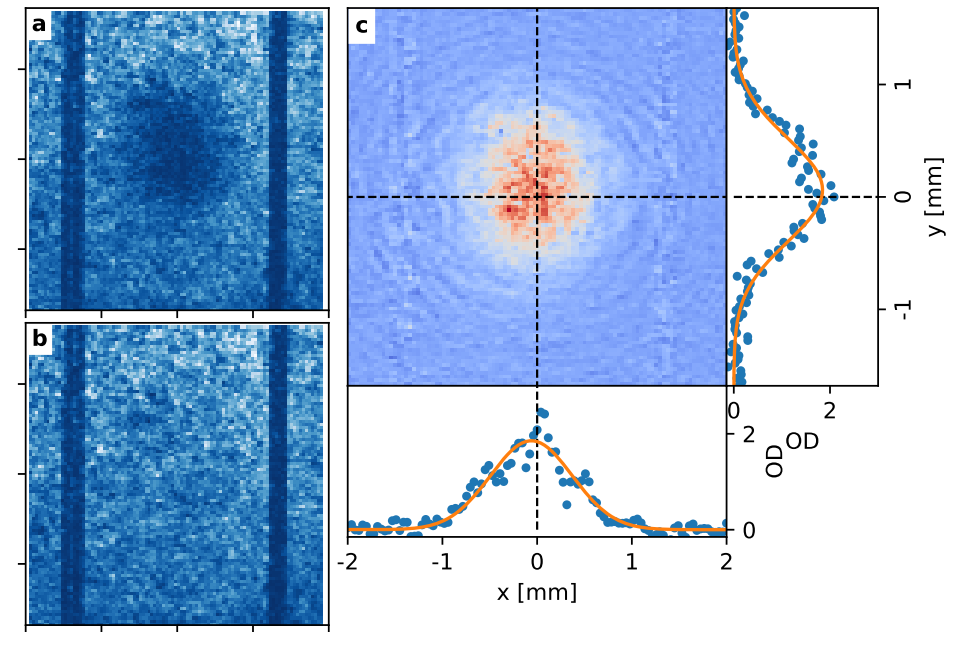

Figure 22: Determination of the optical density in the atom cloud characterization. **a**, and **b**, show the raw pictures taken by the CCD camera with and without the atom cloud, respectively. **c**, corresponds to the optical density calculated by plugging in the raw data pictures into equation 38. Also shown are two cuts through the atom cloud center and corresponding to those cuts, the fitted two-dimensional Gaussian function in orange.

Figure 22 shows a typical absorption imaging measurement in the HAITrap experiment. Panel **a** depicts raw data taken by the CCD camera with atom cloud and **b** without. The two dark vertical bars are shadows created by the ion trap's wires. Panel **c** shows the optical density calculated following equation 38. Also shown in **c** are cuts along x- and y-direction through the atom cloud center. The data is fitted with a two dimensional Gaussian function, deriving the atom cloud widths $\sigma_{a,x}$, $\sigma_{a,y}$ and the peak optical density $\mathrm{od}_{\mathrm{peak}}$. The atom number N_a can be calculated as follows:

$$N_a = \int_{-\infty}^{\infty}\int_{-\infty}^{\infty}\int_{-\infty}^{\infty} n(x,y,z)\mathrm{d}x\mathrm{d}y\mathrm{d}z \tag{39}$$

$$\overset{\text{eq. 38}}{=} \int_{-\infty}^{\infty}\int_{-\infty}^{\infty} \mathrm{od}(x,y)\frac{2I_{\mathrm{sat}}}{\Gamma\hbar\omega_l}\mathrm{d}x\mathrm{d}y \tag{40}$$

$$= 2\pi\sigma_{a,x}\sigma_{a,y}\mathrm{od}_{\mathrm{peak}}\frac{2I_{\mathrm{sat}}}{\Gamma\hbar\omega_l}. \tag{41}$$

The peak atom density n_0 can then be determined by:

$$n_0 = \frac{N_a}{(2\pi)^{3/2}\sigma_{a,x}\sigma_{a,y}\sigma_{a,z}}. \tag{42}$$

Since only the atom's column density is measured with this technique, there is no information given about the atom cloud's width along the z-axis, $\sigma_{a,z}$. By a fluorescence measurement perpendicular to the absorption imaging axis, it

was confirmed that the atom cloud is well approximated to be spherical. In course of this work, the expansion of the atom cloud along the z-direction is assume to be:

$$\sigma_{a,z} = \frac{\sigma_{a,x} + \sigma_{a,y}}{2}. \tag{43}$$

2.2.3.3 *Saturated absorption imaging*

Since the optical density is proportional to the atom column density, it becomes quite large for high density atom clouds. For such optically thick clouds, optical pumping (see section 2.2.3.1) is not feasible anymore and one has to take all populated sub-levels into account. Thus, each individual sub-level results in an individual saturation intensity I_{sat,m_F} and population p_{sat,m_F}, which adds up to a total scattering rate:

$$R_{sc} = \left(\frac{\Gamma}{2}\right) \sum_{m_F} p_{sat,m_F} \frac{(I/I_{sat,m_F})}{1 + (I/I_{sat,m_F})}. \tag{44}$$

The sub-level distribution is unknown, and as long as the system is not pumped into a stretched state, it is impossible to determine the scattering rate in equation 44. This problem can be overcome by combining all saturation intensities into one effective saturation intensity:

$$I_{sat,eff} = \alpha I_{sat}. \tag{45}$$

I_{sat} is in this case the saturation intensity for the stretched state and α is a scaling parameter, taking the real sub-level distribution into account. Therefore the total scattering rate is approximated as follows:

$$R_{sc} = \left(\frac{\Gamma}{2}\right) \frac{(I/\alpha I_{sat})}{1 + (I/\alpha I_{sat})}, \tag{46}$$

which results in the same differential equation for the intensity as equation 36, by replacing I_{sat} by $I_{sat,eff}$.

The scaling parameter α can be determined by measuring the optical density over a large intensity range. Solving equation 36, including the effective saturation intensity, yields:

$$od(x,y) = \alpha \ln\left[\frac{I(x,y)}{I_0(x,y)}\right] + \frac{I_0(x,y) - I(x,y)}{I_{sat}}. \tag{47}$$

The optical density is dominated by the first term for small intensities. It corresponds to the result of the two-level energy system (see equation 38) corrected by the scaling parameter α. However, for large intensities the optical density is dominated by the second term and therefore independent of the scaling parameter.
To calibrate the α, one measures the optical density over a large range of the intensity. During this measurement, the atom cloud is not changed and therefore the optical density has to be independent on the intensity of the

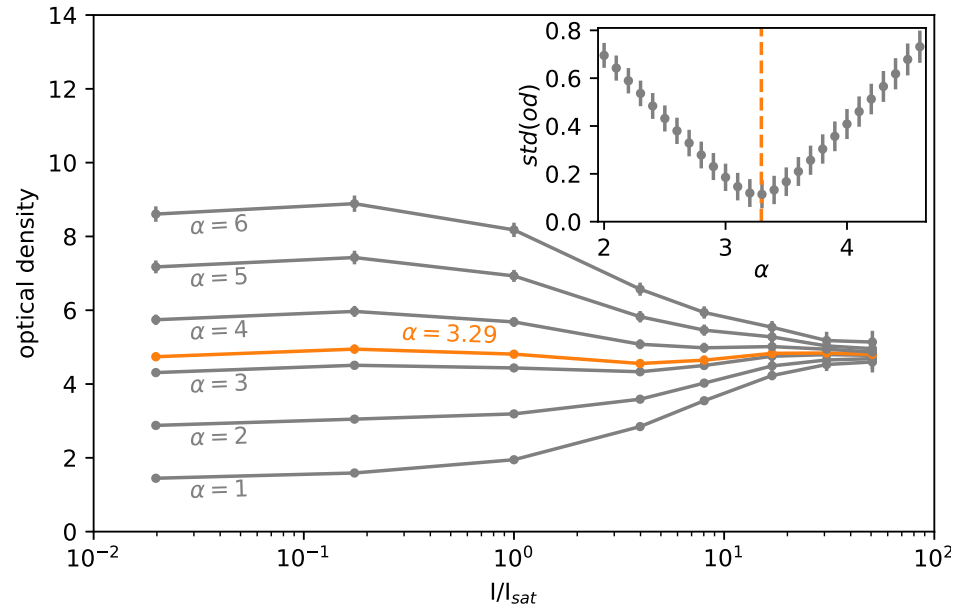

Figure 23: Optical density calculated with equation 47 for different values of α. Highlighted in orange is the result for $\alpha = 3.29$, which is the value with the lowest deviation in the optical density over the measured intensity range. The inset shows the standard deviation for different values of α, where the $\alpha = 3.29$ with smallest standard deviation marked as an orange dashed line .

probe light. The only free parameter of this measurement is then α, which can be determined, minimizing the deviation of the optical density over the entire intensity range. Figure 23 shows the calibration measurement of the atom imaging for the HAITrap setup from $I/I_{sat} = 0.02$ to $I/I_{sat} = 51$. The inset shows the standard deviation of the optical density. It is the smallest at $\alpha_0 = 3.29$.
A CCD camera has a finite dynamical range, which is in the experimental setup 8 Bit ($2^8 = 256$). Therefore the camera can only resolve atom clouds with a maximum optical thickness of $\ln[256] \approx 5.55 = \mathrm{od}_{\mathrm{max}}$. This limitation can be circumvented by detuning the probe light and therefore reducing the scattering rate. This can be expressed in a detuning dependent scaling parameter:

$$\alpha(\Delta) = \alpha_0 \left(1 + 4\left(\frac{\Delta}{\Gamma}\right)^2\right), \tag{48}$$

where α_0 is the scaling parameter on-resonance as measured above, Δ is the detuning of the probe light compared to the resonance and Γ the natural linewidth (see scattering rate: equation 35). This way even denser atom clouds can be characterized. A detailed description of the detuned saturation absorption technique in this setup can be found in the following publication [83].

2.3 CO-TRAPPING OF ANIONS AND ATOMS

The co-trapping of molecular anions and atoms yields three types of collisions, which can occur:

- *elastic collisions*. During an elastic collision between an atom and an ion, kinetic energy is exchanged. Depending on the relative velocity and mass, the ion can gain or lose translational energy.
- *reactive collisions*. During a reactive collision a new specie is formed, which eventually leads to a loss of the anion and the atom. For example, during a collision in the Rb-OH^- system, an associative detachment reaction can occur by stabilizing the rubidium hydroxide neutral molecule, due to the loss of the excess electron.
- *inelastic collision*. During an inelastic collision, internal energy of the molecular anion and the relative kinetic energy is exchanged. In comparison to the sympathetic cooling via Coulomb interaction, in an atom-ion collision the encounter is much closer, which leads to sufficiently high inelastic state-changing rate coefficients [26, 88].

The first two types of collisions dominate the sympathetic cooling dynamics of rubidium with OH^- and naturally also with O^-. Therefore, the elastic and reactive collision dynamics are described in detail in chapter 4.
A common description of the collision dynamics between atoms and ions is the classical Langevin capture model [89], in which the collision cross section scales with $\sigma \propto E_{\mathrm{col}}^{-1/2}$, yielding a velocity-independent collision rate coefficient k. Thus, the rate for an ion to collide with an atom is given by this scattering rate and the integral over the overlap, $\Phi_{\mathrm{ia}}(x,y,z)$, of both clouds:

$$\nu_{\mathrm{coll}} = k \int \underbrace{\rho_{\mathrm{i}}(x,y,z) n_{\mathrm{a}}(x,y,z)}_{\Phi_{\mathrm{ia}}(x,y,z)} \mathrm{d}x\mathrm{d}y\mathrm{d}z, \tag{49}$$

where ρ_{i} is the normalized ion density distribution and n_{a} the absolute atom density distribution. Note, that the scaling of the cross section in the Langevin capture model is a simplification, which is valid for high relative collision energies. For collision energies at which the matter-wave nature of the collision partners becomes relevant, the collision rate becomes indeed energy-dependent [90]. Finally, to quantify any collision dynamics it is crucial to know the temporal evolution of their overlap and therefore, the relative positioning of both clouds.
In the course of co-trapping both, anions and atoms, the anions are trapped first, since in their loading procedure, a helium buffer gas pulse is introduced into the trap region (see section 2.1.2.4). The helium pulse leads to an increase in the background gas pressure, which would eventually lead to a loss of the trapped atoms. The time necessary to ramp down the initial trap offset is sufficiently long enough to reduce the background pressure again to 10^{-9} mbar. With reaching these conditions, the atom trap is loaded, by switching on the

cooling light. Figure 24 illustrates schematically a co-trapping measurement cycle. After a given interaction time between both species, the ions are extracted towards the detector and the atom cloud is characterized via saturation absorption imaging.

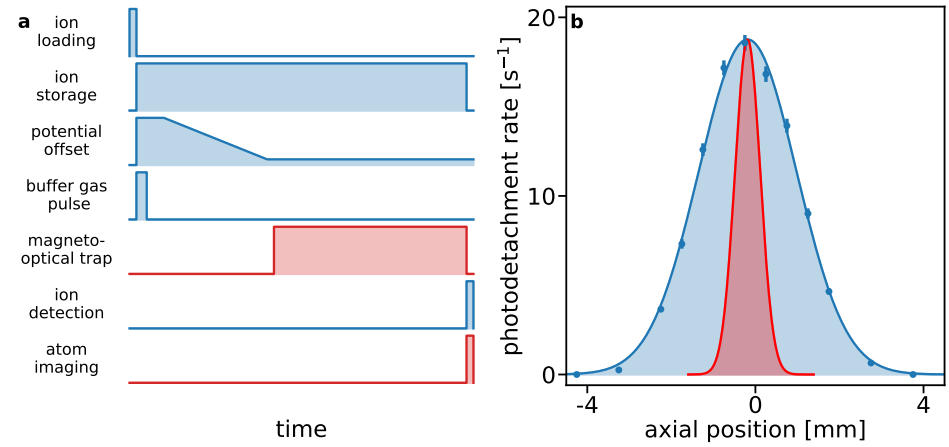

Figure 24: Procedure of reactive loss measurements. **a**, schematic representation of the experimental measurement cycle. The ion initialization includes the loading, the thermalization to the helium buffer gas and the potential manipulation. Subsequently, the atom cloud is loaded concentric to the ion distribution. After a certain interaction time, the atom cloud is characterized via saturation absorption imaging and the ions are extracted to the detector. **b**, the blue region shows the ion distribution measured via photodetachment tomography. The red distribution illustrates the typical extent of the atom cloud.

2.3.1 TEMPORAL EVOLUTION OF THE ATOM-ANION OVERLAP

Due to elastic collision of anions with the ultracold buffer gas, the temperature of the ion ensemble changes with time, also altering the ions' density distribution. Additionally the atom trap is loaded in the same timescale as the typical interaction time between the two species. Thus, the change in atom density and cloud size have to be taken into account. This time-dependent overlap function is described as following:

$$\Phi_{x,y,z,t} = n_a(x,y,z,t)\rho_i(x,y,z,T(t)). \tag{50}$$

Figure25 shows an exemplary case for the determination of the overlap function, between the ultracold rubidium cloud and trapped OH^- anions.

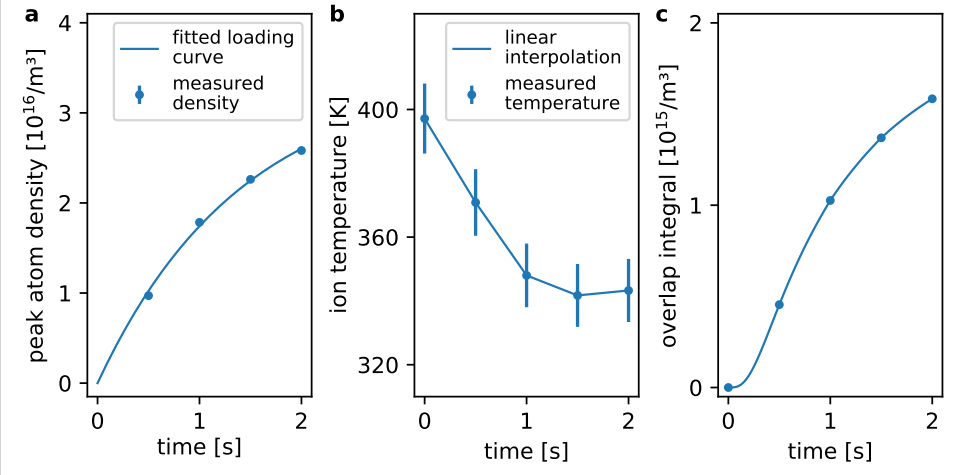

Figure 25: Determination of the time-dependent atom-ion overlap integral. **a**, shows a typical atom loading curve. The solid points represent the measured peak atom densities as a function of loading time. The solid line shows the exponential loading function fitted to the data points, with a loadting time $\tau_{\text{load}} = 1.41(16)$ seconds. **b**, shows the evolution of temperature, due to elastic atom-ion collisions. The solid points are measured via TOF thermometry. **c**, shows the time-dependent overlap integral, determined by taking the atom cloud loading and the ion temperature evolution into account.

The atom cloud loading is well-described by an exponential loading function $n_{\text{a,peak}}(t) = n_{\text{a,0}}\,(1 - \exp(-t/\tau_{\text{load}}))$, the the loading time of $\tau_{\text{load}} = 1.41(16)$ seconds. Since the atom size also increases with time, it has been fitted in the similar way, deriving a growth time of $\tau_{\text{growth}} = 0.23(4)$ seconds. The ions' temperature is derived via their time of flight distribution to the detector. The ions' density distribution can then be calculated by a thermal distribution in the predetermined trapping potential. The potential characterization is done, by a far-threshold photodetachment benchmark measurement, in which the spatial distribution of the anions, thermalized to helium, in both directions is measured, see section 2.1.3. The corresponding temperature is determined via time of flight thermometry for the data taken without interaction with the photodetachment light. The ion trap potential is well-approximated by a harmonic potential in axial direction and a r^6-potential in radial direction. Assuming a thermal distribution, yields the following trapping potential:

$$\begin{aligned} V_{\text{OH}^-}(x,y,z) =& 1.94(11)\cdot 10^{-15}\ \text{J/m}^2\cdot z^2 + \\ &+ 4.1(2)\cdot 10^{-3}\ \text{J/m}^6\cdot (x^2+y^2)^3. \end{aligned} \tag{51}$$

The normalized ion density $\rho_{\text{i}}(x,y,z,T)$ is then given by the thermal spatial distribution in this potential for a given temperature. By interpolating the ion temperature, Figure 25, one can derive the time-dependent integral of the overlap between the atom and the ion cloud.

2.3.2 CHARACTERIZATION OF RELATIVE ATOM-ANION POSITIONS

For the characterization of the overlap, it is indispensable to know the relative distance between the centers of both, the atom and the ion density distribution. Since the trap wires are also visible in the saturation absorption image, it is an easy task to align the atom cloud in one radial direction. In the other radial direction, the atom cloud is aligned by a camera, perpendicular to the trap. In axial direction, however, the two imaging diagnostic techniques, photodetachment tomography and saturation absorption imaging, for anions and atoms, respectively, have to be calibrated to each other. Two calibration methods have been carried out.

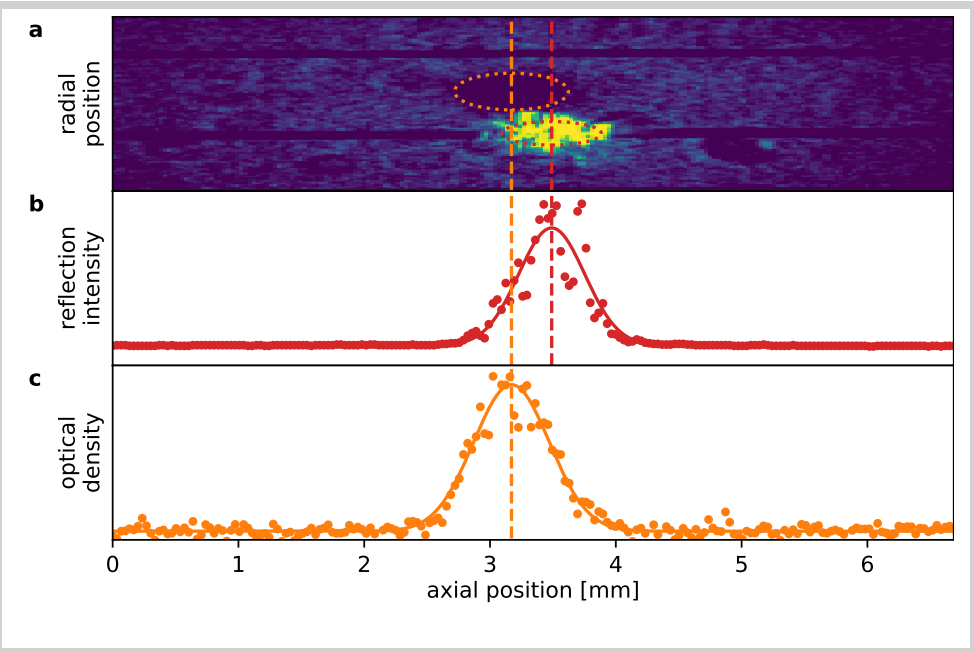

Figure 26: Calibration measurement to determine the relative distance between the atom cloud and the ion cloud. The photodetachment beam was placed such, that the light is reflected from an ion trap wire. **a**, absorption imaging picture showing the atom cloud induced shadow (orange dotted ellipse) and the reflected photodetachment light (red dotted ellipse). Radially the atom cloud is align in respect to the wires, also seen as shadows on the picture. **b**, cut through the picture along the lower wire. The dashed line represents the mean beam position, determined via a Gaussian function fitted to the data. This point connects the photodetachment laser beam position with the atom cloud imaging system. **c**, optical density of the shown atom cloud. The center position is determined via a fitted 2D-Gaussian function, corresponding to a relative position of $z = 0.03$ mm to trap center and $z = 0.31$ mm to the ions.

Figure 26 illustrate the first method, in which the photodetachment laser beam is vertically adjusted such, that the light is reflected by one wire. The reflected light is imaged onto the CCD camera of the saturation absorption imaging. This relates the position of the mechanical stage used for tomography, to the

position on the absorption imaging camera. This calibration has to be done only once, since then, a shift of the atom cloud can be determined with respect to the position of the ion cloud.
A cross check method has been carried out, replacing the optical fiber providing the photodetachment light with one optical fiber transmitting light, which is on-resonant with the ^{85}Rb cooling transition ($5^2S_{1/2}(F = 3) \rightarrow 5^2P_{3/2}(F' = 4)$). This focused laser beam leads to a depletion of fluorescing rubidium atoms at its positions. The tomography stage was then moved to the position, at which the point of depletion is in the atom cloud center, observed via a camera perpendicular to the ion trap. The second method confirmed the previously determined calibration. Since in the exemplary case of Figure 26 the photodetachment beam is placed at an absolute laser beam position of $z_{\text{tomo}} = 15.7$ mm and the ion trap center is at $z_{\text{tomo}} = 15.35$ mm, one can derive the ion trap center to be at $z_{\text{CCD}} = 3.14$ mm on the corresponding absorption imaging pictures. Note, that the ions are, due to surface charges (see sec 2.1.3.2), slightly displaced, yielding a concentric overlap of both clouds at $z_{\text{CCD}} = 2.97$ mm.

3

FORCED EVAPORATIVE COOLING VIA PHOTODETACHMENT

Forced evaporative cooling is a powerful and well-established tool for cooling atoms [91] and also cations [92]. This technique is based on selective removal of high-energy particles out of the trap. The rethermalization of the residual particles leads to a colder ensemble of the remaining trapped specie. Although forced evaporative cooling by energy selective removal via photodetachment was proposed more than three decades ago by Anne Crubellier [54], it has not been experimentally demonstrated.
This chapter presents forced evaporative cooling of molecular anions, OH^-, via photodetachment in an octupole rf trap and a complete thermodynamic model, which describes the temporal evolution of ion temperature and ion number without free fit parameters.
Section 3.1 discusses the derivation of a thermodynamic model detailing evaporation via far-threshold photodetachment. This discussion results in a set of differential equations for the evolution of the ion temperature and ion number, including parameters, which can all be independently determined in advance to predict the cooling dynamics.
Section 3.2 presents evaporative cooling and heating measurements for different photodetachment laser beam positions, inspired by the evaporative cooling measurements of G. Cerchiari et al. , who proposed laser-assisted evaporation as a precooling technique for direct Doppler cooling of La^- [57]. However, the cooling efficiency and rate of static evaporation is quite limited.
Section 3.3 shows the implementation of a forced evaporative cooling scheme via a movable far-threshold photodetachment beam and measurements taken for different beam velocities. The measurements are well-represented by the developed thermodynamic model. However, an additional heating term has to be introduced, covering the ion-ion rf heating. With this further development of the model, a full thermodynamic description for forced evaporative cooling via photodetachment of any weakly-coupled anion plasma in a multipole rf trap can be provided.

3.1 THERMODYNAMIC DESCRIPTION OF EVAPORATIVE COOLING

In this thermodynamic description of evaporative cooling of an anion ensemble, of a single specie with mass m and charge q, is considered. The ions interact with each other and therefore they are able to reach a thermal equilibrium. The photodetachment light is monochromatic and far above the threshold. It is assumed that the ions' thermalization time is much smaller than the evaporation time. Thus, the ions are at any time in thermal equilibrium.

3.1.1 EVOLUTION EQUATIONS

Following the Boltzmann-statistics, the ions' phase-space distribution is given by:

$$\rho(\mathbf{r},\mathbf{v}) = \frac{\exp\left[-(\frac{1}{2}m\mathbf{v}^2 + V(\mathbf{r}))/k_\mathrm{B}T\right]}{\int \exp\left[-(\frac{1}{2}m\mathbf{v}^2 + V(\mathbf{r}))/k_\mathrm{B}T\right] \mathrm{d}\mathbf{r}\mathrm{d}\mathbf{v}}, \tag{52}$$

with $\mathbf{r}$ and $\mathbf{v}$ $\rightarrow$ position and velocity,
$V(\mathbf{r})$ $\rightarrow$ ion trap potential,
k_B $\rightarrow$ Boltzmann constant,
T $\rightarrow$ ensemble temperature.

The total energy of a single ion is given by its kinetic energy $E_\mathrm{k} = \frac{1}{2}m\mathbf{v}^2$ and its potential energy $E_\mathrm{p} = V(\mathbf{r})$:

$$E_\mathrm{tot}(\mathbf{r},\mathbf{v}) = E_\mathrm{k}(\mathbf{v}) + E_\mathrm{p}(\mathbf{r}). \tag{53}$$

The trapping potential in axial direction is assumed to be harmonically shaped, whereas in radial direction the potential's form is dependent on the order of the rf trap ($V_\mathrm{radial}(r) \propto r^{2n-2}$). Taking the virial theorem into account the mean total energy is described by the following:

$$\left\langle\left\langle E_\mathrm{tot}\right\rangle_\mathbf{r}\right\rangle_\mathbf{v} = \left\langle E_\mathrm{k}\right\rangle_\mathbf{v} + \left\langle E_\mathrm{p}\right\rangle_\mathbf{r} = \frac{3}{2}k_\mathrm{B}T + \frac{1}{2}k_\mathrm{B}T + \frac{1}{n-1}k_\mathrm{B}T. \tag{54}$$

The first term corresponds to the kinetic energy of a point-like particle moving in the three-dimensional space, the second term to the axial potential energy and the third term to the radial potential energy.
Since the photodetachment light's frequency is far above threshold, the Doppler shift of the ion's motion is negligible and the photodetachment cross section ($\sigma_\mathrm{pd}(\mathbf{v}) = \sigma_\mathrm{pd}$) independent on the velocity. A detailed description of laser-induced evaporation close to the photodetachment threshold can be found in the publication of Anne Crubellier [54].
As mentioned in section 2.1.3.1 the ion loss, due to photodetachment, is described by the following first order differential equation:

$$\dot{N} = -N\left\langle\left\langle\sigma_\mathrm{pd}(\mathbf{v})I(\mathbf{r})\rho(\mathbf{r},\mathbf{v})\right\rangle_\mathbf{r}\right\rangle_\mathbf{v} \tag{55}$$

$$= -N\int_{-\infty}^{\infty}\sigma_\mathrm{pd}(\mathbf{v})I(\mathbf{r})\rho(\mathbf{r},\mathbf{v})\mathrm{d}\mathbf{r}\mathrm{d}\mathbf{v}. \tag{56}$$

and for $\sigma_\mathrm{pd}(\mathbf{v}) = \sigma_\mathrm{pd}$:

$$\dot{N} = -\sigma_\mathrm{pd}N\int_{-\infty}^{\infty} I(\mathbf{r})\rho(\mathbf{r})\mathrm{d}\mathbf{r}, \tag{57}$$

where $I(\mathbf{r})$ is the light intensity distribution, which can be assumed to be constant along the direction of the photodetachment beam. The time-dependent

total ion energy is given by product of the mean ion energy and the number of ions:

$$E_{\text{tot}}(t) = N(t)\left\langle\left\langle E_{\text{tot}}\right\rangle_{\mathbf{r}}\right\rangle_{\mathbf{v}}(t), \tag{58}$$

and the variation of the total energy corresponds to the energy removed with the lost ions:

$$\dot{E}_{\text{tot}} = -N\left\langle\left\langle \sigma_{\text{pd}} I(\mathbf{r})\rho(\mathbf{r},\mathbf{v})E(\mathbf{r},\mathbf{v})\right\rangle_{\mathbf{r}}\right\rangle_{\mathbf{v}}. \tag{59}$$

Eventually the change of the mean total energy is the following:

$$\left\langle\left\langle \dot{E}_{\text{tot}}\right\rangle_{\mathbf{r}}\right\rangle_{\mathbf{v}} = \frac{\dot{E}_{\text{tot}}}{N} - \frac{E_{\text{tot}}}{N^2}\dot{N}. \tag{60}$$

Plugging into this equation the variation of energy 59 and ion number 55 results in:

$$\begin{aligned}\left\langle\left\langle \dot{E}_{\text{tot}}\right\rangle_{\mathbf{r}}\right\rangle_{\mathbf{v}} &= -\left\langle\left\langle \sigma_{\text{pd}} I(\mathbf{r})\rho(\mathbf{r},\mathbf{v})E_{\text{tot}}(\mathbf{r},\mathbf{v})\right\rangle_{\mathbf{r}}\right\rangle_{\mathbf{v}} &(61)\\ &\quad + \left\langle\left\langle E_{\text{tot}}\right\rangle_{\mathbf{r}}\right\rangle_{\mathbf{v}}\left\langle\left\langle \sigma_{\text{pd}} I(\mathbf{r})\rho(\mathbf{r},\mathbf{v})\right\rangle_{\mathbf{r}}\right\rangle_{\mathbf{v}}. &(62)\end{aligned}$$

Since the phase-space density distribution in equation 52 is separable $\rho(\mathbf{r},\mathbf{v}) = \rho_{\text{r}}(\mathbf{r})\rho_{\text{v}}(\mathbf{v})$, plugging in equation 53 and 54 one can simplify the equation for the change of mean total energy as following:

$$\begin{aligned}\left\langle\left\langle \dot{E}_{\text{tot}}\right\rangle_{\mathbf{r}}\right\rangle_{\mathbf{v}} &= -\left\langle\left\langle \sigma_{\text{pd}} I(\mathbf{r})\rho_{\text{r}}(\mathbf{r})\rho_{\text{v}}(\mathbf{v})\left[E_{\text{p}}(\mathbf{r}) + E_{\text{k}}(\mathbf{v})\right]\right\rangle_{\mathbf{r}}\right\rangle_{\mathbf{v}} &(63)\\ &\quad + \left[\left\langle E_{\text{k}}\right\rangle_{\mathbf{v}} + \left\langle E_{\text{p}}\right\rangle_{\mathbf{r}}\right]\left\langle\left\langle \sigma_{\text{pd}} I(\mathbf{r})\rho_{\text{r}}(\mathbf{r})\rho_{\text{v}}(\mathbf{v})\right\rangle_{\mathbf{r}}\right\rangle_{\mathbf{v}}\\ &= -\sigma_{\text{pd}}\left\langle\rho_{\text{r}}(\mathbf{r})I(\mathbf{r})E_{\text{p}}(\mathbf{r})\right\rangle_{\mathbf{r}} + \sigma_{\text{pd}}\left\langle E_{\text{p}}\right\rangle_{\mathbf{r}}\left\langle\rho_{\text{r}}(\mathbf{r})I(\mathbf{r})\right\rangle_{\mathbf{r}}. &(64)\end{aligned}$$

Due to the integration over the momentum space, the kinetic energy terms become equal and cancel out. The first term of equation 64 corresponds to the mean potential energy the illuminated ions have, whereas the second term corresponds to the mean potential energy of the entire ensemble. Thus, if the mean potential energy of the illuminated ions is smaller than the entire ensemble, the energy change is positive, which results in heating. Vice versa, by illuminating high energy ions the evaporation leads to a cooling of the ensemble.

Applied to a multipole trap of n'th order, the mean total energy is given by equation 54 $\left\langle\left\langle E_{\text{tot}}\right\rangle_{\mathbf{r}}\right\rangle_{\mathbf{v}} = (\frac{3}{2} + \frac{1}{2} + \frac{1}{n-1})k_{\text{B}}T$ and the mean potential energy is $\left\langle E_{\text{p}}\right\rangle_{\mathbf{r}}=(\frac{1}{2} + \frac{1}{n-1})k_{\text{B}}T$. Thus, the change in temperature and ion number is described by:

$$\begin{aligned}\left\langle\left\langle \dot{E}_{\text{tot}}\right\rangle_{\mathbf{r}}\right\rangle_{\mathbf{v}} &= \left(\frac{2n-1}{n-1}\right)k_{\text{B}}\dot{T} &(65)\\ &= -\sigma_{\text{pd}}\int \rho_{\text{r}}(x,y,z,T)\Phi(x,z,x_{\text{L}},z_{\text{L}})V(x,y,z)\,\text{d}x\text{d}y\text{d}z\\ &\quad + \left(\frac{n+1}{2n-2}\right)\sigma_{\text{pd}}k_{\text{B}}T\int \rho_{\text{r}}(x,y,z,T)\Phi(x,z,x_{\text{L}},z_{\text{L}})\,\text{d}x\text{d}y\text{d}z\end{aligned}$$

$$\dot{N} = -\sigma_{\text{pd}}N\int \rho_{\text{r}}(x,y,z,T)\Phi(x,z,x_{\text{L}},z_{\text{L}})\,\text{d}x\text{d}y\text{d}z \tag{66}$$

with $\rho_r(x,y,z,T) = \int \frac{\exp[-V(x,y,z)/k_B T]dy}{\int \exp[-V(x,y,z)/k_B T]dxdydz}$ → spatial column density,
$V(x,y,z)$ → ion trap potential,
$\Phi(x,z,x_L,z_L)$ → photon flux distribution,
x_L and z_L → detachment beam position.

3.1.2 ION-ION THERMALIZATION RATE

The main assumption of the thermodynamic model is that the ion-ion thermalization time is much smaller than the evaporation time. In the special case of a single particle plasma the ion-ion collision rate, already calculated by Spitzer in the 1950s [80], is equal to the thermalization rate [93]:

$$\nu_{ii} = \frac{n_i e^4 \log \Lambda_{ii}}{12\epsilon_0^2 \sqrt{\pi^3 m_i (k_B T)^3}}. \tag{67}$$

with the ion density n_i and $\log \Lambda_{ii}$ as the Coulomb logarithm, which is defined as the following:

$$\log \Lambda_{ii} = \log\left(\frac{r_{max}}{r_{min}}\right). \tag{68}$$

r_{max} and r_{min} are the upper and lower boundary of the impact parameter to approximate a Coulomb collision, which in reality has infinite range. The minimum distance is approximated by the deBroglie length or the classical distance of closest approach, which of both is larger:

$$r_{min} \approx \max\left(\frac{h}{\sqrt{2\pi m k_B T}}, \frac{e^2}{4\pi\epsilon_0 k_B T}\right) \tag{69}$$

The maximum impact parameter is typically chosen to be the Debye length:

$$r_{max} \approx \lambda_D = \sqrt{\frac{\epsilon_0 k_B T}{n_i e^2}}. \tag{70}$$

3.2 LASER-INDUCED EVAPORATION OF TRAPPED NEGATIVE IONS

To study the effect of laser-induce evaporation on the ions' energy distribution, six measurements were performed, in which the laser beam was positioned at different points relative to the spatial distribution of the ions along the axial axis. Overlapping with different spatial regions of the ion cloud, ions of different potential energies were addressed.

3.2.1 EXPERIMENTAL IMPLEMENTATION

Figure 27 shows schematically the procedure of the experimental cycle. The ions are created, loaded and initially thermalized with a helium buffer gas

pulse at a high ion trap offset, as explained in section 2.1. After the initialization the trap potential is ramped down, to create the optimized trapping and extraction potential. This ramping is done slowly, thus the ions' energy distribution is not affected. After the final potential is reached the evaporation process is started, by shining in the photodetachment laser light.

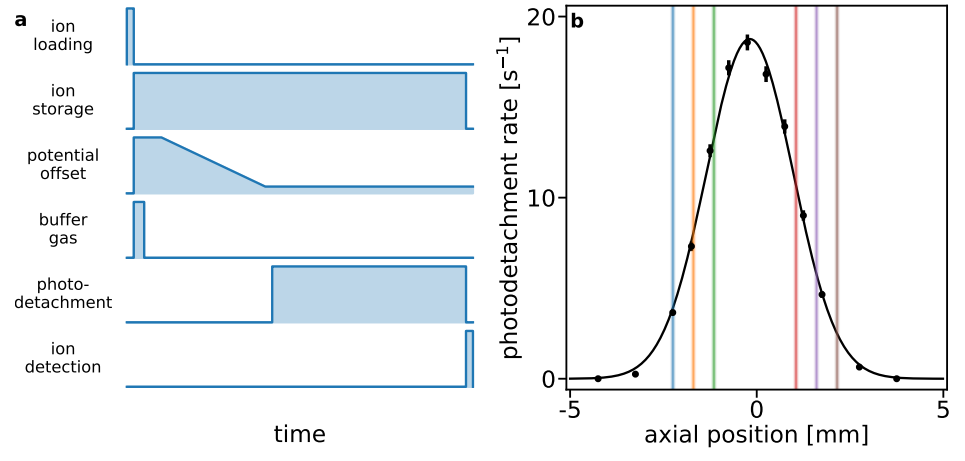

Figure 27: Procedure of static evaporation measurements. **a**, schematic representation of the experimental measurement cycle. The ion initialization, including the loading, the thermalization with the buffer gas pulse and the potential manipulation. Following is the beginning of the evaporation measurement, including position dependent photodetachment and ion detection. **b**, shown in black is the spatial distribution measured via a separate photodetachment tomography measurement. The colored bars illustrate the laser beam positions, corresponding to six measurements of the evaporation dynamics. The bars' width correspond to the laser beam width of 180 µm ($1/e^2$).

The ions have typically a initial temperature of 370 K and the axial distribution is nicely represented by a thermal distribution in a harmonic trap, as shown in Figure 27 **b**. Also shown are the photodetachment beam position and width in respect to the ion distribution for six evaporation measurements. The photodetachment light is provided by a laser diode with a maximum output power of 50 mW at a wavelength of $\lambda_{pd} = 660$ nm, which is far-below the photodetachment threshold of $\lambda_{th} = 678.37$ nm. The temporal evolution of ion temperature and ion number is measured by extracting the ions after different photodetachment interaction times and guiding them to the detector. The ions are counted and the temperature can be derived by their TOF distribution (see section 2.1.4).

The main assumption in the earlier discussed thermodynamic model (section 3.1.1) is that the ion-ion thermalization rate is much higher than the evaporation rate. To ensure the validity of this assumption the photodetachment light intensity was adapted to each laser beam position. The light-induced loss rate is calculated by equation 66, taking into account the beam width (180 µm at $1/e^2$) and the power. The ion-ion thermalization rate on the other hand was

calculated by equation 67. Table 1 summarizes the peak intensities and the calculated loss and thermalization rate for all laser beam positions.

beam position [mm]	peak intensity [$\frac{W}{cm^2}$]	initial evaporation rate [s^{-1}]	thermalization rate [s^{-1}]
-2.25	15.1	0.23	1.38
-1.70	11.0	0.37	1.32
-1.15	3.8	0.21	0.97
1.05	4.5	0.21	1.13
1.60	11.7	0.31	1.75
2.15	20.0	0.24	1.60

Table 1: Laser beam intensities corresponding to the static evaporative cooling and heating measurements shown in Figure 28.

3.2.2 ION ENERGY EVOLUTION VIA STATIC EVAPORATION

The measured evolution of temperature and ion number as a function of interaction time with the photodetachment laser light is shown in Figure 28. Each point in the upper panel corresponds to multiple hundreds of the above described measurement cycles until the derived width of the Gaussian shaped TOF converged. These TOF distributions typically consists of 10 000 measured ions. The error bars are derived from the error of the fitted Gaussian function to the TOF distribution. The lower panel shows the ion number normalized to the initial starting number of counted ions on the detector, typically 50 ions.
One can see that for the two measurements, in which the beam position is close to the ion cloud center, the ion ensemble is heated up. Whereas for the other measurements the temperature decreases by about a factor of 2. This corresponds to the picture derived from section 3.1.1 that a removal of ions with an energy lower than the mean potential energy leads to heating. This is the case in the trap center. For the beam positions further from the center the removed ions' energy was larger than the mean potential energy and therefore leading to a cooling effect.
The full theoretical evolution of temperature and ion number derived in section 3.1.1 is shown in solid lines. For an octupole ion trap ($n = 4$) equation 66 and 65 results in the following equations of evolution:

$$\begin{aligned}\dot{T} = &-\left(\frac{3}{7}\right)\frac{\sigma_{pd}}{k_B}\int \rho_r(x,y,z,T)\Phi(x,z,x_L,z_L)V(x,y,z)\mathrm{d}x\mathrm{d}y\mathrm{d}z \\ &+\sigma_{pd}\left(\frac{3}{7}\right)\left(\frac{5}{6}\right)T\int \rho_r(x,y,z,T)\Phi(x,z,x_L,z_L)\mathrm{d}x\mathrm{d}y\mathrm{d}z\end{aligned} \tag{71}$$

$$\dot{N} = -\sigma_{pd}N\int \rho_r(x,y,z,T)\Phi(x,z,x_L,z_L)\mathrm{d}x\mathrm{d}y\mathrm{d}z - \nu_{bgr}N. \tag{72}$$

The ion trap potential is determined by combining the spatial distribution, measured via photodetachment tomography in axial and radial direction

(section 2.1.3.1), and the corresponding temperature, measured via TOF thermometry (section 2.1.4). The potential is in well-approximated by a harmonic potential in axial direction and a r^6-potential in radial direction:

$$V_{OH^-}(x,y,z) = 1.94(11) \cdot 10^{-15}\,\mathrm{J/m^2} \cdot z^2 + \\ + 4.1(2) \cdot 10^{-3}\,\mathrm{J/m^6} \cdot (x^2+y^2)^3. \tag{73}$$

The normalized ion density $\rho_r(x,y,z,T)$ is then given by the thermal spatial distribution in this potential for a given temperature and the photon flux is modeled by a two-dimensional Gaussian shaped distribution at the laser beam position (x_L, z_L), with a total photon flux of $F_L = \frac{P}{h\nu}$. P is the measured power and $h\nu$ the photon energy. The absolute photodetachment cross section of OH^- at 662 nm, $\sigma_{pd} = 8.5(1)(3)\ \mathrm{cm^2}$, was measured in earlier work [94].
With the initial temperature measured, all necessary parameters of equation 71 and 72 are determined and one can calculate the evolution of temperature and ion number by numerically integrating those differential equations. The solutions for all six different laser beam positions are shown as solid lines in Figure 28. The shaded areas correspond to the uncertainty in the ion trap potential.

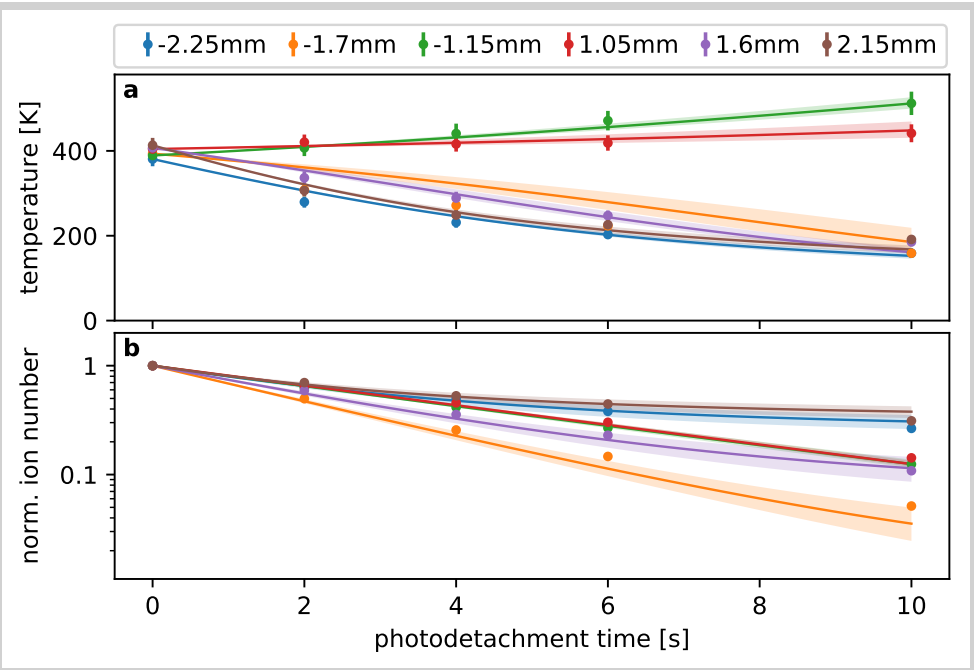

Figure 28: Static evaporation measurements. **a**, the temporal evolution of ion temperature and **b**, the normalized ion number for six different laser beam positions. The color code corresponds to the positions in Figure 27. The solid points represent the measured data and the lines show the numerical integration of equation 71 and 72 for the measured initial conditions. The shaded areas illustrate the uncertainty of the predetermined trapping potential (equation 73).

The measurements with a constant laser beam position show that the evaporation process is well-represented by the introduced thermodynamic model.

The cooling process, however, is limited by the illuminated potential region and therefore by the laser beam position. Due to the cooling of the ions, their energy is no longer sufficient to reach the illuminated potential and the cooling stops.

3.3 FORCED EVAPORATIVE COOLING OF TRAPPED NEGATIVE IONS

The limitation of the static evaporative cooling can be circumvented by moving the photodetachment beam, during the cooling process, towards the trap center. This way, the cut-off energy is dynamically reduced and the ion ensemble is forced to lower energies. This process is called forced evaporative cooling.

3.3.1 REALIZATION OF DYNAMICAL ANION PHOTODETACHMENT

Figure 29 shows schematically the measurement cycle to investigate the forced evaporative cooling process. The shown sequence is similar to the earlier measurements in section 3.2, however, this time with switching on the photodetachment light, the laser beam is moved simultaneously towards the trap center by an automated linear stage.

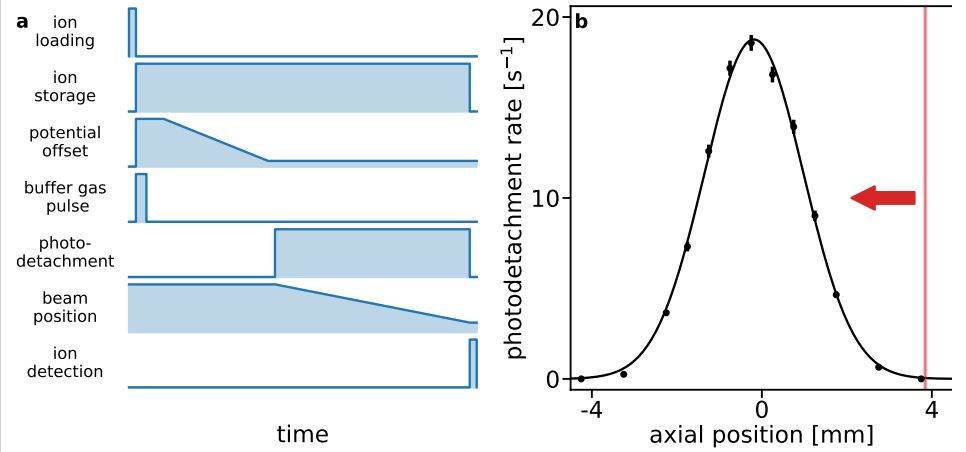

Figure 29: Procedure of forced evaporative cooling measurements. **a**, schematic representation of the experimental measurement cycle, similar to the static evaporation measurements. In this case, with switching on the photodetachment light, the beam moves towards the trap center. **b**, axial ion distribution measured via photodetachment tomography, shown in black. The red bar illustrates the starting position of the forced evaporative cooling measurements.

As illustrated in Figure 29 **b** the initial beam position is at $z(0) = 4\,\mathrm{mm}$ in respect to the center of the axial ion distribution. Because the overlap between ions and photons is small, the laser beam peak intensity is increased to $325\,\mathrm{W/cm^2}$ (beam diameter 180 µm and power 41 mW). The cooling process is measured for four different constant laser beam velocities. To map out the cooling dynamics, the ions are extracted after the photodetachment beam has

moved to a certain final position. Note, that for different beam velocities this corresponds to different photodetachment interaction times.

3.3.2 COOLING MOLECULAR ANIONS IN THE KELVIN REGIME

Figure 30 shows the result of this measurement for four different laser beam velocities. In each case the ions were extracted, without photodetachment and after the beam traveled 1 mm, 2 mm, 3 mm and 3.4 mm. For the two faster beam velocities additional measurement were taken for 3.5 mm, 3.6 mm and 3.7 mm.

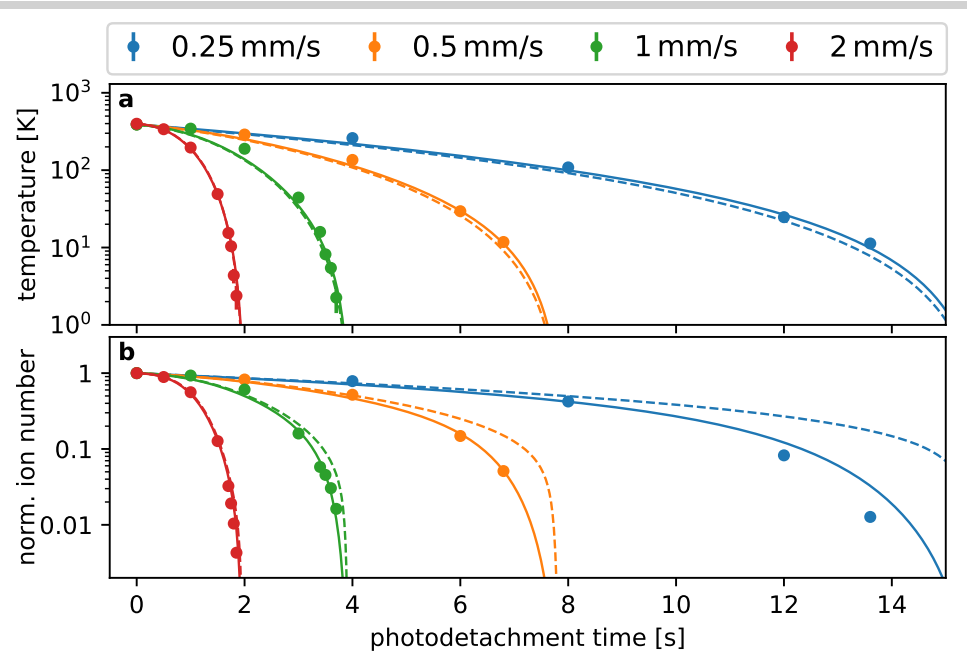

Figure 30: Forced evaporative cooling via far-threshold photodetachment light. The evolution of **a**, the ions' temperature and **b**, the normalized ion number, while moving the photodetachment beam towards the trap center, for four different laser beam velocities. The initial beam position is at 4 mm and the ions were extracted after reaching 4 mm, 3 mm, 2 mm, 1 mm and 0.6 mm. For 1 mm/s and 2 mm/s additional extraction positions were measured, 0.5 mm, 0.4 mm and 0.3 mm. Those measurements as represented as solid points. The dashed lines show the numerical integration of equation 71 and 72 for the measured initial conditions. The solid lines correspond to the thermodynamic model including the ion-ion rf heating (see equation 75).

The initially loaded ≈ 1100 molecular anions at a temperature $T = 370(12)$ K could by cooled below 4 K in less than 2 seconds. The highest cooling efficiency, however, was measured for a beam velocity of 1 mm/s. After 3.7 s an ensemble temperature of 2.2(8) K with 1.62(7) % of the initially loaded ions was measured. This corresponds to an increase of phase-space density by three orders of magnitude (see Figure 32) and the temperature is already far

below 10K, which is the lowest translational temperature for anions, typically achieved in cryostat multipole rf traps [19].
The differential equations 71 and 72, describing the ensemble dynamics for a fixed beam position, can be transferred to the forced evaporation by introducing a time-dependent laser beam position along the axial axis $\Phi\big(x, z, 0, (4mm - v_{\text{stage}}t)\big)$. The dashed lines in Figure 30 correspond to the numerical solutions of the derived differential equations. However, the temperature evolution is modeled quite accurately, the ion loss is underestimated in all four measurements, which suggests that an additional loss mechanism has to be taken into account.
This can be explained by ion-ion collisional rf heating. As introduced in section 2.1.1 the radial confining potential is generated by the fast oscillating motion in the inhomogeneous field of a multipole trap. In the adiabatic approximation, the ions motion can be separated into a secular motion inside a ponderomotive potential. However, a collision in this potential can transfer energy from the driving field into the secular motion. The effect of atom-ion collisional rf heating has been discussed in section 2.1.2.4 about the initial helium buffer gas pulse, and it is plays a major role in the following chapter about sympathetic cooling by a heavy ultracold buffer gas, section 4.1.
In this section, although there are no atoms to collide with, but ion-ion collisions can also perturb the trajectory of an ion in the trap and therefore lead to heating. Traditionally, this heating rate is approximated by a mean energy transfer per ion-ion collision [95, 96]:

$$Q_{\text{ii}} = \nu_{\text{ii}} \bar{\epsilon} \langle V_{\text{eff}} \rangle, \tag{74}$$

where ν_{ii} is the ion-ion collision rate (see equation 67) and $\bar{\epsilon}$ is the mean relative energy exchange per collision. The temperature change, due to ion-ion collisions, in this system can be therefore described by the following differential equation:

$$\dot{T} = \left(\frac{3}{7}\right)\left(\frac{1}{3}\right) T \bar{\epsilon} \nu_{\text{ii}}(T). \tag{75}$$

The unknown parameter $\bar{\epsilon}$ was determined separately by a heating measurement, shown in Figure 31. The ions were initialized by a helium buffer gas pulse, the potentials ramped down and afterwards, the ions were kept in the octupole trap for various storage times. The solid line represents a numerical solution of equation 75 fitted to the data point, with $\bar{\epsilon}$ and the initial temperature as free parameters. The derived mean relative energy exchange per ion-ion collision is $\bar{\epsilon} = 0.045(6)$.

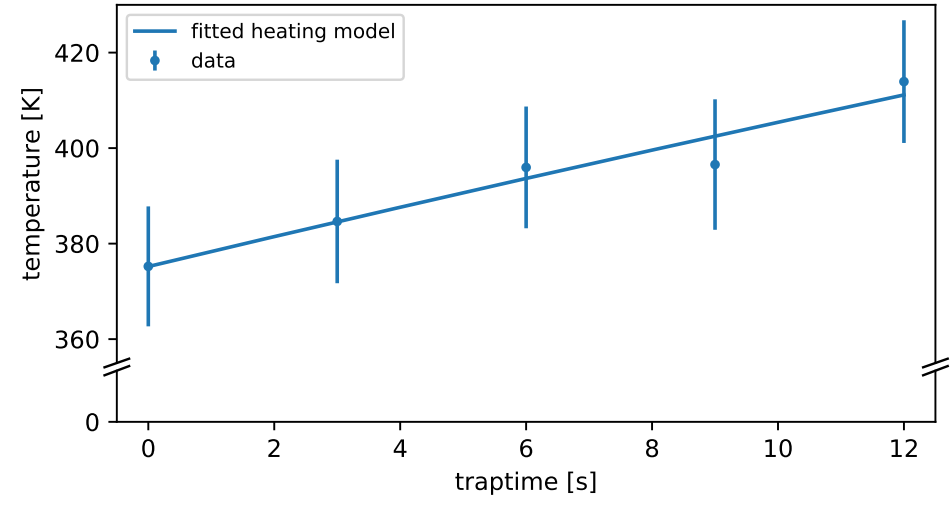

Figure 31: Ion-ion rf heating. Shown as solid points is the temperature evolution of the ion ensemble after the initialization process. The solid curve represents the fitted numerical solution of equation 75 with $\bar{\epsilon}$ and the initial temperature as free parameters. The curve corresponds to a mean relative energy exchange per ion-ion collision of $\bar{\epsilon} = 0.045(6)$.

Including the ion-ion rf heating in equation 71, results in the numerical solutions shown as solid lines in Figure 30. Introducing the ion-ion heating term, explains the observed additional ion loss and completes the thermodynamic model, describing photodetachment cooling of anions in any multipole trap. Note that relative to the cooling term, both heating terms become smaller with increasing pole order.

The range of validity and the cooling efficiency can be described by two dimensionless parameter, the Coulomb coupling constant Γ and the relative phase-space density. The first one represents the nearest-neighbor Coulomb energy to the thermal energy:

$$\Gamma = \frac{E_c}{E_{th}} = \frac{e^2}{4\pi\langle r\rangle_{WS} k_B T}, \tag{76}$$

with $\langle r\rangle_{WS}$ being the Wigner-Seitz radius, which is the mean inter-particle distance. In a weakly coupled plasma, $\Gamma \ll 1$, the thermal energy is much larger and the Coulomb interaction can be treated as a two-particle ion-ion collision, as discussed above. For a Coulomb coupling parameter close to unity the Coulomb potential generated by neighboring ions can not be ignored anymore and the developed thermodynamic model breaks down. For $\Gamma > 2$ the ion cloud reveals phenomena as liquid-like behavior and for $\Gamma = 178$ one can observe a liquid-solid phase transition into a Coulomb crystal [97, 98].

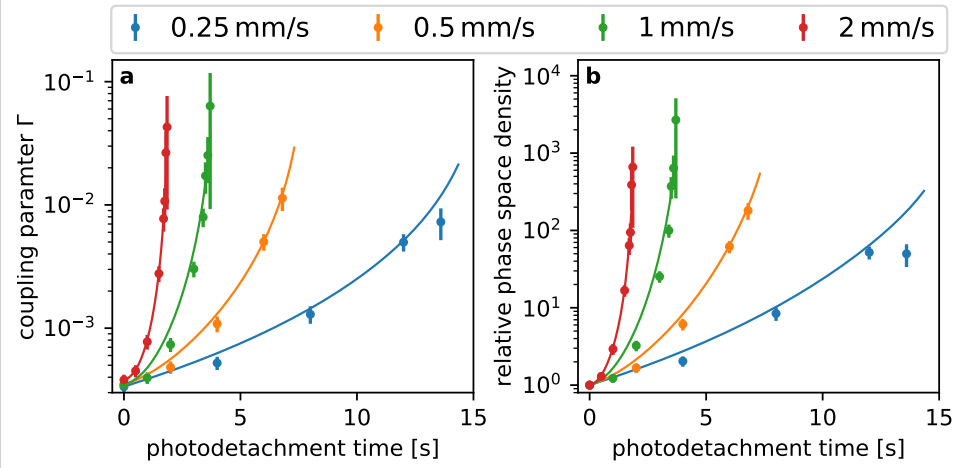

Figure 32: Dimensionless parameters to benchmark the cooling efficiency. **a**, Coulomb coupling parameter and **b**, relative phase-space density corresponding to the measurements (solid points) and the model solutions (solid curves) shown in Figure 30.

Figure 32 **a** shows the Coulomb coupling parameter corresponding to the measurements shown in Figure 30 and as solid lines the model including the heating rate. The largest increase was measured for the beam velocity $v_{\text{stage}} = 1$ mm/s. The ensemble of molecular anions was initialized at $\Gamma = 0.00035(4)$ and it was increase by forced evaporative cooling to $\Gamma = 0.06(5)$. This value is already quite close to the point, when the nearest-neighbor Coulomb potential becomes relevant. Figure 32 **b** shows the relative phase-space density. As the phase-space density represents the number of ions in a volume in space and momentum ($D = N\rho\lambda^3$), it is a good measure for the efficiency of the cooling process. The efficiency and pace of cooling is limited by three timescales, the thermalization rate, the evaporation rate and the heating rate:

- The *thermalization rate* describes how fast the energy is distributed over the whole ensemble. If the evaporation rate exceeds the thermalization time, the ions are spilled out of the trap, without an increase in phase-space density.
- The *evaporation rate* describes the light-induced loss rate. If the laser beam moves in faster than the high energy ions are removed, the relative cut-off energy drops and consequently the cooling rate.
- The *heating rate*, due to ion-ion interaction, is limiting the cooling process, due to a reduced cooling efficiency and therefore to a higher ion loss to cool the ensemble.

Most efficient cooling was observed for $v_{\text{stage}} = 1$ mm/s and decreasing efficiency for slower beam velocities, which can be explained by the introduced heating rate. In the solutions without the heating, the slowest beam velocity was most efficient. The fastest beam velocity, $v_{\text{stage}} = 2$ mm/s, was limited by the finite beam intensity, available at the experiment, and therefore limited

by the evaporation rate. This limitation, however, could be circumvented by increasing the photodetachment laser power.
If one recalls the ion-ion thermalization rate, equation 67, one sees that it depends on the product of the phase-space density and the Coulomb logarithm. In the example of the $v_{\text{stage}} = 1$ mm/s- measurement the Coulomb parameter dropped by a factor of 3, where as the phase-space density increase by multiple orders of magnitude. Thus, the thermalization rate increases with the cooling, which would allow us to increase beam velocity, if the evaporation rate is high enough.

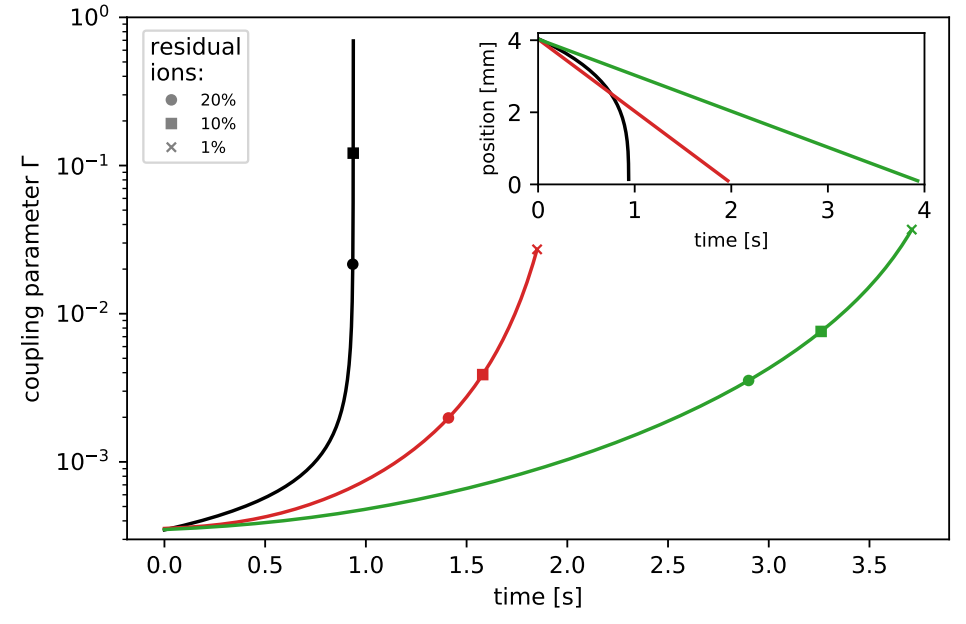

Figure 33: Modeled evolution of the Coulomb coupling parameter to illustrate runaway cooling. The red and the green curves correspond to the modeled dynamics for 1 mm/s and 2 mm/s, respectively (see Figure 32). The black line is the solution of an exemplary accelerated cooling scheme, explained in the text. The inset shows the beam position as a function of photodetachment time. The markers represent the residual fraction of initially loaded ions.

Here, an exemplary case is discussed. Starting with the same initial ion ensemble as in the measurements. The relative cut-off energy is kept constant. Simultaneously the laser beam intensity is adapted such, that the evaporation rate is always 10% of the thermalization rate. This way the models assumption are not violated, and a high cooling efficiency is reached. Figure 33 shows in green ($v_{\text{stage}} = 1$ mm/s) and red ($v_{\text{stage}} = 2$ mm/s) the Coulomb coupling parameter for constant beam velocity until only 1% of the ions are left. These curves are similar to the ones, representing the measured data in Figure 32. The inset illustrates the laser beam position as a function of photodetachment time.
Now in this exemplary case the cooling rate is adapted to the thermalization

rate, which results in an acceleration of both. Starting with the same initial conditions as in the measurements above, the self-accelerating regime is reached in less than 1 second. This behavior is called runaway cooling and is known from forced evaporative cooling of ultracold atomic gases [99].
The measurements presented in this chapter have shown, that forced evaporative cooling via photodetachment is a powerful tool to reduce the translational temperature of, in principle any anionic specie in a multipole trap by several orders of magnitude in a short time. The prospect of reaching the runaway regime promises even higher cooling efficiencies and opens up a new regime, to cool anions into the cold regime. The ion-ion rf heating has been identified as an additional heating term in the thermodynamic model, which well-represents the measured data. With increasing rf trap pole order, both heating terms become smaller with respect to the cooling one, which allows more efficient evaporative cooling. Since the final anion temperature only depends on the final laser beam position, forced evaporative cooling via photodetachment provides the possibility to prepare anion samples over a vast temperature range. It is therefore ideal for collision energy-dependent reaction measurements, as performed up to now in merged beam [18], crossed beam [17] and cryogenic multipole trap [20] experiments. Furthermore, in the prospect of anion laser-cooling, a pre-cooled anion ensemble in ultra-high vacuum is needed [32, 57]. The technique of forced evaporative cooling via photodetachment shown here does not involve the typically used cryogenic buffer gas for anion cooling and thus, is an ideal tool to efficiently prepare a pre-cooled anionic sample in ultrahigh vacuum conditions.

4 SYMPATHETIC COOLING VIA AN ULTRACOLD BUFFER GAS

Sympathetic cooling describes the technique, in which two trapped species are overlapped, one of them is directly cooled via an established cooling technique, the other one is then cooled "sympathetically" via elastic collisions with the colder specie. For cations, it was experimentally demonstrated for $^{198}Hg^+$ co-trapped with laser-cooled $^9Be^+$ ions [100] and also shown for neutral particles in a mixture of two ^{87}Rb spin states, where one of the two states is evaporatively cooled [101]. A hybrid atom-ion system like in Heidelberg, which combines molecular anions and laser-cooled atoms, this technique allows to not only sympathetically cool the translational degree of freedom, but it also provides the ability to quench vibrational and rotational motion, which was successfully demonstrated for atom-cation systems, as $BaCl^+$ [102]. For anions, the state of the art is cooling with a cryogenic buffer gas. However, the key limitation to the final ion temperature attained is the temperature of the buffer gas. Thus, choosing a buffer gas with a lower temperature, for example, laser-cooled buffer gas would sympathetically cool the anions to much lower temperatures. First experiments for anions co-trapped with laser-cooled atoms were done in an earlier version of the HAITrap setup used in this work [47].
The cooling principle of an ultracold atom cloud overlapped with the ion of choice appears to be simple, but it is surprising that the ions do not thermalize to the buffer gas temperature, which was already discussed in 1968 by Major and Dehmelt [59]. The thermalization process of an ion in the ponderomotive potential of an rf trap differs from a particle in a conservative potential. The time-averaged confinement in the rf trap is created by a time-dependent force, which can lead to heating in case of a collision, even with a neutral particle in rest.
The ions' motion inside a rf trap has been discussed in chapter 2. In the following section 4.1, the influence of a neutral-ion collision on this motion is further described. The heating collisions yield a non-thermal steady-state energy distribution, which distinguishes itself by a high-energy power-law tail, numerically predicted by DeVoe [103] and also analytically calculated for an ion in a Paul trap and a homogeneous buffer gas distribution [50, 51]. In previous work in the HAITrap group in Heidelberg, the theoretical calculations were further developed, including multipole ion traps and inhomogeneous buffer gas clouds [49, 48]. A brief discussion of these numerical calculations and the derived steady-state energy distribution for our system are given in section 4.1.1. In the course of this work, the model was further developed to derive the dynamical cooling behavior into the non-thermal steady-state energy distribution. Section 4.1.2 details the changes to the previously established theoretical model and shows the temporal evolution of the energy distribution

into the steady-state. However, this model does not include ion loss channels, which are energetically accessible for the two systems, Rb-O^- and Rb-OH^-. Section 4.2 discusses the observed loss channels for the co-trapped Rb-OH^- and Rb-O^- systems, which can be attributed to reactive and photodetachment processes. For both systems the reaction rate coefficients are determined, which allow us to completely describe the evolution of ion temperature and ion number for sympathetic cooling of O^- and OH^- by ultracold rubidium in a quasi-static approximation.
Section 4.3 shows sympathetic cooling measurements depending on the relative overlap between the coolant and the anions. The results are well-described by a thermodynamic model, including the ion-ion heating rate introduced in chapter 3.

4.1 ELASTIC ATOM-ION COLLISIONS INSIDE A RF TRAP

An elastic collision is best described in the center of mass frame (COM). The velocities of both collision partners are given by their relative velocity and the velocity of the COM:

$$\mathbf{v}_{\mathrm{COM}} = \frac{m_\mathrm{i}\mathbf{v}_\mathrm{i} + m_\mathrm{a}\mathbf{v}_\mathrm{a}}{m_\mathrm{i} + m_\mathrm{a}}, \tag{77}$$

where m_a and $\mathbf{v}_\mathrm{a}$ are the mass and the velocity of the atom, respectively. m_i and $\mathbf{v}_\mathrm{i}$ are on the other hand the mass and velocity of the ion, respectively, which can be expressed by the COM and the relative velocity.

$$\mathbf{v}_\mathrm{i} = \mathbf{v}_{\mathrm{COM}} + \frac{m_\mathrm{a}}{m_\mathrm{a} + m_\mathrm{i}} \left(\mathbf{v}_\mathrm{i} - \mathbf{v}_\mathrm{a}\right). \tag{78}$$

If an elastic collision occurs, the center of mass velocity remains unchanged, whereas the relative velocity vector is rotated:

$$\mathbf{v}'_\mathrm{i} = \mathbf{v}_{\mathrm{COM}} + \frac{m_\mathrm{a}}{m_\mathrm{a} + m_\mathrm{i}} \mathcal{R}(\Phi, \Theta) \left(\mathbf{v}_\mathrm{i} - \mathbf{v}_\mathrm{a}\right), \tag{79}$$

where $\mathcal{R}(\Phi, \Theta)$ is a rotation matrix, including the polar Φ and the azimuthal angle Θ. However, in a rf trap the ion motion consists of the macro- and the micromotion, which are separable, due to their different time scales, see section 2.1.1: $\mathbf{v}_\mathrm{i} = \mathbf{v}_\mathrm{i,d} + \mathbf{v}_\mathrm{i,rf}$.
Since the time-averaged drift motion, $\mathbf{v}_\mathrm{i,d}$, represents the ion's translational velocity in a ponderomotive potential, to understand the cooling dynamics it is imperative to determine the change of this velocity via a collision. In this picture, the system is transferred into a frame, where the micromotion is attributed to the atoms. Here, the ions move with $\mathbf{v}_\mathrm{i,d}$ in an effective potential, $V_\mathrm{eff}(r)$ and the atoms have an effective velocity, $\mathbf{v}_\mathrm{a,eff} = \mathbf{v}_\mathrm{a} - \mathbf{v}_\mathrm{i,rf}$, taking the micromotion into account. Assuming that in the short period of time of a collision, the rf motion remains unchanged ($\mathbf{v}_\mathrm{i,rf} = \mathbf{v}'_\mathrm{i,rf}$), the ion's final drift velocity after the collision can be expressed in a similar way as equation 79 in the COM frame:

$$\mathbf{v}'_\mathrm{i,d} = \frac{m_\mathrm{i}\mathbf{v}_\mathrm{i,d} + m_\mathrm{a}\mathbf{v}_\mathrm{a,eff}}{m_\mathrm{i} + m\mathrm{a}} + \frac{m_\mathrm{a}}{m_\mathrm{a} + m_\mathrm{i}} \mathcal{R}(\Phi, \Theta) \left(\mathbf{v}_\mathrm{i,d} - \mathbf{v}_\mathrm{a,eff}\right). \tag{80}$$

In this effective atom velocity frame, one can attribute an effective mean energy to the atoms:

$$\langle E_{\mathrm{a,eff}} \rangle = \frac{1}{2} m_{\mathrm{a}} \langle \mathbf{v}_{\mathrm{a,eff}}^2 \rangle = \frac{1}{2} m_{\mathrm{a}} \left(\langle \mathbf{v}_{\mathrm{a}}^2 \rangle + 2 \langle \mathbf{v}_{\mathrm{a}} \mathbf{v}_{\mathrm{i,rf}} \rangle + \langle \mathbf{v}_{\mathrm{i,rf}}^2 \rangle \right). \tag{81}$$

Since the atom velocity and the rf motion are not correlated, the middle term is zero. For a thermal atom cloud, the first term can be expressed by the thermal energy. The mean energy stored in the rf motion is given by the effective potential (see equation 13):

$$\langle E_{\mathrm{a,eff}}(r) \rangle = \frac{3}{2} k_{\mathrm{B}} T_{\mathrm{a}} + \xi V_{\mathrm{eff}}(r), \tag{82}$$

where ξ is the atom-to-ion mass ratio.
Figure 34 illustrates the effect of the driving rf field on an atom-ion collision in a radio frequency trap. The upper panel **a**, shows the ion trajectory zoomed in at the radial turning point, at which the micromotion is the largest. The polarity of the electric quadrupole field is represented by gray/white background and the resulting direction of the force is illustrated by red arrows. The exemplary ion trajectory is shown in blue. The dashed line represents the time-averaged drift motion. Without a collision, the ion is following the unperturbed trajectory, shown in gray. The event of a head-on collision, when the electric field polarity changes, is shown at the black dashed line. The ion gains a lot of energy, although, in this example the neutral collision partner with the same mass is in rest. The collision results in a completely stopped ion, which afterwards, is accelerated outwards by a full period of the electric field. The resulting macromotion amplitude is increased and hence the ion's translational energy as well. This heating effect is also known, as buffer gas rf-heating.

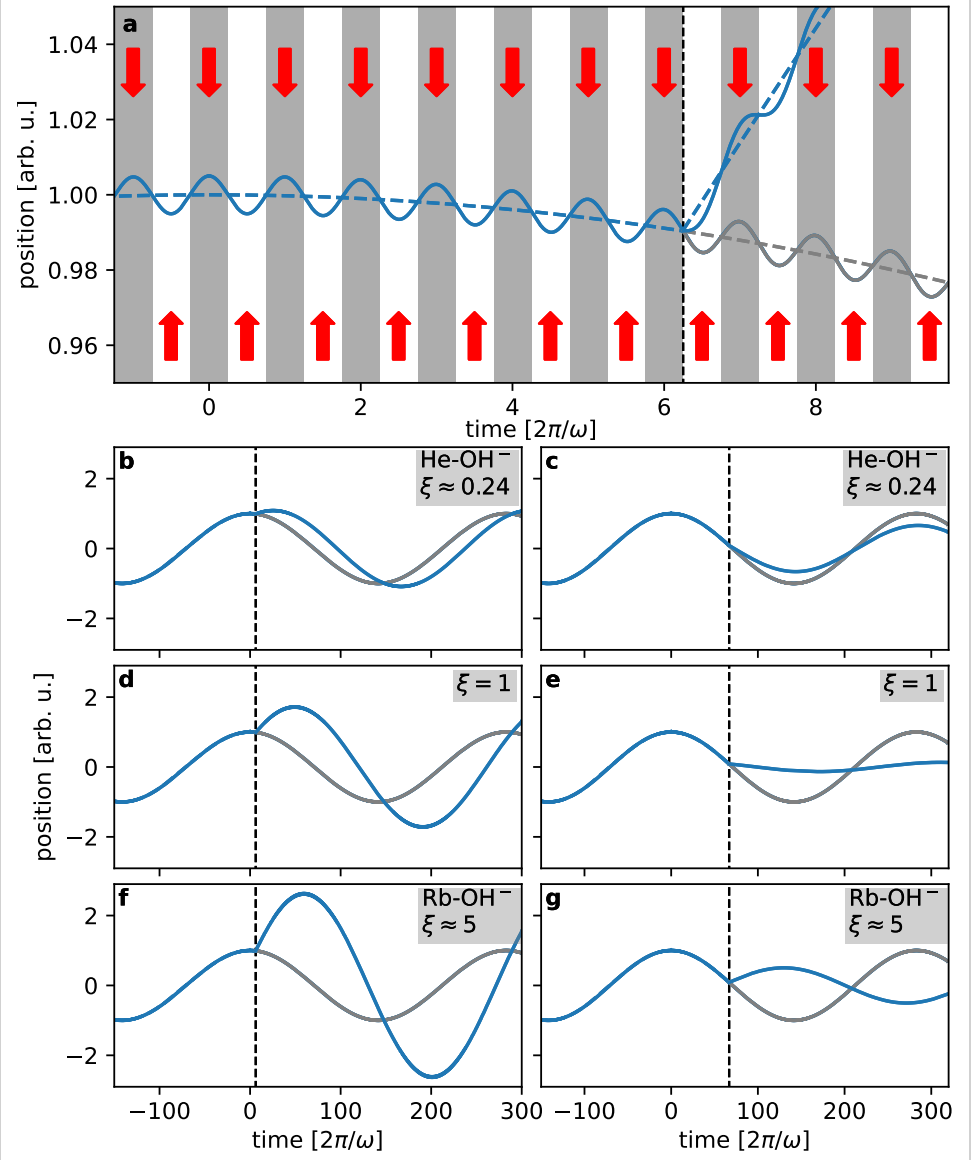

Figure 34: Elastic head-on collisions in a rf trap. **a**, the blue line represents an ion trajectory close to the turning point of the macromotion. At point $t = 12.5\pi/\omega$ s, the ion is colliding head-on with a neutral of the same mass at rest, leading to an increase in the macromotion amplitude (dashed blue line). The gray trajectory represents the unperturbed ion motion. The gray/white background color illustrates the polarity of the electric field, inducing a force in the direction of the red arrows. The lower panels **b**, **d**, and **f**, show the zoomed out trajectory, colliding at the same point in time (black dashed line) with **b**, a helium atom in rest, **d**, a neutral of the same mass, similar to the upper panel and **f**, with a rubidium atom in rest. **c**, **e**, and **g**, show for the same mass ratios, an exemplary cooling collision close to the trap center.

The lower left panels, **b**, **d** and **f**, in Figure 34 illustrate the dependency on the mass ratio of the colliding atom and ion, derived in equation 80. For a lighter collision partner, the ion is slowed down, but not stopped, which results in

a smaller heating effect. However, while colliding with a collision partner of higher mass, the ion experiences a recoil and the heating effect is increased. Whereas **d** shows the before-mentioned example of equal masses, **b** illustrates the reduced heating effect of OH^- colliding with a helium atom in rest and **f** shows the increased heating for rubidium as a collision partner. The lower right panels, **c**, **e** and **g**, show for the same mass ratios the final ion trajectory after a collision closer to the trap center. For equal masses, the momentum exchange is the most efficient, whereas the heating effect for collisions at larger radii is smaller for lower coolant masses. Already Major and Dehmelt estimated a critical atom to ion mass ratio of $\xi \approx 1$ above which the rf collision lead to a net heating and loss from the trap [59]. In previous work of the Heidelberg group the critical mass ratio was generalized for multipole rf ion traps [49]:

$$\xi_{\mathrm{crit}}(n) \approx 1.5(n-1), \tag{83}$$

where n is the ion trap pole order.
Since the cooling dynamics are not trivial, a numerical model to derive the final steady state energy distribution of an ion in an atom cloud has been developed within this group in earlier works [104, 84]. In the following section, the numerical model is discussed and the steady state energy distribution of our system is shown. In course of this work, the model has been further developed to simulate the temporal evolution into the steady state and therefore derive the amount of collision required to reach this energy distribution.

4.1.1 STEADY STATE DISTRIBUTIONS

The following model to derive the ion's final steady state energy distribution is based on these assumptions:

- A single ion is stored in an infinitely long rf trap of the n'th order. Thus, Coulomb interaction between multiple ions is neglected. Furthermore the influence of axial confinement is not taken into account.
- The timescales of macro- and micromotion are separable, as before mentioned in the adiabatic approximation (see section 2.1.1).
- The collision scattering rate is velocity-independent and can be described by the classical Langevin capture model.
- The time between consecutive collisions is large, compared to the timescale of the macromotion.

In contrast to a full trajectory simulation, the probability of a collision at a radius r is calculated as following:

$$p_{\mathrm{coll}}(r)dr = \rho_{\mathrm{a}}(r)p_{\mathrm{i}}(r, E_{\mathrm{i}}, L, n)dr, \tag{84}$$

where $\rho_{\mathrm{a}}(r)$ is the atom density distribution and $p_{\mathrm{i}}(r, E_{\mathrm{i}}, L, n)$ the probability to find a single ion at the radius r for a given ion energy E_{i} and angular

momentum L in the radial plane. n is the trap order.

In the calculation of the steady state energy distribution, the final ion velocity in radial and axial direction after the collision is calculated via equation 80 and saved. The atom velocity is randomly derived from a three-dimensional thermal distribution with an atom cloud temperature of $T_a = 200\,\mu K$. The relative velocity is then calculated by the kinetic energy of the ion at the collision radius and the sampled atom velocity vector. The micromotion phase is chosen randomly between $0 \leq \phi_{rf} \leq 2\pi$ and therefore determines the micromotion velocity at the time of the collision. Finally the scattering angles can be chosen randomly between $0 \leq \Phi \leq 2\pi$ and $0 \leq \Theta \leq \pi$, weighted with the isotropically distributed angular probability, predicted in the Langevin picture of a classical elastic atom-ion collision. With these sampled collision parameter a new set of ion properties are generated, which represent the new starting conditions for the next collision calculation. To derive the steady state energy distribution upto 10^6 of these collisions are computed and saved. The energies derived after all the collision are then binned, resulting in an energy distribution. The first 5000 collisions are not taken into account, to remove any thermalization effect into the steady state. Since not every collision has the same probability to happen in the given time, the final energies are weighted by the likelihood of the collision, which is given by time between two consecutive collisions:

$$\tau = 1/\left(k_{el} \int \rho_a(r)\, p_i(r, E_i, L, n)\, dr\right), \tag{85}$$

where k_{el} is the elastic collision rate coefficient, derived from the Langevin model [89].
Note, that the velocity-independent collision rate coefficient is a simplification, since in a more complete description the atom-ion collision is treated by expanding the wave-function into partial waves, which contribute to the total elastic collision cross section. For many partial waves, the elastic cross section scales with the collision energy like $\sigma \propto E^{-1/3}$ [90], which results in an energy dependent collision rate. In previous calculations the partial wave approximation and the simpler Langevin model have been compared. It was shown that for both the final energy distribution and the relaxation rate the elastic collision cross section derived from the Langevin model is valid [105, 50].

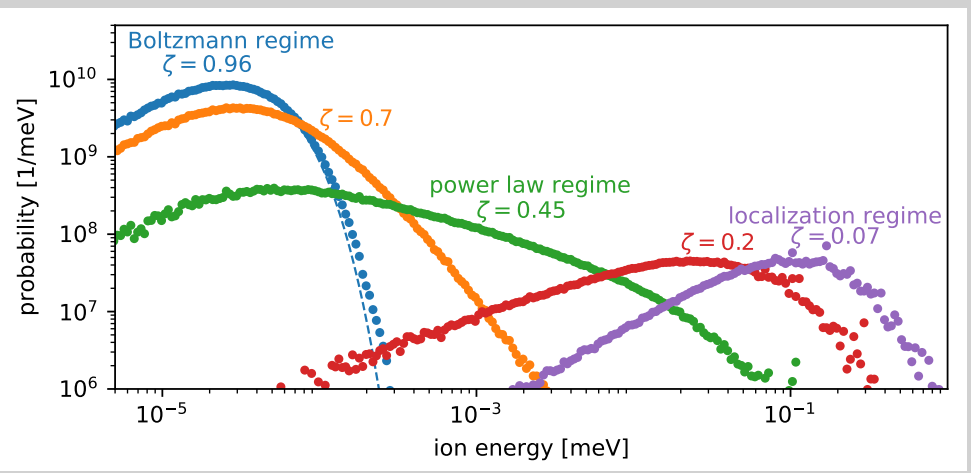

Figure 35: Final steady state energy distributions for different atom-ion mass ratios and ion trap pole orders, expressed in the thermalicity parameter ζ, equation 86. The calculated energy distributions can be separated into three regimes, depending on the thermalicity parameter. The dashed line represents the energy distribution of a thermal ion cloud at the atoms' temperature, $T_a = 200$ µK. Adapted from [49].

Figure 35 shows the final energy distributions for different mass ratio and ion trap configurations. The atom distribution is chosen to be homogeneous with a temperature of $T = 200$ µK.
A parameter combining the two collision properties, the mass ratio ξ and pole order n, is the "thermalicity" parameter:

$$\zeta = \frac{3n-1}{3n-1+2\xi}. \tag{86}$$

It is defined as the ratio between the thermal energy of the atoms and the effective atom energy, given by equation 82.
Based on the thermalicity, the shown energy distributions can be separated in three regimes:

Boltzmann regime: For high pole orders and low atom to ion mass ratios, the thermalicity is $\zeta \approx 1$ and the influence of the micromotion is largely suppressed. Thus, in limit $\zeta \to 1$ the energy distribution converges towards a thermal distribution in a conservative potential.

Power law regime: In the intermediate regime, the micromotion becomes relevant compared to the atom's thermal energy. While the thermal energy remains constant with increasing ion energy, the effective potential is proportional to it. Thus, the probability to gain energy from the micromotion remains constant and therefore multiple consecutive heating collisions can lead to an exponential increase in the ion's energy. This behavior is known to cause power law distributions.

Localization regime: With decreasing the thermalicity, the collisions lead to a net heating and therefore to an ion loss out of the trapping potential. Localization of the atoms to a volume in the trap center limits the maximum effective atom energy. Thus, in the region of high energy gain, there are no atoms anymore.

In the HAITrap experimental setup, the coolant rubidium is about five times heavier than O^- and OH^-. In a Paul trap this would result in a thermalicity parameter of $\zeta \approx 0.33$, which is far in the power law regime. Combined atom-ion trapping is only possible with a localized buffer gas cloud. For an octupole trap, however, the thermalicity is sufficiently high, $\zeta \approx 0.53$.
Figure 36 shows the final energy distribution for the HAITrap experimental setup, including the rf voltage and frequency used. The black line, represents the Boltzmann energy distribution in a conservative trap, whereas blue and orange sold lines include the driving micromotion for a homogeneous and a localized buffer gas cloud, respectively. The width chosen for a localized Gaussian shaped atom cloud is the typical cloud size in the experiment. One can see, although, a heavy sided energy distribution is expected, the mean energy, represented as dashed lines, of $\langle E_\mathrm{i} \rangle = 3.23 \cdot 10^{-5}$ meV is only about 2 times larger than the Boltzmann distributed one, $\langle E_\mathrm{i} \rangle = 1.44 \cdot 10^{-5}$ meV. The localization of the atom cloud leads to a small drop of the probability at larger energies, which is negligible in the cooling process.

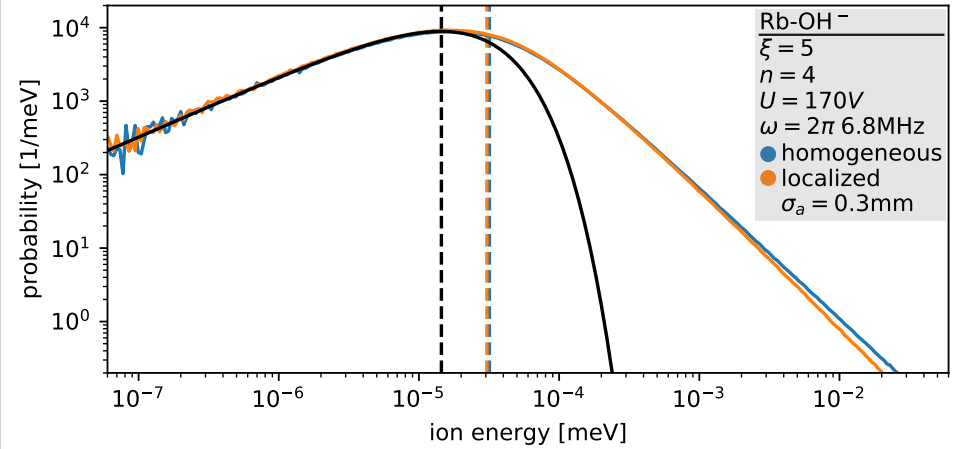

Figure 36: Normalized final energy distribution for OH^- anions, trapped in an infinitely long octupole rf trap ($n = 4$). The rf voltage U and rf frequency ω is chosen to be the same as in the experimental setup. The blue line represents the final energy distribution for a homogeneous buffer gas cloud and the orange line shows the distribution for a localized Gaussian-shaped atom cloud with a width of $\sigma_\mathrm{a} = 0.3$ mm, which is the typical width, used in this work. The black line illustrates the thermal energy distribution at $T_\mathrm{a} = 200$ µK. The dashed lines represent the mean energy of the shown distributions.

4.1.2 THERMALIZATION BEHAVIOR TOWARDS STEADY STATE

In the previous section, the interest was the steady state distribution and the collisions relevant for the thermalization were ignored to make the final steady state independent of the initial starting conditions. However, for the interest of efficient sympathetic cooling, it is important to know how fast this steady state is reached. The existing model has been altered to derive the change for a set of ions in time. The initial ion distribution was chosen to be a thermal distribution in the ponderomotive potential of a n'th order multipole trap:

$$p(E_\mathrm{i}) \propto E_\mathrm{i}^{\frac{1}{2}+\frac{1}{n-1}} \exp\left(-\frac{E_\mathrm{i}}{k_\mathrm{B}T}\right). \tag{87}$$

From this distribution, derived by applying the virial theorem, a set of initial ion energies are sampled. Following section 4.1.1 for each ion a random collision is calculated and saved. This way, the evolution of the whole ion set is calculated after every ion undergoes one collision. The newly determined energy distribution is then used to calculate the next collision. Since the likelihood of collisions differs depending on their energy and velocity direction, the time of free flight time between two consecutive collisions is computed by the Langevin collision rate of each single ion in the atom cloud, similar to equation 85.

Figure 37 shows the evolution of OH^- anions in an octupole trap, overlapped with a localized atom cloud. The trap and atom cloud parameters are similar to the previously shown steady state solution in Figure 36. An energy set of 10^5 ions were sampled from a thermal distribution at $T_\mathrm{i} = 370$ K. The binned initial energies are shown as gray solid points in the inset of Figure 37. The gray dashed line corresponds to the normalized thermal probability distribution the initial ion energies were sampled from. After every collision, the energy of each single ion was stored until 250 collisions were reached. Taking the time of free flight between consecutive collisions into account, the number of collisions is transferred into a time. Figure 37 shows in blue the evolution of the mean ion energy as a function of time. The black dashed line corresponds to the steady state mean energy calculated for 10^6 collisions in this system. The corresponding energy distribution is also depicted in the inset as a dashed black line. The red line, however, is illustrating the Boltzmann distribution at the atoms' temperature $T_\mathrm{a} = 200$ µK. Multiple energy distributions during the thermalization process are shown in the inset as points, corresponding to the initial sample ions and the energy distribution after 10, 25, 50 and 100 collisions. After 10 collisions, the mean energy dropped by a factor of 22, while after 25 collisions the mean energy is already reduced by three orders of magnitude.
In our system about 100 collisions are needed to fully converge to the calculated steady state energy distribution calculated in section 4.1.1.

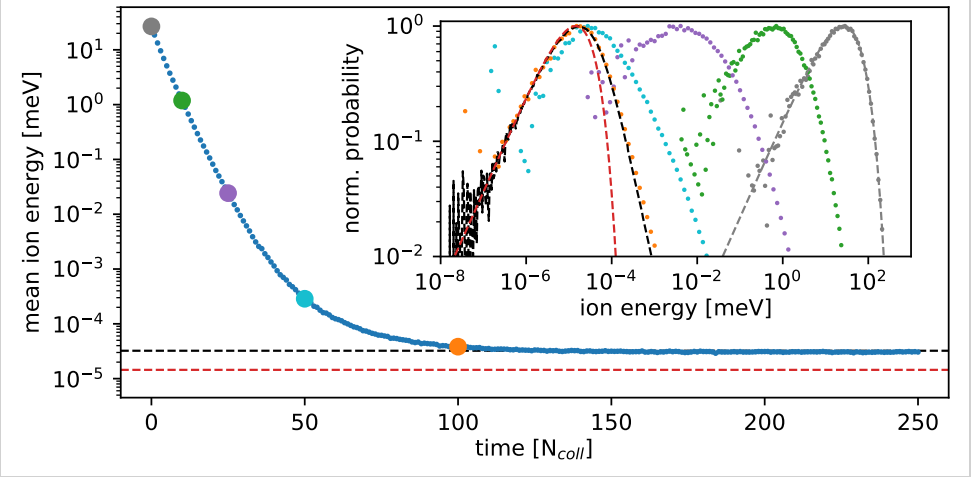

Figure 37: Evolution of the mean ion energy as a function of time, corresponding to the number of collisions. The dashed lines represent the mean energy of the energy distributions shown in the inset. The colored enlarged points correspond to the energy distributions shown in the inset. The calculated energies after a collision are binned in time and energy. The initial distribution corresponds to a thermal distribution with $T_i = 370$ K, shown as dashed gray line in the inset. The sampled initial energy distribution is depicted as gray points. The black dashed line represents the mean energy of the steady state energy distribution for 10^6 collisions, also shown in the inset. The red dashed line corresponds to the thermal distribution at the atoms temperature $T_a = 200$ µK.

In Figure 34, illustrating the collisions in a rf trap, one can see that the cooling dynamics are dominantly dependent on the mass ratio between the coolant and the ions. For the three different mass ratios, depicted in the previously shown figure, the cooling dynamics were calculated upto the 100'th collision. Figure 38 shows the evolution of the mean energy for these three systems. As expected, the final mean energy depends on the mass ratio. For the heavier atoms, it is the largest, and for the helium case it is the lowest and resembling to the thermal distribution. The cooling efficiency is the highest for equal masses, since the momentum exchange is more efficient, as illustrated for a collision close to the trap center in Figure 34.

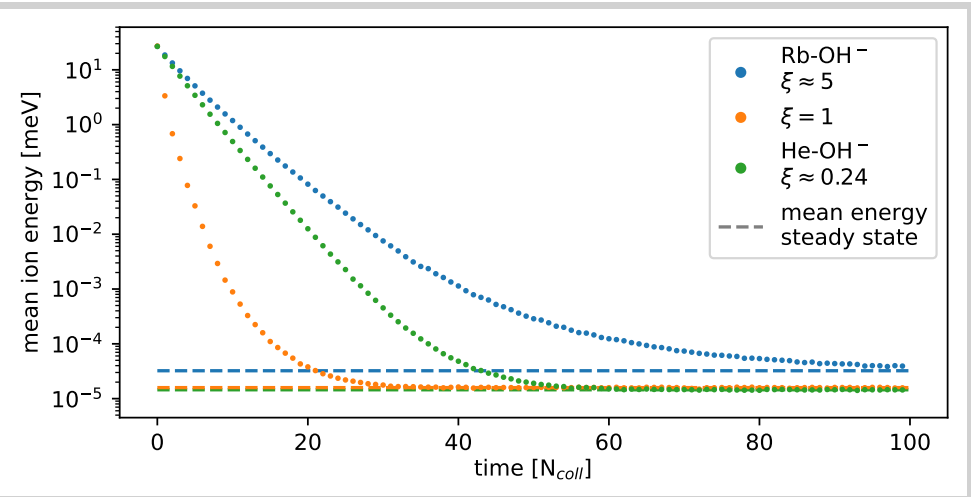

Figure 38: Evolution of the mean energy as a function of time for the three mass ratios, which are used to illustrate the collision of an ion with a neutral particle in an rf trap, see Figure 34. The calculated dynamics correspond to homogeneously distributed rubidium (blue), neutral of equal mass (orange) and helium atoms (green). The dashed lines represent the final mean energy of the steady state calculations for 10^6 collisions.

4.2 REACTIVE ATOM-ION COLLISIONS

It was established in section 4.1, that for efficiently cooling anions in a rf trap, a sufficient number of elastic collisions are required. However, anions tend to lose their additional electron during reactive collisions, leading to an ion loss. These ion losses prevent the cooling of anions, as they cannot undergo sufficient collisions to reach their steady state temperatures/energies.

4.2.1 ASSOCIATIVE DETACHMENT REACTION: OH^- AND RUBIDIUM

Theoretical studies on the Rb-OH^- system show that reactive collisions leading to an ion loss are likely to occur [106, 107]. The dominant reaction path for the ground-state rubidium atom is associative electronic detachment (AED). In the case of rubidium and the closed shell OH^- molecule, the collision partners form an intermediate reaction complex, which binds the additional electron via dipole forces. However, if the dipole of the complex becomes too small, the excess electron is lost and the neutral rubidium hydroxide molecule is formed:

$$\mathrm{Rb}(^2\mathrm{S}) + \mathrm{OH}^- \rightarrow \mathrm{RbOH} + e^- \tag{88}$$

The reactivity of this collision is reduced by steric effects, since only in a small angular space of the collision, it is possible that the dipole drops below the critical value, required to bind the excess electron. In the before mentioned *ab-initio* calculations, the reaction rate constant is predicted to be $4.2 \cdot 10^{-10}$ cm^3/s, which is an order of magnitude lower than the classical Langevin atom-ion collision rate constant of the ground state $k_{\mathrm{L},^2\mathrm{S}} = 4.3 \cdot 10^{-9}$ cm^3/s.

Since the detachment process happens when the collision partners are close together and the dipole moment is small, the calculations mentioned are strongly dependent on the effective core potential used to model the rubidium atom. Figure 39 shows the potential energy surfaces (PES) calculated using three different rubidium effective core potential. A crossing between the PES of the anionc and the neutral rubidium hydroxide complex corresponds the the inter-particle distance, at which the dipole of the molecule is to small to bind the excess electron. It is shown, that the relative energy needed to reach the crossing is strongly the dependent on the atom core approximation. Thus, by measuring the reaction rate coefficient accurately, one is able to benchmark different models for the description of the rubidium atom.

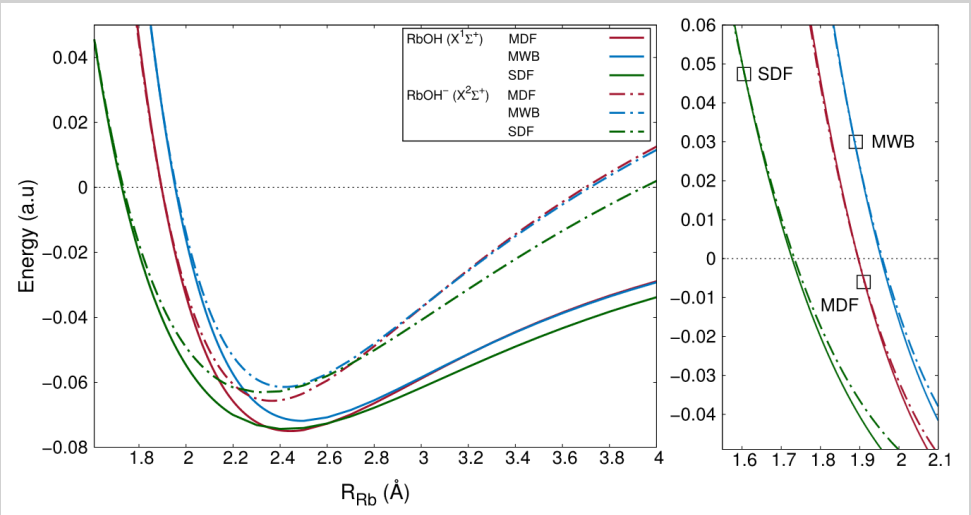

Figure 39: Potential energy surfaces (PES) for a ground state rubidium atom approaching the OH^- molecule co-linearly on the oxygen side. The dashed curves correspond to the anionic, the solid curve to the neutral rubidium hydroxide complex. The crossing of the dashed and the solid curves, gives the inter-particle distance, at which the excess electron is lost. The colors illustrate the different effective core potentials used to calculate the PES [106].

However, in the HAITrap experiment the atoms are stored in a magneto-optical trap, which leads to a fraction of atoms being in an excited electronic state, $Rb(^2P)$. The energy stored in the excited state opens up new exothermic reaction paths:

$$Rb(^2P) + OH^- \rightarrow RbOH + e^- \tag{89}$$

$$Rb(^2P) + OH^- \rightarrow Rb^- + OH \tag{90}$$

The reaction rate coefficient for the excited rubidium entrance channel is theoretically expected to be close to the coefficient derived from the classical capture model $k_{L,^2P} = 7.2 \cdot 10^{-9}\ cm^3/s$, which results in a drastically high loss rate. To suppress the number of excited rubidium atoms, the magneto-optical

trap is set up in a darkSPOT configuration, which allows to control and reduce the ratio of excited to ground state atoms (see section 2.2.2). This ratio can be estimated by measuring in the absorption imaging only the atoms still in the bright state or the total atom number, by a repumping pulse before the imaging. This characterization process is explain in detail in section 2.2.3. With the number of atoms in the bright state, the cooling light intensity and frequency, the number of excited atoms can be estimated by the atom-light scattering rate, equation 35. The ratio between bright state and total atom number in this work is typically 30% and the cooling light intensity 36 mW/cm^2. For a frequency detuning of 12 MHz the excited state fraction is estimated to be about 10%.

To characterize the loss of OH^- anions, due to reactive collisions with rubidium atoms, a loss measurement was performed. Figure 40 illustrates the experimental measurement procedure. After the initialization method of the ion ensemble is completed, the atom cloud is loaded by switching on the necessary cooling light. The ion and the atom cloud are concentrically overlapped, leading to a loss of ions. The ion number and temperature were measured by extracting the ions after a certain interaction time with the atoms. At the same time an atom cloud characterization measurement was performed, via saturation absorption imaging (see section 2.2.3), to derive the atom cloud size and density.

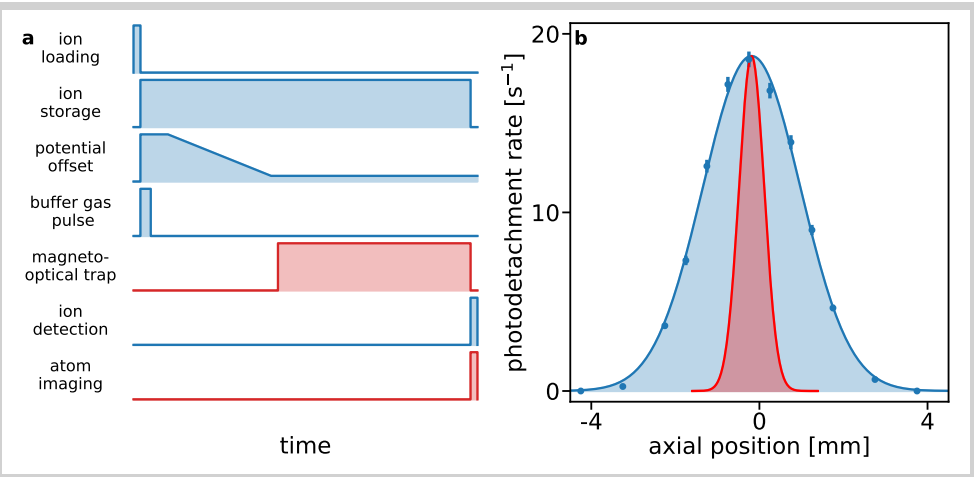

Figure 40: Procedure of reactive loss measurements. **a**, schematic representation of the experimental measurement cycle. The ion initialization includes the loading, the thermalization to the helium buffer gas and the potential manipulation. Subsequently, the atom cloud is loaded concentric to the ion distribution. After a certain interaction time, the atom cloud is characterized via saturation absorption imaging and the ions are extracted to the detector. **b**, the blue region shows the ion distribution measured via photodetachment tomography. The red distribution illustrates the typical extent of the atom cloud.

As explained in section 2.3.1 the collision rate can be expressed by a reactive collision rate coefficient k_r and the overlap integral between the atom and the ion cloud:

$$\dot{N} = -k_r N \int \underbrace{n_a(x,y,z,t)\rho_i(x,y,z,T)}_{\Phi_{ia}(x,y,z,t)} \mathrm{d}x\mathrm{d}y\mathrm{d}z - \nu_{bgr} N, \tag{91}$$

where $\rho_i(x,y,z,T)$ is the temperature-dependent normalized ion distribution and $n_a(x,y,z,t)$ the time-dependent atom distribution. $\nu_{bgr} = 0.009(1)\ \mathrm{s}^{-1}$ is the ion trap's background loss rate and $\Phi_{ia}(x,y,z,t)$ is called the time-dependent atom-ion overlap.

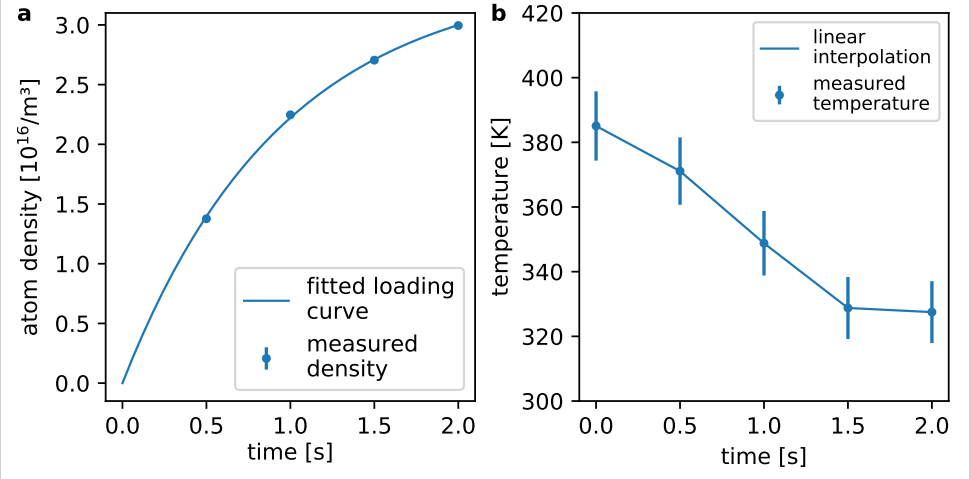

Figure 41: Measured evolution of atom density and OH^- anion temperature. **a**, shows the atom density as a function of time after the loading started. The atom density is fitted by an exponential loading curve, yielding a loading time of $\tau_{load} = 0.95(3)$ seconds. **b**, OH^- anion temperature measured via the time of flight thermometry method. The solid line represents a linear interpolation between the measured data.

Figure 41 shows the measured evolution of the atom cloud density and the ion temperature as a function of interaction time of both species. The time-dependent overlap integral is calculated, corresponding to section 2.3.1, with the determined atom density loading time $\tau_{load} = 0.95(3)$ seconds and the atom with growing time $\tau_{growth} = 0.14(5)$ seconds. By plugging this time-dependent overlap into equation 91 and fit the numerical solution to the measured ion number, one can derive the reaction rate coefficient k_r.
Figure 42 shows the normalized measured ion number, corresponding to the measurement of the atom cloud loading and ion temperature depicted in Figure 41. The ion number drops within the 2 seconds interaction time of both specie to 20% of the initially loaded number of ions. The ion loss is therefore much higher than the loss expected from the low background loss rate $\nu_{bgr} = 0.009(1)\ \mathrm{s}^{-1}$, which was determined by an additional measurement shown in the inset. The blue solid line corresponds to fitted the solution of the differential equation 91 with a reaction rate coefficient of

$k_r = 9.0(2) \cdot 10^{-10}$ cm^3/s. This value is about five times smaller than the collision rate coefficient, derived from the Langevin model for the ground state $k_{L,^2S} = 4.3 \cdot 10^{-9}$ cm^3/s and the excited state $k_{L,^2P} = 7.2 \cdot 10^{-9}$ cm^3/s. Thus, in this system there will be about an average of four elastic collision before a reactive loss collision occurs.
This high loss rate will limit achieving the final energy possible via sympathetic cooling of OH^- by rubidium, since the mean energy calculated in the previously mentioned numerical model drops in four collisions only be about a factor of four.

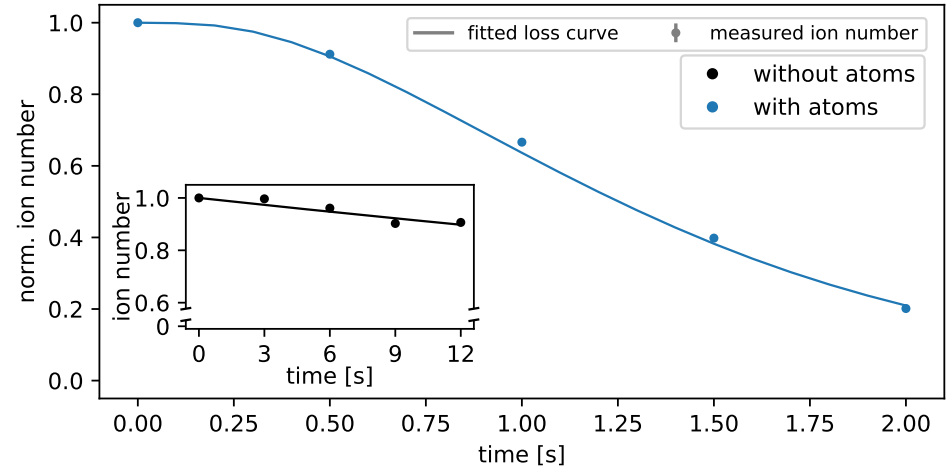

Figure 42: Measured loss of OH^- anion, due to reactive collisions. The detected ion number normalized to the initially loaded number of ions are shown as blue points. The blue solid line corresponds to the fitted numerical solution of the differential equation 91, yielding the reaction rate coefficient $k_r = 9.0(2) \cdot 10^{-10}$ cm^3/s. The inset shows the determination of the background loss rate without an overlapped atom cloud. The solid line corresponds to a fitted exponential decay function, with a background loss rate of $\nu_{bgr} = 0.009(1)$ s^{-1}.

Regarding the comparison to the *ab-initio* calculations, the measured reaction rate coefficient is slightly lower than the calculated reaction rate coefficient for an excited state fraction of 10%, $k_{theo} = 11.3 \cdot 10^{-9}$ cm^3/s. In a systematic measurement, the excited state fraction was changed over a large range. This way, a ground state reaction rate coefficient of $k_{gs} = 0.85(7) \cdot 10^{-9}$ cm^3/s and for the excited state $k_{es} = 2.1(4) \cdot 10^{-9}$ cm^3/s was measured. Note, that theses reaction rate coefficients are calculated and measured for high relative collision energy ($T \sim 300$ K). In comparison to the theoretical predictions, the ground state reaction rate coefficient is two times larger, whereas the excited state reactivity is reduced, hinting at the presence of other stabilization processes at play. However, the discussion of these reaction dynamics are not included in the scope of this thesis.

4.2.2 DETACHMENT LOSS CHANNELS OF O^-

The reactivity of the Rb-O^- system on the other hand differs completely from the OH^- case, because the excess electron is valence bound in the RbO^- complex. Similar to other alkali-monoxide anions, accessible states of the RbO^- complex, from the ground state entrance channel, are expected to be stable against autodetachment [108]. Thus, the reaction rate coefficient for O^- and rubidium is expected to be much smaller compared to the OH^-– Rb system.
Similarly to the measurement performed for OH^-, the atom loading curve and the temperature dependency on the interaction time between atoms and anions are shown in Figure 43.

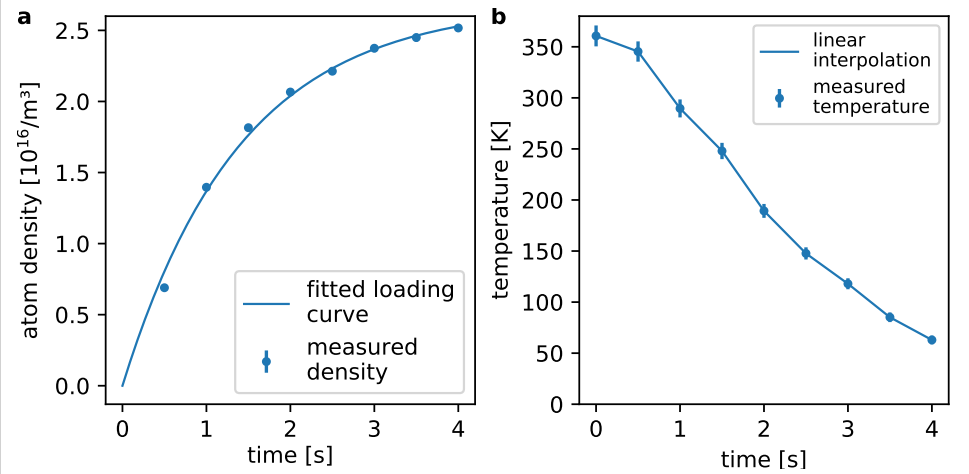

Figure 43: Measured evolution of atom density and O^- anion temperature. **a**, shows the atom density as a function of time after the loading started. The atom density is fitted by an exponential loading curve, yielding a loading time of $\tau_{\text{load}} = 1.40(8)$ seconds. **b**, O^- anion temperature measured via the time of flight thermometry method. The solid line represents a linear interpolation between the measured data.

Since the radial potential is mass dependent (see section 2.1.1), the photodetachment tomography benchmark measurement to determine the trapping potential has also been performed for the O^- anion:

$$\begin{aligned} V_{O^-}(x,y,z) =& 1.86(10)\cdot 10^{-15}\,\mathrm{J/m^2}\cdot z^2 + \\ &+ 5.2(5)\cdot 10^{-3}\,\mathrm{J/m^6}\cdot (x^2+y^2)^3. \end{aligned} \tag{92}$$

The transition frequency of the cooling light, required for the magneto-optical trap (780 nm), is below the photodetachment threshold for O^- (849 nm). Thus, an additional loss channel opens up. The MOT beams are much larger than the ion cloud, therefore the light intensity can be treated as constant for all positions in the ion trap. Hence, the cooling light has no evaporative heating or cooling effect on the anions' energy distribution, as discussed in chapter 3. The photodetachment loss can be treated as an additional background loss.

Figure 44 shows two measurements, in blue the anion loss as a function of interaction time with the atoms and in black the same measurement configuration is shown, including the cooling light, but without any atoms loaded. The photo-induced background loss rate is fitted with an exponential loss function, yielding a loss rate of $\nu_{\mathrm{bgr}} = 0.211(1)\ \mathrm{s}^{-1}$. The fitted loss curve is shown as a solid black line. The blue line corresponds to the fitted solution of the differential equation 91, including the additional background loss and the trapping potential for O^-. The reaction rate coefficient is determined to be $k_{\mathrm{r}} = 1.56(3) \cdot 10^{-10}\ \mathrm{cm}^3/\mathrm{s}$, which is about six times less than for the molecular anion OH^- and about 30 times smaller than the Langevin collision rate. Thus, the cooling of O^- is expected to be more efficient than for OH^-.

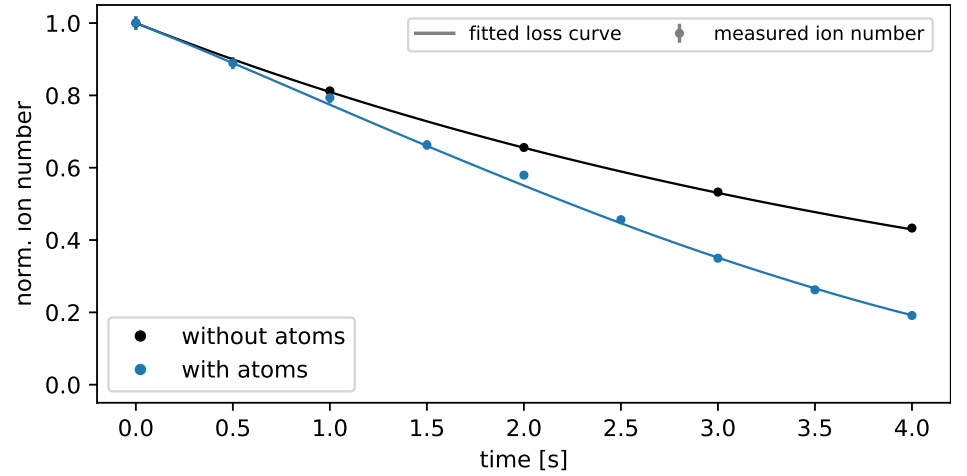

Figure 44: Measured loss of O^- anions, due to reactive collisions with the atoms and photodetachment via the magneto-optical trap cooling light. The black points represent the measured ion number normalized to the initially loaded ions without atoms, but with the cooling light switched on. The black solid line corresponds to a fitted exponential decay, with a loss rate of $\nu_{\mathrm{bgr}} = 0.211(1)\ \mathrm{s}^{-1}$. The blue points show the normalized detected ion number with the same cooling light configuration, but with loaded atoms. The blue line corresponds to the fitted numerical solution of equation 91, yielding a reaction rate coefficient of $k_{\mathrm{r}} = 1.56(3) \cdot 10^{-10}\ \mathrm{cm}^3/\mathrm{s}$.

4.3 ANION COOLING IN A HYBRID ATOM-ION TRAP

For the description of the sympathetic cooling dynamics, the ion-ion collision rate is essential. In Chapter 3 it was discussed, that with cooling the ions, the ion-ion self-thermalization rate increased drastically, which leads to a redistribution of the ions' energy. To quantify the dynamics, a thermodynamic approach is developed in section 4.3.1. Since the loss behavior for O^- and OH^- differs tremendously, the cooling dynamics are expected to differ as well. In section 4.3.2, the cooling of both species is presented. For both anions the cooling dynamics are measured for five different atom cloud positions,

to change the relative overlap between the ion-atom clouds and derive the influence of the relevant collision rates in the system.

4.3.1 THERMODYNAMIC DESCRIPTION OF ANION-ATOM COLLISIONS

Similar to the model describing the evaporative cooling in chapter 3, one assumes a high ion-ion thermalization rate, compared to any other relevant rate, as the ion-atom elastic and the ion-atom reactive collision rate. Thus, the ion ensemble can be described in a quasi-static picture, by its mean energy.

In the simple case of a gas with a thermal energy $\langle E_\mathrm{i} \rangle$, thermalizing to a heat bath, with a constant thermal energy $\langle E_\mathrm{a} \rangle$, particles collide and energy is transferred. The change in energy is then described by the rate of collisions $\dot{N}_\mathrm{coll}$, the mean relative energy exchange $\left\langle \frac{\Delta E}{E} \right\rangle$ and the difference in the mean energy of the two gases:

$$\langle \dot{E}_\mathrm{i} \rangle = \left\langle \frac{\Delta E}{E} \right\rangle \dot{N}_\mathrm{coll} \left(\langle E_\mathrm{a} \rangle - \langle E_\mathrm{i} \rangle \right). \tag{93}$$

The mean relative energy exchange per collision is dependent on the mass difference and is determined by averaging over all possible collision angles in equation 79, yielding $\left\langle \frac{\Delta E}{E} \right\rangle_{\text{Rb-OH}^-} = 0.2778$ and $\left\langle \frac{\Delta E}{E} \right\rangle_{\text{Rb-O}^-} = 0.2666$.
The atom-ion collision rate coefficient can be derived from the Langevin capture model, which when multiplied with the atom-ion overlap integral yields the collision rate:

$$\dot{N}_\mathrm{coll} = k_\mathrm{el} \int \rho_\mathrm{i}(x,y,z) n_\mathrm{a}(x,y,z) \mathrm{d}x\mathrm{d}y\mathrm{d}z. \tag{94}$$

The Langevin scattering model is a valid assumption, since the collision energies discussed here, are far above the regime in which only a few partial waves contribute to the collision cross section [105, 50].
Similar to the single particle description in section 4.1, one can transfer the ions' micromotion to the atoms, resulting in a radius-dependent effective mean atom energy:

$$\langle E_\mathrm{a,eff}(r) \rangle = \frac{3}{2} k_\mathrm{B} T_\mathrm{a} + \xi V_\mathrm{eff}(r). \tag{95}$$

The effective atom energy the ions see depends on the position of the atom cloud with respect to the ion ensemble. As well as the mean kinetic energy of the ions at that position. The change in the total energy of the ions, due to collisions with localized atom cloud, is then given as:

$$\langle \dot{E}_\mathrm{i,tot} \rangle = k_\mathrm{el} \left\langle \frac{\Delta E}{E} \right\rangle \int \left[\langle E_\mathrm{a,eff}(x,y) \rangle - \langle E_\mathrm{i,kin}(x,y,z) \rangle \right] \rho_\mathrm{i}(x,y,z) n_\mathrm{a}(x,y,z) \mathrm{d}x\mathrm{d}y\mathrm{d}z. \tag{96}$$

In the case of an ion ensemble in an octupole trap, the mean total energy is derived from the virial theorem $\langle E_\mathrm{i,tot} \rangle = \frac{7}{3} k_\mathrm{B} T$. The mean kinetic energy is

derived from the mean total energy and and the mean potential energy the ions have at the position of the atom cloud. Combining this, with the atoms' effective energy from equation 95 gives the following change in mean total ion energy, or temperature:

$$\dot{T} = k_{\mathrm{el}} \left(\frac{3}{7k_{\mathrm{B}}}\right) \left\langle \frac{\Delta E}{E} \right\rangle \int \left[\left(\frac{3}{2} k_{\mathrm{B}} T_{\mathrm{a}} + \xi V_{\mathrm{eff}}(x,y) \right) - \left(\frac{7}{3} k_{\mathrm{B}} T - V_{\mathrm{O}^-}(x,y,z) \right) \right] \rho_{\mathrm{i}}(x,y,z,T) n_{\mathrm{a}}(x,y,z,t) \mathrm{d}x\mathrm{d}y\mathrm{d}z + \left(\frac{3}{7}\right) \left(\frac{1}{3}\right) T\bar{\epsilon}\nu_{\mathrm{ii}}(T), \tag{97}$$

including also the ion-ion heating rate $\dot{T}_{\mathrm{heat}} = \left(\frac{3}{7}\right) \left(\frac{1}{3}\right) T\bar{\epsilon}\nu_{\mathrm{ii}}(T)$, which was introduced in chapter 3 in equation 75. The change in the ion loss is described similar to the reactive loss measurement, however, this time the ion temperature is coupled to the differential equation 97:

$$\dot{N} = -k_{\mathrm{r}} N \int \rho_{\mathrm{i}}(x,y,z,T) n_{\mathrm{a}}(x,y,z,t) \mathrm{d}x\mathrm{d}y\mathrm{d}z - \nu_{\mathrm{bgr}} N. \tag{98}$$

With a measurement of the atom cloud's position and the evolution of the cloud's density and size, the two coupled differential equations can be solved numerically, providing a full thermodynamic description of the sympathetic cooling dynamics in an octupole rf trap.

4.3.2 SYMPATHETIC COOLING OF O^- AND OH^- VIA ULTRACOLD RB

The cooling measurements were performed similarly to the experimental measurement procedure to determine the reaction rate coefficient, see Figure 45 **a**. The initially loaded $\sim$ 1000 ions are thermalized to about 370 Kelvin. The trapping potentials are ramped down to a trap offset of 30 volts. The time used to prepare the potential is sufficiently long to also pump out the helium buffer gas, reaching a vacuum of 10^{-9} mbar. The atom cloud density and size, as well as the ion number and temperature were measured as a function of interaction time between both clouds. These measurements were performed for different atom cloud positions along the axial trapping direction, as illustrated in Figure 45 **b** for a typical atom cloud width of $\sigma_{\mathrm{a}} = 0.3$ mm. The atom cloud was shifted axially by an additional homogeneous magnetic field, generated by a coil placed outside the trapping chamber. In radial direction both clouds were placed concentrically to the ion trap center.

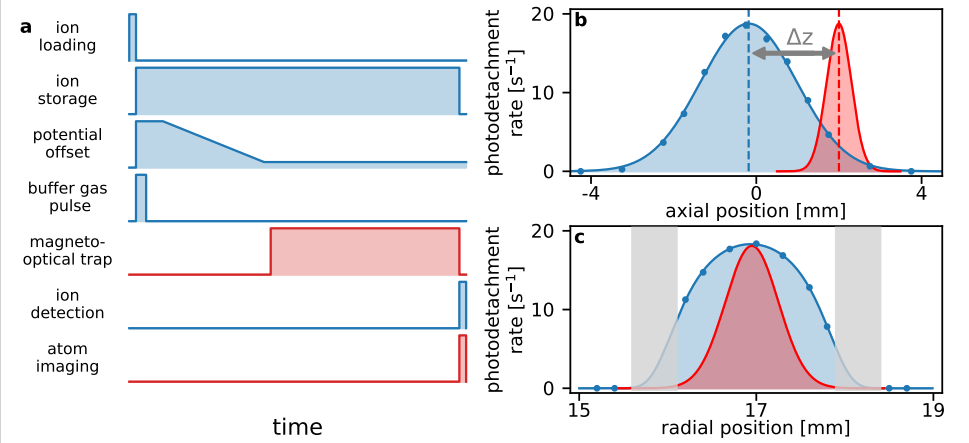

Figure 45: Experimental measurement procedure for sympathetic cooling of O^- or OH^-. **a**, schematic representation of the experimental measurement cycle. **b**, blue region shows the axial ion distribution measured via photodetachment tomography, fitted by a Gaussian function. The red Gaussian function illustrates a typical atom cloud distribution, displaced from the ion cloud center by Δz. **c**, the blue points represent the ions' radial distribution measured via photodetachment tomography. The atom cloud is positioned concentrically to the ions in the radial plane. The shaded gray areas represent the wires of the octupole trap.

Figure 46 shows the sympathetic cooling of O^- anions via elastic collsisions with ultracold rubidium atom in a darkSPOT configuration. **a** shows the evolution of ion temperature determined via time of flight thermometry and **b** the normalized detected number of ions. The black points represent a background measurement without any atoms, but with the cooling light switched on. The colored points show the cooling measurements for different MOT positions. With larger distance between the cloud centers, the cooling is slower and an offset occurs. This can be explained by a smaller overlap and with cooling the ions and the resultant shrinking of the ion cloud, the two clouds separate. In the two measurements, in which the two clouds are almost overlapped concentrically, $\Delta z = -0.3$ mm and $\Delta z = 0.38$ mm, the ions are cooled down within three seconds to a temperature of 30(2) Kelvin, 34(2) Kelvin respectively.

The solid lines are the evolution of ion temperature and ion number calculated via numerical integration of the coupled differential equations 97 and 98, starting with the initially determined ion temperature and ion number at $t = 0$ s. The evolution of the atom cloud parameters are for each measurement fitted with exponential loading curves and included as the time-dependent atom density in the two differential equations 97 and 98. In the case without atoms, the solution is shown in black and is essentially the ion-ion rf heating and the photodetachment loss. Thus, similar to the thermodynamic model for the evaporative cooling, in this model all parameters can be predetermined and the equations of evolution are numerically solved.

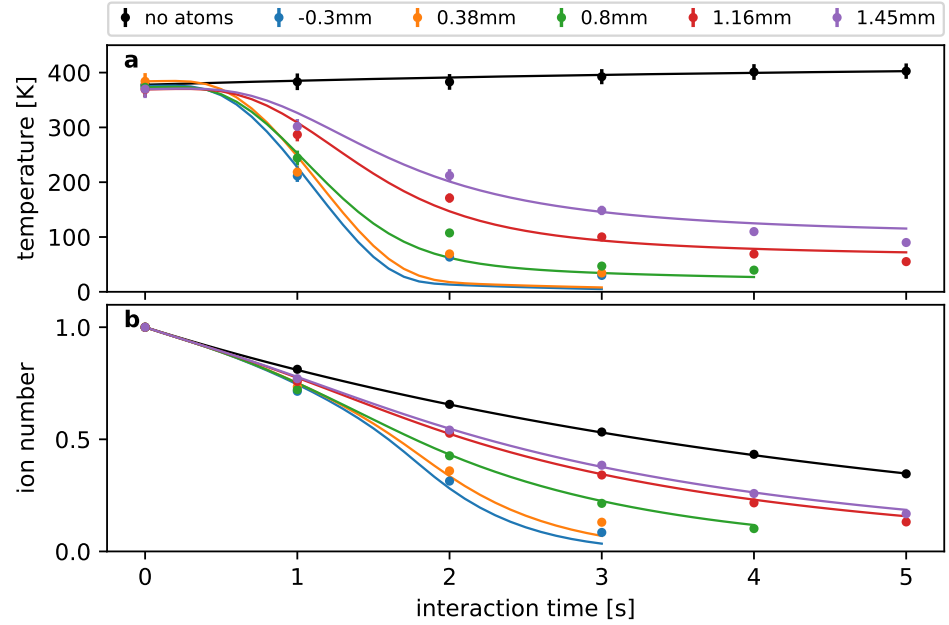

Figure 46: Temporal evolution of **a**, the O^- ions' temperature and **b**, the normalized ion number. The colored points correspond to the ion temperature and number measured as a function of interaction time with the atoms for different atom cloud positions Δz. The black points are measured without atoms, but the cooling light switched on. The solid lines correspond to the numerical solution of the coupled differential equations 97 and 98, taking the initial ion conditions and the atom cloud loading into account.

While the measured data of the outer-most MOT positions is modeled quite well, for smaller distances between the two clouds, one can see large deviations in the temperature. These deviations can be explained by a high ion-atom elastic collision rate, which leads to a contradiction of our initial assumption that the ion-ion thermalization rate is always higher. Figure47 **a** and **c** shows the behavior of the three relevant collision rates in the system for the atom cloud position $\Delta z = -0.3$ mm and $\Delta z = 1.16$ mm. The collision rates are determined for the measured conditions for each interaction time of the two clouds, as following:

$$\nu_{\mathrm{th}} = \frac{ne^4 \log \Lambda_{\mathrm{ii}}}{12\epsilon_0^2 \sqrt{\pi^3 m (k_{\mathrm{B}} T)^3}}, \tag{99}$$

$$\nu_{\mathrm{el}} = k_{\mathrm{el}} \int \rho_{\mathrm{i}}(x,y,z,t) n_{\mathrm{a}}(x,y,z,t) \mathrm{d}x\mathrm{d}y\mathrm{d}z, \tag{100}$$

$$\nu_{\mathrm{r}} = k_{\mathrm{r}} \int \rho_{\mathrm{i}}(x,y,z,t) n_{\mathrm{a}}(x,y,z,t) \mathrm{d}x\mathrm{d}y\mathrm{d}z, \tag{101}$$

where ν_{th} is the ion-ion self-thermalization rate, ν_{el} the atom-ion elastic collision rate and ν_{r} the atom-ion reactive collision rate. The solid lines shown in Figure 47 **a** and **c** are a guide to the eye. One can see, that for a small distance in panel **a** the atom-ion elastic collision rate and the ion-ion thermalization rate

increase with cooling the ions. Since they are of the same size, the assumptions of both models introduced break down. In the model in section 4.1, describing only atom-ion elastic collisions, the ion-ion thermalization is ignored, whereas in the thermodynamic model, the ion-ion thermalization rate is expected to be much larger than any other rate. The non-thermalicity can also be seen in the measured TOF distribution. In panel **b**, one can see deviations from the fitted Gaussian distribution, which one expects for a thermal ion distribution before the extraction. Note, that the given temperatures in Figure 46 correspond to the TOF width derived by the Gaussian fit and the non-thermalicity of the distribution is not taken into account.

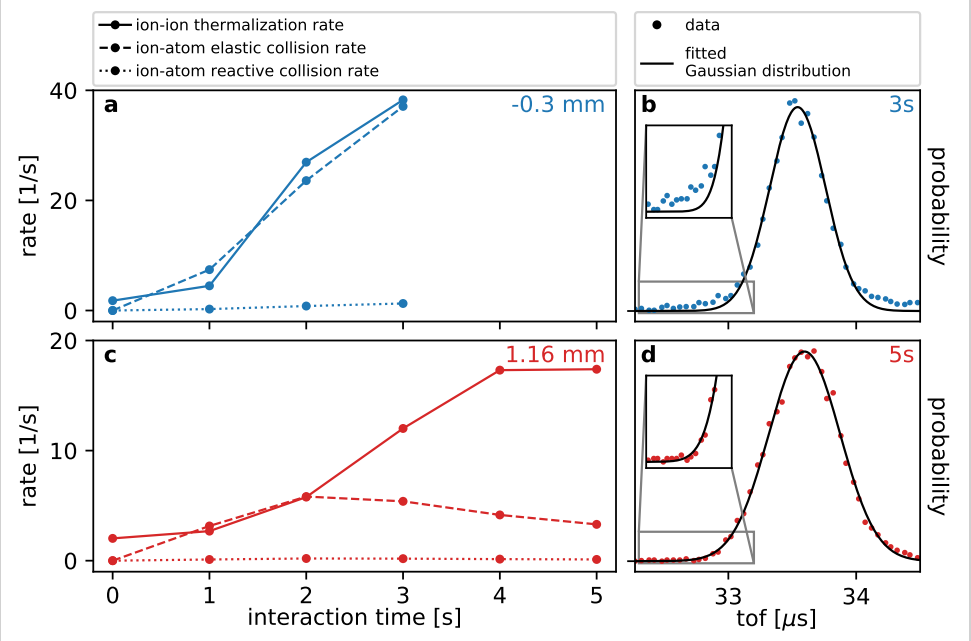

Figure 47: Relevant collision rates in the Rb-O^- system for two different atom cloud displacements. **a**, ion-ion thermalization rate and atom-ion collision rates for $\Delta z = -0.3$ mm. **b**, time of flight distribution after the longest interaction time with the atoms $t = 3$ s at $\Delta z = -0.3$ mm. **c**, relevant rates for $\Delta z = 1.16$ mm. **d**, time of flight distribution after the longest interaction time with the atoms $t = 5$ s at $\Delta z = 1.16$ mm.

On the other side, for the displaced atom cloud, the ions and atoms separate with the cooling of the ions. Thus, the overlap shrinks and therefore the elastic collision rate. Panel **d** shows the measured TOF distribution after 5 seconds interaction time, which is well-represented by the fitted Gaussian function. Therefore, one can expect that the ions undergo complete thermalization before the extraction. Also shown is, that the reaction rate is small compared to the other two rates, which means that the assumptions of the thermodynamic model are valid. The reaction rate is small compared to any other rate. Thus, evaporative effects, due to energy-selective reactions, can be neglected. The major loss channel of this system is due to photodetachment loss via the atom cooling light. Both loss channels can be suppressed by replacing the currently used magneto-optical trap by a far-red-detuned dipole trap. The dipole trap

provides a cloud of only ground state atoms. Thus, reactive losses are most likely suppressed. A dipole trap is operated with photon energies far-below any possible electronic transition. A typical wavelength of a rubidium dipole trap laser is 1064 nm and therefore, way below the photodetachment threshold of O^-.

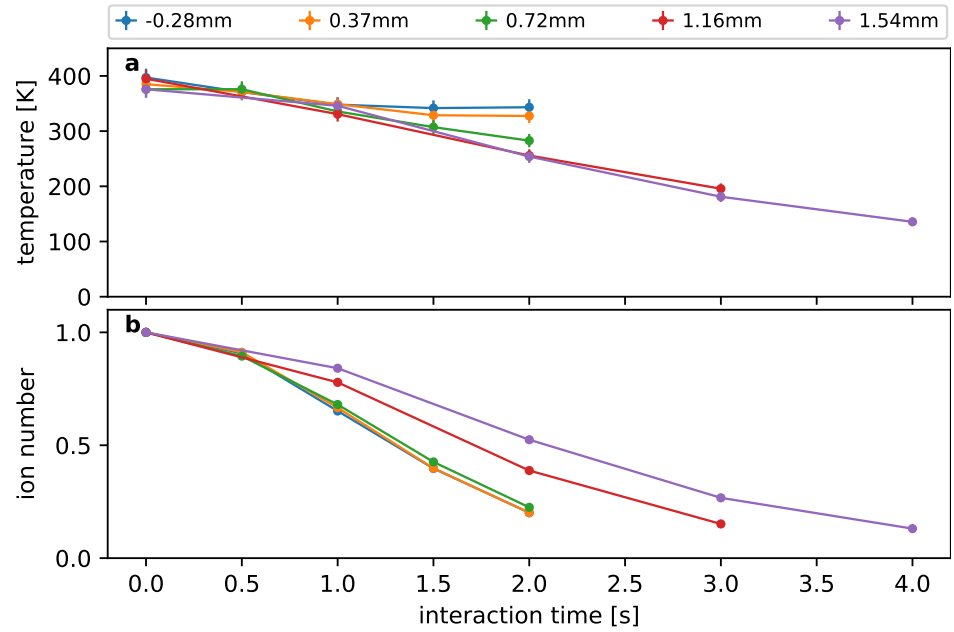

Figure 48: Temporal evolution of **a**, the OH^- ions' temperature and **b**, the normalized ion number. The colored points correspond to the ion temperature and number measured as a function of interaction time with the atoms for different atom cloud positions Δz. The solid lines are a guide to the eye.

Figure 48 shows the sympathetic cooling measurements of an OH^- anion ensemble overlapped with the atom cloud at similar positions, as previously shown for the O^- measurements. The thermodynamic model is not depicted in these graphs, because the high loss rate leads to a drop of the thermalization rate, contradicting the model's assumptions. The solid points represent the measured ion temperature and number, the lines are a guide to the eye. One can observe that the cooling behavior changes completely, compared to the previously shown results for O^-. The measurement at $\Delta z = -0.28$ mm levels off at 340(15) Kelvin for an initial starting temperature of 397(16) Kelvin, while for the largest distance between both clouds the cooling is more efficient, resulting in a final OH^- temperature of 135(8) Kelvin. This different cooling behavior can be most likely attributed to the high reaction rate between rubidium and OH^-. When the ions and atoms are almost overlapped concentrically in the trap center, the reactive collisions between OH^- ions and Rb atoms result in the loss of low energy ions to drop or 'spill' out of the trap. Due to the loss of low energy ions, the temperature is limited far above

100 K, which was the expected mean energy after four elastic collisions, see Figure 37. For a larger displacement of the atom cloud, the elastic collisions first sympathetically cool the OH^- anions, due to which the ion cloud shrinks and is separated from the atom cloud. Thus, reducing the overlap and the reactive losses. Additionally, the reactive spilling of ions can lead to a removal of high energy ions, resulting in a colder ion ensemble.

Sympathetic cooling of negatively charged ions by a heavy ultracold buffer gas has been shown experimentally, for the first time, by these two sets of measurements. The results show the influence of different loss channels on the anion cooling dynamics. The reduced reactive rate between Rb and O^- favored the cooling of O^- species, which was the dominant loss channel for the molecular anions, OH^-, and hindered the cooling of OH^- anions to lower temperatures. The major and limiting loss channel of O^- is the photodetachment by the cooling light of the magneto optical trap. The measured cooling dynamics are well-described by a thermodynamic model, as long as the ion-ion thermalization rate is larger compared to any other relevant rate. One also has to include the rf field induce micromotion, accounted for in the effective mean atom energy [49, 51]. As previously mentioned, the loss channels in the Rb-O^- can be suppressed by the introduction of a dipole trap instead of an magneto-optical trap. Nevertheless, in the case of OH^-, the high reactivity of the rubidium ground state with OH^- is limiting the cooling even though the atoms are trapped in a dipole trap. However, there are alkali and earth-alkaline OH^- systems, for which a suppressed ground state reactivity is predicted [107]. The suppression of the reaction loss channels would not only allow to push the frontier of translational cooling far below the Kelvin range, it opens up the opportunity to efficiently cool the internal degrees of freedom. While for the Rb-OH^- system the state-changing collision rate are in the same order as the reactive collisions, no internal cooling is expected [21]. However, by the right combination of anion-atom species, the reactive loss channels can be suppressed, providing a technique to cool also the internal degrees of freedom far below the state-of-the-art, as seen for hybrid systems involving cations [41, 42]. The internal cooling allows to perform high-precision photodetachment spectroscopy, yielding detailed information about the internal structure of anionic and neutral molecules [24, 27, 28].

5 SYNOPSIS OF HYBRID ATOM-ION TRAPPING

As early as 1968, Major and Dehmelt postulated that the thermalization behavior between an atom and an ion in a radio frequency (rf) trap and therefore, the cooling of ions by a cold buffer gas, is not trivial [109]. They introduced the critical atom-to-ion mass ratio, which they estimated to be $\xi_{crit} \approx 1$ in a linear Paul trap. Above this critical mass ratio, the collisional induced energy transfer between the rf motion and the drift motion leads to a net ion heating and ion loss. If the atom is lighter than the ion, the ion becomes colder. However, the radio frequency heating still prevents the ions to thermalize to the atoms' temperature [74, 103, 105, 110]. Lower temperatures could be achieved with the development of multipole rf ion traps, most notably the 22-pole trap [62, 64]. The advantage of these traps is a large field-free region in which the rf motion amplitude is small and therefore, the heating is reduced. Buffer gas cooling via cryogenic helium in these kind of multipole radio frequency traps, is the state-of-the-art cooling technique for negatively charged particles. With this technique, translational temperatures of 10 Kelvin are reached [19]. Due to the close encounter in a collision between a neutral and a molecular anion, also the rotational degrees of freedom are cooled [25, 26]. It has been observed that the lowest rotational temperature is about 20 Kelvin, when the translation temperature is 10 Kelvin [111].
The buffer gas cooling via collisions with cryogenic helium is limited by the temperature of the coolant. With the emergence of laser cooling a new type of buffer gas is provided, ultracold atoms [36]. The combination between rf ion traps and laser cooled atoms have been successfully demonstrated in a variety of experiments for positively charged ions [40, 39, 112]. For instance, single ions were immersed in a degenerate Bose gas [113, 114], molecular cations cooled via collisions with ultracold atoms [44, 42, 37] and reaction dynamics at low relative energies [44, 45, 46]. Furthermore, sympathetic cooling was shown with ultracold buffer gas atoms heavier than the cooled cationic specie, as Cs-Rb^+ ($\xi \approx 1.5$) and Rb-K^+ ($\xi \approx 2$) [115].

First experiments with anions were performed, combining OH^-, stored in a octupole wire trap, with a magneto-optical rubidium trap [47]. The octupole wire trap combines the advantages of reduced rf heating and the optical access required for the atom trap. These first measurements didn't show cooling of OH^- but they showed that associative detachment reactions can occur in the presents of both species. However, the loss rate has been estimated to be sufficiently small compared to the cooling collision rate and that it can be even reduced by implementing a dark spontaneous-force trap (darkSPOT), which allows for higher atom densities and a lower ratio of excited state to ground state atoms.

These first measurements triggered theoretical investigations on the final steady-state ion energy distribution in such multipole traps, combined with a heavy buffer gas [48, 49]. The major result of these studies, is a general formula for the critical mass ratio in a n'th order pole trap, $\xi_{\text{crit}} = 1.5(n-1)$, and that this critical mass ratio can be overcome by localizing the atom cloud in an ion trap region of low rf amplitude and therefore low rf heating. These studies showed, that indeed the cooling of OH^- anions by a heavy buffer gas, as rubidium, should be possible, reaching energies close to the coolant's thermal energy.

In course of this work, the picture of sympathetic cooling of OH^- via collision with ultracold rubidium in a darkSPOT could be completed. It was found that, OH^- anions are sympathetically cooled best, when the atom and the anion cloud centers were displaced by 1.54 mm. The lowest final anion temperature measured is 135(8) K. The plasma discharge source also allowed to produce O^- anions. In the case of these anions co-trapped with ultracold rubidium atoms, the cooling behavior is reversed. For O^-, the lowest temperature measured is 30(2) K, when the atom and ion cloud are almost concentrically overlapped. The different dynamics are attributed to the dissimilar loss channels of the anions. The loss channels in both atom-anion system were identified and quantified. For OH^-, there is a reaction path with rubidium in the ground state, which leads to a high reactivity between the coolant atoms and the anions. With the determined reaction rate coefficient, the number of elastic collisions before an anion loss is estimated to be four, which is far lower than previously estimated. The limited number of elastic collisions explains the rather high resultant temperature of the anions. For concentrically overlapped clouds, low energy anions are more likely to get spilled out of the trap, which works against the cooling mechanisms and explains the improved cooling behavior for larger cloud displacements.
The reactivity of O^- is lower, since there is no ground state reaction path energetically accessible and the number of excited state rubidium atoms are reduced in the darkSPOT configuration of the atom trap. Another loss channel opens up for O^-, due to photodetachment via the atom trap cooling light. This loss channel limits the atom-ion interaction time, but it does not have an influence on the energy distribution, since the laser beams are much larger than the ion distribution. For high ion-ion thermalization rate, the cooling dynamics are well-represented by a thermodynamic model, assuming an elastic collision rate coefficient derived from the classical Langevin capture model and an effective mean atom energy, including the atoms' thermal energy and the ions' position dependent micromotion.
Although, the cooling is limited in both systems, Rb-O^- and Rb-OH^-, the limitations have been identified and they can be circumvented in future experiments.
The loss channels of O^- can be suppressed by the implementation of a rubidium dipole trap. A far-red-detuned dipole trap has three major advantages, compared to a darkSPOT. Firstly, the atoms in a dipole trap are in their elec-

tronic ground state. Thus, the excited state reaction channel is closed. The second advantage of a dipole trap is that, it is operated with far-red-detuned light, which has a lower photon energy than the detachment threshold and therefore, the photodetachment loss channel is also closed. This allows for a sufficient number of elastic collisions to reach the cold regime. The third advantage is, that in a dipole trap higher atom densities can be reached and therefore the atom-ion collision rate is increased.
In the case of the molecular anion OH^-, a transfer to a dipole trap would not improve the cooling, since the ground state reactivity is still about a quarter of the elastic collision rate. The neutral alkali hydroxide is stabilized during the reaction, when the dipole moment of the reaction complex becomes too small to bind the excess electron. Since this associative detachment process between the ground state atom and the closed-shell molecular anion happens at short inter-particle distance, the reactivity is strongly dependent on the alkali atom. Ab-initio calculations predict, that for other alkali species, as lithium, sodium and potassium, the associative detachment channel is suppressed [107]. The lower coolant to anion mass ratio is an additional advantage in the terms of cooling. Alternatively, ultracold alkaline earth atoms also provide a closed ground state associative detachment loss channel. A suppression of the loss channel would not only allow to cool a diatomic molecular anion to translational temperatures close to that of the coolant's, as seen for cations [41, 42], it would also enable the study of internal state-changing collisions [26, 88], and their influence on the quenching of an molecular anion's internal motion. High-precision photodetachment spectroscopy on cold molecular anions can resolve the internal structure of the anionic and the neutral molecule [116, 117, 27]. Furthermore the control over the molecular anion's internal degrees of freedom, enables studies of the reactive dynamics depending on the internal quantum state [44, 118]. Near-threshold photodetachment of anions have also been proven to be valuable tool to prepare transition-states, studying transient species in course of a chemical reaction[23].
Regarding future experiments in the HAITrap setup in Heidelberg, a fascinating feature of the plasma discharge source used in this experiment is that, in addition to O^- and OH^-, also OH^- with additional water molecules attached to the anion are produced. The production of theses hydrated anions, $OH^-(H_2O)_n$, were characterized in a Master thesis up to the eight order ($n = 8$) [72]. Theoretical calculations have shown that the additional water molecules stabilize the excess charge and with increasing order n, the reaction path resulting in $RbOH^-(H_2O)_{n-1}$ and H_2O becomes more and more suppressed, due to steric effects [119]. A detailed reaction measurement would give insights into the reactive dynamics of the rubidium and hydrated anion systems with increasing order n or structural complexity.
Another molecular anion, which awakens interest, is C_2^-, because it provides several stable electronic states, which could be used for laser cooling, and it is assumed to be part of the formation of larger carbon based anions in space [17]. Calculations predict that the rubidium ground state C_2^- reaction path is closed and that also the inelastic collision rate is in the order of the

Langevin rate, which allows for sufficient cooling of the internal degree of freedom [120]. Since the rethermalization, due to the black body field in a homo-nuclear diatomic molecule is hindered, it should also be possible to prepare ground state molecules. An interesting point, from an experimental physicist's point of view, is that the existence of stable electronic states, opens up the possibility to probe the anions via fluorescence imaging, which is, in comparison to the shown time of flight thermometry or the photodetachment tomography, a non-destructive diagnostic method.

In the course of the collision dynamic measurements the question arose, if a position dependent loss and therefore a potential energy dependent loss would lead to evaporative cooling or heating effects. Inferring from these thoughts, the idea to induce ion loss via photodetachment shaped up. Surprisingly, forced evaporative cooling via photodetachment had been proposed already more than 30 years ago [54], but it has never been experimentally demonstrated up to now. This thesis presented the forced evaporative cooling of molecular anions, OH^-, to a final temperature of $2.2(8)$ Kelvin in less than 4 seconds. It was shown, that with the reduction of the thermal energy by a factor of about 150, the phase space density was increased by more than three orders of magnitude and the anionic cloud was pushed towards a regime, in which the inter-particle Coulomb interaction becomes dominant, compared to the thermal energy (Coulomb coupling parameter $\Gamma \gtrsim 1$).
In order to describe the measured data, a thermodynamic model was introduced in this work. Due to the infinite-range of the Coulomb interaction between the ions, the self-thermalization rate is high, even for low ion numbers, which allows to describe the system in a quasi-thermal picture. The theoretical model yields two coupled differential equations describing the evolution of ion temperature and ion number dependent on the interaction time with the photodetachment laser light.
Solutions of the differential equations of evolution could be numerically calculated with a precise characterization of the trapping potential and the ion density distribution, via time of flight thermometry and photodetachment tomography, respectively. The measured experimental data for a static photodetachment laser beam position are well-represented by the introduced model. However, for a moving laser beam, deviations between the predicted and the measured ion number were observed. This additional loss is attributed to an energy-dependent heating rate, identified as ion-ion radio frequency heating. The thermodynamic model was extended by an additional term describing the energy gain per ion-ion collision. The mean relative energy gain was measured by a separate measurement, completing the two differential equations of evolution without any fitting parameter. The extended model well-described the observed results for forced evaporative cooling of anions via photodetachment with a far-threshold laser beam.
Since the theoretical model reproduces the data very well, it enables to identify the prospects of this technique. It has been shown, that a runaway evaporation regime can be reached by increasing the photodetachment laser beam

intensity and an accelerated beam movement. A higher photodetachment laser beam intensity improves the evaporation efficiency, and prevents the relative cut-off energy from dropping with inward movement of the laser beam. With cooling of the ions the thermalization rate increases drastically, because the background loss out of the radio frequency trap is negligible. Therefore, the cooling rate can be increased without decreasing the efficiency.
Another future prospect of this technique is the co-trapping of multiple anions. Since in a radio frequency trap it is possible to trap multiple species at the same time, one can sympathetically cool one specie via collisions with the evaporatively cooled other one, e.g. co-trapped O^- and OH^-. The photodetachment threshold of O^- is lower, thus, O^- can be cooled evaporatively, while OH^- is only influenced by Coulomb collisions, not the photodetachment light. The final temperature attained would depend on the laser beam position. Thus, the energy can be varied over a range of multiple orders of magnitude, providing a great deal of control and tunability over the system. This measurement technique is ideal to study temperature dependent reaction dynamics of, in principle, any anion specie interacting with ultracold atoms.

In this thesis, two new approaches for cooling anions were discussed, which pushed the frontiers of interaction of trapped anions with photons and atoms. With consideration of the relevant rates, these techniques can be applied, in principle, to a large variety of anionic species, thus providing vital insights into the field of anion trapping and cooling in rf traps.

BIBLIOGRAPHY

[1] Steven Chu. The manipulation of neutral particles. *Reviews of Modern Physics*, 70(3):685–706, 1998. ISSN 00346861. doi: 10.1103/revmodphys.70.685. URL https://journals.aps.org/rmp/pdf/10.1103/RevModPhys.70.685.

[2] William D. Phillips. Laser cooling and trapping of neutral atoms. *Reviews of Modern Physics*, 70(3):721–741, 1998. ISSN 00346861. doi: 10.1103/revmodphys.70.721. URL https://journals.aps.org/rmp/pdf/10.1103/RevModPhys.70.721.

[3] J J Bollinger, L R Brewer, J C Bergquist, S L Gilbert, W M Itano, and D J Larson. Ion trapping techniques: Laser cooling and sympathetic cooling. *Intense Position Beams*, pages 80–91, 1988. URL http://citeseerx.ist.psu.edu/viewdoc/download?doi=10.1.1.549.5941{&}rep=rep1{&}type=pdf.

[4] E. S. Shuman, J. F. Barry, and D. Demille. Laser cooling of a diatomic molecule. *Nature*, 467(7317):820–823, 2010. ISSN 00280836. doi: 10.1038/nature09443. URL https://www.nature.com/articles/nature09443.pdf.

[5] Immanuel Bloch, Jean Dalibard, and Wilhelm Zwerger. Many-body physics with ultracold gases. *Reviews of Modern Physics*, 80(3):885–964, 2008. ISSN 00346861. doi: 10.1103/RevModPhys.80.885. URL https://journals.aps.org/rmp/pdf/10.1103/RevModPhys.80.885.

[6] Cindy A. Regal, Christopher Ticknor, John L. Bohn, and Deborah S. Jin. Creation of ultracold molecules from a Fermi gas of atoms. *Nature*, 424(6944):47–50, 2003. ISSN 00280836. doi: 10.1038/nature01738. URL https://www.nature.com/articles/nature01738.pdf.

[7] D Jaksch and P Zoller. The cold atom Hubbard toolbox. *Annals of Physics*, 315(1):52–79, 2005. ISSN 0003-4916. doi: https://doi.org/10.1016/j.aop.2004.09.010. URL https://www.sciencedirect.com/science/article/pii/S0003491604001782.

[8] M. J. Edmonds, M. Valiente, G. Juzeliunas, L. Santos, and P. Öhberg. Simulating an interacting gauge theory with ultracold bose gases. *Physical Review Letters*, 110(8):1–5, 2013. ISSN 00319007. doi: 10.1103/PhysRevLett.110.085301. URL https://journals.aps.org/prl/pdf/10.1103/PhysRevLett.110.085301.

[9] T. D. Ladd, F. Jelezko, R. Laflamme, Y. Nakamura, C. Monroe, and J. L. O'Brien. Quantum computers. *Nature*, 464(7285):45–53, 2010. ISSN

00280836. doi: 10.1038/nature08812. URL https://www.nature.com/articles/nature08812.pdf.

[10] M. C. McCarthy, C. A. Gottlieb, H. Gupta, and P. Thaddeus. Laboratory and Astronomical Identification of the Negative Molecular Ion C 6 H -. *The Astrophysical Journal*, 652(2):L141–L144, 2006. ISSN 0004-637X. doi: 10.1086/510238. URL https://iopscience.iop.org/article/10.1086/510238/pdf.

[11] A J Coates, F J Crary, G R Lewis, D T Young, J H Waite Jr., and E C Sittler Jr. Discovery of heavy negative ions in Titan's ionosphere. *Geophysical Research Letters*, 34(22), 2007. doi: https://doi.org/10.1029/2007GL030978. URL https://agupubs.onlinelibrary.wiley.com/doi/abs/10.1029/2007GL030978.

[12] M. A. Cordiner, S. B. Charnley, J. V. Buckle, C. Walsh, and T. J. Millar. Discovery of interstellar anions in Cepheus and Auriga. *Astrophysical Journal Letters*, 730(2 PART II):2–6, 2011. ISSN 20418213. doi: 10.1088/2041-8205/730/2/L18. URL https://iopscience.iop.org/article/10.1088/2041-8205/730/2/L18/pdf.

[13] M. Larsson, W. D. Geppert, and G. Nyman. Ion chemistry in space. *Reports on Progress in Physics*, 75(6), 2012. ISSN 00344885. doi: 10.1088/0034-4885/75/6/066901. URL https://iopscience.iop.org/article/10.1088/0034-4885/75/6/066901/pdf.

[14] Thomas J. Millar, Catherine Walsh, and Thomas A. Field. Negative ions in space. *Chemical Reviews*, 117(3):1765–1795, 2017. ISSN 15206890. doi: 10.1021/acs.chemrev.6b00480. URL https://pubs.acs.org/doi/pdf/10.1021/acs.chemrev.6b00480.

[15] D. McElroy, C. Walsh, A. J. Markwick, M. A. Cordiner, K. Smith, and T. J. Millar. The UMIST database for astrochemistry 2012. *Astronomy and Astrophysics*, 550:1–13, 2013. ISSN 14320746. doi: 10.1051/0004-6361/201220465. URL https://www.aanda.org/articles/aa/pdf/2013/02/aa20465-12.pdf.

[16] V. Wakelam, J. C. Loison, E. Herbst, B. Pavone, A. Bergeat, K. Béroff, M. Chabot, A. Faure, D. Galli, W. D. Geppert, D. Gerlich, P. Gratier, N. Harada, K. M. Hickson, P. Honvault, S. J. Klippenstein, S. D.Le Picard, G. Nyman, M. Ruaud, S. Schlemmer, I. R. Sims, D. Talbi, J. Tennyson, and R. Wester. The 2014 kida network for interstellar chemistry. *Astrophysical Journal, Supplement Series*, 217(2), 2015. ISSN 00670049. doi: 10.1088/0067-0049/217/2/20. URL https://arxiv.org/pdf/1503.01594.pdf.

[17] Björn Bastian, Tim Michaelsen, Jennifer Meyer, and Roland Wester. Anionic Carbon Chain Growth in Reactions of C2-,C4-,C6-, C2H- , C4H- , and C6H- with C2H2. *The Astrophysical Journal*, 878(2):162, 2019. ISSN 1538-4357. doi: 10.3847/1538-4357/ab2042. URL http://dx.doi.org/10.3847/1538-4357/ab2042.

[18] H Kreckel, H Bruhns, M Čížek, S C O Glover, K A Miller, X Urbain, and D W Savin. Experimental Results for H2 Formation from H- and H and Implications for First Star Formation. *Science*, 329(5987):69 LP – 71, jul 2010. doi: 10.1126/science.1187191. URL http://science.sciencemag.org/content/329/5987/69.abstract.

[19] Dieter Gerlich, Pavol Jusko, Štěpán Roučka, Illia Zymak, Radek Plašil, and Juraj Glosík. Ion trap studies of H- + H -> H2 + e - Between 10 and 135 K. *Astrophysical Journal*, 749(1), 2012. ISSN 15384357. doi: 10.1088/0004-637X/749/1/22. URL https://iopscience.iop.org/article/10.1088/0004-637X/749/1/22/pdf.

[20] R. Otto, J. Mikosch, S. Trippel, M. Weidemüller, and R. Wester. Nonstandard behavior of a negative ion reaction at very low temperatures. *Physical Review Letters*, 101(6):1–4, 2008. ISSN 00319007. doi: 10.1103/PhysRevLett.101.063201. URL https://journals.aps.org/prl/pdf/10.1103/PhysRevLett.101.063201.

[21] F. A. Gianturco, E. Yurtsever, M. Satta, and R. Wester. Modeling Ionic Reactions at Interstellar Temperatures: The Case of NH 2 -+ H2 <-> NH3 + H-. *Journal of Physical Chemistry A*, 123(46):9905–9918, 2019. ISSN 15205215. doi: 10.1021/acs.jpca.9b07317. URL https://pubs.acs.org/doi/pdf/10.1021/acs.jpca.9b07317.

[22] S. S. Kumar, D. Hauser, R. Jindra, T. Best, Š Roučka, W. D. Geppert, T. J. Millar, and R. Wester. Photodetachment as a destruction mechanism for CN- and C 3N- anions in circumstellar envelopes. *Astrophysical Journal*, 776(1):4–9, 2013. ISSN 15384357. doi: 10.1088/0004-637X/776/1/25. URL https://iopscience.iop.org/article/10.1088/0004-637X/776/1/25/pdf.

[23] Robert E. Continetti and Hua Guo. Dynamics of transient species: Via anion photodetachment. *Chemical Society Reviews*, 46(24):7650–7667, 2017. ISSN 14604744. doi: 10.1039/c7cs00684e. URL https://pubs.rsc.org/en/content/articlepdf/2017/cs/c7cs00684e.

[24] Malcolm Simpson, Markus Nötzold, Alice Schmidt-May, Tim Michaelsen, Björn Bastian, Jennifer Meyer, Robert Wild, Franco A. Gianturco, Milan Milovanović, Viatcheslav Kokoouline, and Roland Wester. Threshold photodetachment spectroscopy of the astrochemical anion CN-. *Journal of Chemical Physics*, 153(18), 2020. ISSN 10897690. doi: 10.1063/5.0029841. URL https://doi.org/10.1063/5.0029841https://aip.scitation.org/doi/pdf/10.1063/5.0029841.

[25] Rico Otto, Alexander Von Zastrow, Thorsten Best, and Roland Wester. Internal state thermometry of cold trapped molecular anions. *Physical Chemistry Chemical Physics*, 15(2):612–618, 2013. ISSN 14639076. doi: 10.1039/c2cp43186f. URL https://pubs.rsc.org/en/content/articlepdf/2013/cp/c2cp43186f.

[26] Daniel Hauser, Seunghyun Lee, Fabio Carelli, Steffen Spieler, Olga Lakhmanskaya, Eric S. Endres, Sunil S. Kumar, Franco Gianturco, and Roland Wester. Rotational state-changing cold collisions of hydroxyl ions with helium. *Nature Physics*, 11(6):467–470, 2015. ISSN 17452481. doi: 10.1038/nphys3326. URL https://www.nature.com/articles/nphys3326.pdf.

[27] C. Meyer, A. Becker, K. Blaum, C. Breitenfeldt, S. George, J. Göck, M. Grieser, F. Grussie, E. A. Guerin, R. Von Hahn, P. Herwig, C. Krantz, H. Kreckel, J. Lion, S. Lohmann, P. M. Mishra, O. Novotný, A. P. O'Connor, R. Repnow, S. Saurabh, D. Schwalm, L. Schweikhard, K. Spruck, S. Sunil Kumar, S. Vogel, and A. Wolf. Radiative Rotational Lifetimes and State-Resolved Relative Detachment Cross Sections from Photodetachment Thermometry of Molecular Anions in a Cryogenic Storage Ring. *Physical Review Letters*, 119(2):1–5, 2017. ISSN 10797114. doi: 10.1103/PhysRevLett.119.023202. URL https://journals.aps.org/prl/pdf/10.1103/PhysRevLett.119.023202.

[28] H. T. Schmidt, G. Eklund, K. C. Chartkunchand, E. K. Anderson, M. Kamińska, N. De Ruette, R. D. Thomas, M. K. Kristiansson, M. Gatchell, P. Reinhed, S. Rosén, A. Simonsson, A. Källberg, P. Löfgren, S. Mannervik, H. Zettergren, and H. Cederquist. Rotationally Cold OH- Ions in the Cryogenic Electrostatic Ion-Beam Storage Ring DESIREE. *Physical Review Letters*, 119(7):1–5, 2017. ISSN 10797114. doi: 10.1103/PhysRevLett.119.073001. URL https://journals.aps.org/prl/pdf/10.1103/PhysRevLett.119.073001.

[29] C. W. Walter, N. D. Gibson, D. J. Matyas, C. Crocker, K. A. Dungan, B. R. Matola, and J. Rohlén. Candidate for laser cooling of a negative ion: Observations of bound-bound transitions in la. *Physical Review Letters*, 113(6):1–5, 2014. ISSN 10797114. doi: 10.1103/PhysRevLett.113.063001. URL https://journals.aps.org/prl/pdf/10.1103/PhysRevLett.113.063001.

[30] G. Cerchiari, A. Kellerbauer, M. S. Safronova, U. I. Safronova, and P. Yzombard. Ultracold Anions for High-Precision Antihydrogen Experiments. *Physical Review Letters*, 120(13):133205, 2018. ISSN 10797114. doi: 10.1103/PhysRevLett.120.133205. URL https://doi.org/10.1103/PhysRevLett.120.133205.

[31] Pauline Yzombard, Mehdi Hamamda, Sebastian Gerber, Michael Doser, and Daniel Comparat. Laser cooling of molecular anions. *Physical Review Letters*, 114(21):1–5, 2015. ISSN 10797114. doi: 10.1103/PhysRevLett.114.213001. URL https://journals.aps.org/prl/pdf/10.1103/PhysRevLett.114.213001.

[32] Sebastian Gerber, Julian Fesel, Michael Doser, and Daniel Comparat. Photodetachment and Doppler laser cooling of anionic molecules. *New Journal of Physics*, 20(2), 2018. ISSN 13672630. doi: 10.1088/

1367-2630/aaa951. URL https://iopscience.iop.org/article/10.1088/1367-2630/aaa951/pdf.

[33] M. Amoretti, C. Amsler, G. Bonomi, A. Bouchta, P. Bowe, C. Carraro, C. L. Cesar, M. Chaliton, M. J.T. Collier, M. Doser, V. Filippini, F. S. Fine, A. Fontana, M. C. Fujiwara, R. Funakoshi, P. Genova, J. S. Hangst, R. S. Hayano, M. H. Holzscheiter, L. V. Jørgensen, V. Lagomarsino, R. Landua, D. Lindelöf, E. Lodi Rizzini, M. Macrì, N. Madsen, G. Manuzio, M. Marchesotti, P. Montagna, H. Pruys, C. Regenfus, P. Riedler, J. Rochet, A. Rotondi, G. Rouleau, G. Testera, A. Variola, T. L. Watson, and D. P. Van Der Werf. Production and detection of cold antihydrogen atoms. *Nature*, 419(6906):456–459, 2002. ISSN 00280836. doi: 10.1038/nature01096. URL https://www.nature.com/articles/nature01096.pdf.

[34] G. B. Andresen, M. D. Ashkezari, M. Baquero-Ruiz, W. Bertsche, P. D. Bowe, E. Butler, C. L. Cesar, S. Chapman, M. Charlton, A. Deller, S. Eriksson, J. Fajans, T. Friesen, M. C. Fujiwara, D. R. Gill, A. Gutierrez, J. S. Hangst, W. N. Hardy, M. E. Hayden, A. J. Humphries, R. Hydomako, M. J. Jenkins, S. Jonsell, L. V. Jørgensen, L. Kurchaninov, N. Madsen, S. Menary, P. Nolan, K. Olchanski, A. Olin, A. Povilus, P. Pusa, F. Robicheaux, E. Sarid, S. Seif El Nasr, D. M. Silveira, C. So, J. W. Storey, R. I. Thompson, D. P. Van Der Werf, J. S. Wurtele, and Y. Yamazaki. Trapped antihydrogen. *Nature*, 468(7324):673–676, 2010. ISSN 00280836. doi: 10.1038/nature09610. URL https://www.nature.com/articles/nature09610.pdf.

[35] A Kellerbauer, M Amoretti, A S Belov, G Bonomi, I Boscolo, R S Brusa, M Büchner, V M Byakov, L Cabaret, C Canali, C Carraro, F Castelli, S Cialdi, M de Combarieu, D Comparat, G Consolati, N Djourelov, M Doser, G Drobychev, A Dupasquier, G Ferrari, P Forget, L Formaro, A Gervasini, M G Giammarchi, S N Gninenko, G Gribakin, S D Hogan, M Jacquey, V Lagomarsino, G Manuzio, S Mariazzi, V A Matveev, J O Meier, F Merkt, P Nedelec, M K Oberthaler, P Pari, M Prevedelli, F Quasso, A Rotondi, D Sillou, S V Stepanov, H H Stroke, G Testera, G M Tino, G Trénec, A Vairo, J Vigué, H Walters, U Warring, S Zavatarelli, and D S Zvezhinskij. Proposed antimatter gravity measurement with an antihydrogen beam. *Nuclear Instruments and Methods in Physics Research Section B: Beam Interactions with Materials and Atoms*, 266(3):351–356, 2008. ISSN 0168-583X. doi: https://doi.org/10.1016/j.nimb.2007.12.010. URL https://www.sciencedirect.com/science/article/pii/S0168583X07017740.

[36] Michał Tomza, Krzysztof Jachymski, Rene Gerritsma, Antonio Negretti, Tommaso Calarco, Zbigniew Idziaszek, and Paul S. Julienne. Cold hybrid ion-atom systems. *Reviews of Modern Physics*, 91(3):1–63, 2019. ISSN 15390756. doi: 10.1103/RevModPhys.91.035001. URL https://arxiv.org/pdf/1708.07832.pdf.

[37] Eric R. Hudson. Sympathetic cooling of molecular ions with ultracold atoms. *EPJ Techniques and Instrumentation*, 3(1), 2016. ISSN 2195-7045. doi: 10.1140/epjti/s40485-016-0035-0. URL https://link.springer.com/content/pdf/10.1140/epjti/s40485-016-0035-0.pdf.

[38] D. S. Goodman, I. Sivarajah, J. E. Wells, F. A. Narducci, and W. W. Smith. Ion-neutral-atom sympathetic cooling in a hybrid linear rf Paul and magneto-optical trap. *Physical Review A - Atomic, Molecular, and Optical Physics*, 86(3):1–10, 2012. ISSN 10502947. doi: 10.1103/PhysRevA.86.033408. URL https://journals.aps.org/pra/pdf/10.1103/PhysRevA.86.033408.

[39] K. Ravi, Seunghyun Lee, Arijit Sharma, G. Werth, and S. A. Rangwala. Cooling and stabilization by collisions in a mixed ion-atom system. *Nature Communications*, 3, 2012. ISSN 20411723. doi: 10.1038/ncomms2131. URL https://www.nature.com/articles/ncomms2131.pdf.

[40] I. Sivarajah, D. S. Goodman, J. E. Wells, F. A. Narducci, and W. W. Smith. Evidence of sympathetic cooling of Na+ ions by a Na magneto-optical trap in a hybrid trap. *Physical Review A - Atomic, Molecular, and Optical Physics*, 86(6):1–7, 2012. ISSN 10502947. doi: 10.1103/PhysRevA.86.063419. URL https://journals.aps.org/pra/pdf/10.1103/PhysRevA.86.063419.

[41] Eric R. Hudson. Method for producing ultracold molecular ions. *Physical Review A - Atomic, Molecular, and Optical Physics*, 79(3):1–9, 2009. ISSN 10502947. doi: 10.1103/PhysRevA.79.032716. URL https://journals.aps.org/pra/pdf/10.1103/PhysRevA.79.032716.

[42] Wade G. Rellergert, Scott T. Sullivan, Steven J. Schowalter, Svetlana Kotochigova, Kuang Chen, and Eric R. Hudson. Evidence for sympathetic vibrational cooling of translationally cold molecules. *Nature*, 495 (7442):490–494, 2013. ISSN 00280836. doi: 10.1038/nature11937. URL https://www.nature.com/articles/nature11937.pdf.

[43] Andrew T. Grier, Marko Cetina, Fedja Oručević, and Vladan Vuletić. Observation of cold collisions between trapped ions and trapped atoms. *Physical Review Letters*, 102(22):1–4, 2009. ISSN 00319007. doi: 10.1103/PhysRevLett.102.223201. URL https://journals.aps.org/prl/pdf/10.1103/PhysRevLett.102.223201.

[44] Felix H.J. Hall and Stefan Willitsch. Millikelvin reactive collisions between sympathetically cooled molecular ions and laser-cooled atoms in an ion-atom hybrid trap. *Physical Review Letters*, 109(23):3–7, 2012. ISSN 00319007. doi: 10.1103/PhysRevLett.109.233202. URL https://journals.aps.org/prl/pdf/10.1103/PhysRevLett.109.233202.

[45] Prateek Puri, Michael Mills, Christian Schneider, Ionel Simbotin, John A. Montgomery, Robin Côté, Arthur G. Suits, and Eric R. Hudson. Synthesis of mixed hypermetallic oxide BaOCa+ from laser-cooled reagents in an

atom-ion hybrid trap. *Science*, 357(6358):1370–1375, 2017. ISSN 10959203. doi: 10.1126/science.aan4701. URL https://science.sciencemag.org/content/357/6358/1370/tab-pdf.

[46] Prateek Puri, Michael Mills, Ionel Simbotin, John A. Montgomery, Robin Côté, Christian Schneider, Arthur G. Suits, and Eric R. Hudson. Reaction blockading in a reaction between an excited atom and a charged molecule at low collision energy. *Nature Chemistry*, 11(7): 615–621, 2019. ISSN 17554349. doi: 10.1038/s41557-019-0264-3. URL https://www.nature.com/articles/s41557-019-0264-3.pdf.

[47] J. Deiglmayr, A. Göritz, T. Best, M. Weidemüller, and R. Wester. Reactive collisions of trapped anions with ultracold atoms. *Physical Review A - Atomic, Molecular, and Optical Physics*, 86(4):1–4, 2012. ISSN 10502947. doi: 10.1103/PhysRevA.86.043438. URL https://journals.aps.org/pra/pdf/10.1103/PhysRevA.86.043438.

[48] Bastian Höltkemeier, Pascal Weckesser, Henry López-Carrera, and Matthias Weidemüller. Dynamics of a single trapped ion immersed in a buffer gas. *Physical Review A*, 94(6):1–10, 2016. ISSN 24699934. doi: 10.1103/PhysRevA.94.062703. URL https://journals.aps.org/pra/pdf/10.1103/PhysRevA.94.062703.

[49] Bastian Höltkemeier, Pascal Weckesser, Henry López-Carrera, and Matthias Weidemüller. Buffer-Gas Cooling of a Single Ion in a Multipole Radio Frequency Trap beyond the Critical Mass Ratio. *Physical Review Letters*, 116(23):1–5, 2016. ISSN 10797114. doi: 10.1103/PhysRevLett.116.233003. URL https://journals.aps.org/prl/pdf/10.1103/PhysRevLett.116.233003.

[50] Kuang Chen, Scott T Sullivan, and Eric R Hudson. Neutral Gas Sympathetic Cooling of an Ion in a Paul Trap. *Phys. Rev. Lett.*, 112 (14):143009, apr 2014. doi: 10.1103/PhysRevLett.112.143009. URL https://link.aps.org/doi/10.1103/PhysRevLett.112.143009.

[51] I. Rouse and S. Willitsch. Superstatistical Energy Distributions of an Ion in an Ultracold Buffer Gas. *Physical Review Letters*, 118(14):1–6, 2017. ISSN 10797114. doi: 10.1103/PhysRevLett.118.143401. URL https://journals.aps.org/prl/pdf/10.1103/PhysRevLett.118.143401.

[52] Ziv Meir, Tomas Sikorsky, Ruti Ben-Shlomi, Nitzan Akerman, Yehonatan Dallal, and Roee Ozeri. Dynamics of a Ground-State Cooled Ion Colliding with Ultracold Atoms. *Physical Review Letters*, 117(24):1–5, 2016. ISSN 10797114. doi: 10.1103/PhysRevLett.117.243401. URL https://journals.aps.org/prl/pdf/10.1103/PhysRevLett.117.243401.

[53] Ziv Meir, Meirav Pinkas, Tomas Sikorsky, Ruti Ben-Shlomi, Nitzan Akerman, and Roee Ozeri. Direct Observation of Atom-Ion Nonequilibrium Sympathetic Cooling. *Physical Review Letters*, 121(5):53402,

2018. ISSN 10797114. doi: 10.1103/PhysRevLett.121.053402. URL https://doi.org/10.1103/PhysRevLett.121.053402.

[54] Anne Crubellier. Theory of laser evaporative cooling of trapped negative ions. I. Harmonically bound ions and RF traps. *Journal of Physics B: Atomic, Molecular and Optical Physics*, 23(20):3585–3607, 1990. ISSN 13616455. doi: 10.1088/0953-4075/23/20/020. URL https://iopscience.iop.org/article/10.1088/0953-4075/23/20/020/pdf.

[55] J. Mikosch, U. Frühling, S. Trippel, D. Schwalm, M. Weidemüller, and R. Wester. Evaporation of Buffer-gas-thermalized anions out of a multipole rf ion trap. *Physical Review Letters*, 98(22):4–7, 2007. ISSN 00319007. doi: 10.1103/PhysRevLett.98.223001. URL https://journals.aps.org/prl/pdf/10.1103/PhysRevLett.98.223001.

[56] G. B. Andresen, M. D. Ashkezari, M. Baquero-Ruiz, W. Bertsche, P. D. Bowe, E. Butler, C. L. Cesar, S. Chapman, M. Charlton, J. Fajans, T. Friesen, M. C. Fujiwara, D. R. Gill, J. S. Hangst, W. N. Hardy, R. S. Hayano, M. E. Hayden, A. Humphries, R. Hydomako, S. Jonsell, L. Kurchaninov, R. Lambo, N. Madsen, S. Menary, P. Nolan, K. Olchanski, A. Olin, A. Povilus, P. Pusa, F. Robicheaux, E. Sarid, D. M. Silveira, C. So, J. W. Storey, R. I. Thompson, D. P. Van Der Werf, D. Wilding, J. S. Wurtele, and Y. Yamazaki. Evaporative cooling of antiprotons to cryogenic temperatures. *Physical Review Letters*, 105(1):1–5, 2010. ISSN 00319007. doi: 10.1103/PhysRevLett.105.013003. URL https://journals.aps.org/prl/pdf/10.1103/PhysRevLett.105.013003.

[57] G. Cerchiari, P. Yzombard, and A. Kellerbauer. Laser-Assisted Evaporative Cooling of Anions. *Physical Review Letters*, 123(10):103201, 2019. ISSN 10797114. doi: 10.1103/PhysRevLett.123.103201. URL https://journals.aps.org/prl/pdf/10.1103/PhysRevLett.123.103201.

[58] Markus Nötzold, Saba Zia Hassan, Jonas Tauch, Eric Endres, Roland Wester, and Matthias Weidemüller. Thermometry in a Multipole Ion Trap. *Applied Sciences*, 10(15):5264, jul 2020. ISSN 2076-3417. doi: 10.3390/app10155264. URL https://www.mdpi.com/2076-3417/10/15/5264.

[59] H G Dehmelt. Radiofrequency Spectroscopy of Stored Ions I. In D R Bates and Immanuel Estermann, editors, *Advances in Atomic and Molecular Physics*, volume 3 of *Advances in Atomic and Molecular Physics*, pages 53–72. Academic Press, 1968. doi: https://doi.org/10.1016/S0065-2199(08)60170-0. URL http://www.sciencedirect.com/science/article/pii/S0065219908601700.

[60] F M Penning. Die glimmentladung bei niedrigem druck zwischen koaxialen zylindern in einem axialen magnetfeld. *Physica*, 3(9):873–894, 1936. ISSN 0031-8914. doi: https://doi.org/10.1016/S0031-8914(36)80313-9. URL http://www.sciencedirect.com/science/article/pii/S0031891436803139.

[61] Wolfgang Paul. Electromagnetic Traps for Charged and Neutral Particles (Nobel Lecture). *Angewandte Chemie International Edition in English*, 29 (7):739–748, 1990. ISSN 15213773. doi: 10.1002/anie.199007391. URL https://journals.aps.org/rmp/pdf/10.1103/RevModPhys.62.531.

[62] Dieter Gerlich. *Inhomogeneous RF Fields: A Versatile Tool for the Study of Processes with Slow Ions*, pages 1–176. John Wiley & Sons, Ltd, 1992. ISBN 9780470141397. doi: https://doi.org/10.1002/9780470141397.ch1. URL https://onlinelibrary.wiley.com/doi/abs/10.1002/9780470141397.ch1.

[63] E Teloy and D Gerlich. Integral cross sections for ion-molecule reactions. I. The guided beam technique. *Chemical Physics*, 4(3):417–427, 1974. ISSN 0301-0104. doi: https://doi.org/10.1016/0301-0104(74)85008-1. URL http://www.sciencedirect.com/science/article/pii/0301010474850081.

[64] Dieter Gerlich. Ion-neutral collisions in a 22-pole trap at very low energies. *Physica Scripta*, 1995(T59):256–263, 1995. ISSN 14024896. doi: 10.1088/0031-8949/1995/T59/035. URL https://iopscience.iop.org/article/10.1088/0031-8949/1995/T59/035/pdf.

[65] David L. Osborn, David J. Leahy, Douglas R. Cyr, and Daniel M. Neumark. Photodissociation spectroscopy and dynamics of the N2O2- anion. *Journal of Chemical Physics*, 104(13):5026–5039, 1996. ISSN 00219606. doi: 10.1063/1.471132. URL https://aip.scitation.org/doi/pdf/10.1063/1.471132.

[66] Christian Greve. *Creation of charged water clusters and storage in a biplanar rf multipole ion trap*. Master thesis, Universität Freiburg, 2009.

[67] Henry López-Carrera. *Sympathetic cooling and rotational quenching of molecular anions in a hybrid atom ion trap*. Phd thesis, Universität Heidelberg, 2018. URL http://archiv.ub.uni-heidelberg.de/volltextserver/25225/.

[68] Nina Beier. *A versatile anion source for studying atom-ion collisions*. Bachelor thesis, Universität Heidelberg, 2017.

[69] Michael L Alexander, Nancy E Levinger, M A Johnson, Douglas Ray, and W C Lineberger. Recombination of Br-2 photodissociated within mass selected ionic clusters. *The Journal of Chemical Physics*, 88(10):6200–6210, may 1988. ISSN 0021-9606. doi: 10.1063/1.454458. URL https://doi.org/10.1063/1.454458.

[70] Stefan Felix Paul. *Optimization of the Ion Storage in a Hybrid Atom-Ion-Trap*. Bachelor thesis, Universität Heidelberg, 2015.

[71] Rico Otto. *Dynamics of a Microsolvated Ion-Molecule Reaction*. Phd thesis, Universität Freiburg, 2011. URL https://freidok.uni-freiburg.de/data/8342.

[72] Jan Trautmann. *Manipulating Hydroxyl Anions - Hydration and Rotational Cooling*. Master thesis, Universität Heidelberg, 2018.

[73] W. C. Wiley and I. H. McLaren. Time-of-flight mass spectrometer with improved resolution. *Review of Scientific Instruments*, 26(12):1150–1157, 1955. ISSN 00346748. doi: 10.1063/1.1715212. URL https://aip.scitation.org/doi/pdf/10.1063/1.1715212.

[74] Oskar Asvany and Stephan Schlemmer. Numerical simulations of kinetic ion temperature in a cryogenic linear multipole trap. *International Journal of Mass Spectrometry*, 279(2):147–155, 2009. ISSN 1387-3806. doi: https://doi.org/10.1016/j.ijms.2008.10.022. URL http://www.sciencedirect.com/science/article/pii/S1387380608004338.

[75] Lewis M. Branscomb, David S. Burch, Stephen J. Smith, and Sydney Geltman. Photodetachment cross section and the electron affinity of atomic oxygen. *Physical Review*, 111(2):504–513, 1958. ISSN 0031899X. doi: 10.1103/PhysRev.111.504. URL https://journals.aps.org/pr/pdf/10.1103/PhysRev.111.504.

[76] Lewis M. Branscomb. Photodetachment cross section, electron affinity, and structure of the negative hydroxyl ion. *Physical Review*, 148(1):11–18, 1966. ISSN 0031899X. doi: 10.1103/PhysRev.148.11. URL https://journals.aps.org/pr/pdf/10.1103/PhysRev.148.11.

[77] H. Hotop, T. A. Patterson, and W. C. Lineberger. High-resolution photodetachment study of Se- ions. *Physical Review A*, 8(2):762–774, 1973. ISSN 10502947. doi: 10.1103/PhysRevA.8.762. URL https://journals.aps.org/pra/pdf/10.1103/PhysRevA.8.762.

[78] S. Trippel, J. Mikosch, R. Berhane, R. Otto, M. Weidemüller, and R. Wester. Photodetachment of cold OH- in a multipole ion trap. *Physical Review Letters*, 97(19):1–4, 2006. ISSN 00319007. doi: 10.1103/PhysRevLett.97.193003. URL https://journals.aps.org/prl/pdf/10.1103/PhysRevLett.97.193003.

[79] NIST Webbook chemistry SRD 69, 2021. URL https://webbook.nist.gov/chemistry/.

[80] Lyman Spitzer. *Physics of fully ionized gases*. Interscience Publ., New York, 2. edition edition, 1967.

[81] Simone Götz. *A high density target of ultracold atoms and momentum resolved measurements of ion-atom collisions*. Phd thesis, Universität Heidelberg, 2012. URL https://archiv.ub.uni-heidelberg.de/volltextserver/13352/.

[82] Julian Glässel. *Saturation absorption imaging of a high-density rubidium dark spot*. Master thesis, Universität Heidelberg, 2014.

[83] Bastian Höltkemeier, Julian Glässel, Henry López-Carrera, and Matthias Weidemüller. A dense gas of laser-cooled atoms for hybrid atom-ion trapping. *Applied Physics B*, 123(1):51, 2017. ISSN 1432-0649. doi: 10.1007/s00340-016-6624-4. URL https://doi.org/10.1007/s00340-016-6624-4.

[84] Bastian Höltkemeier. *Sympathetic cooling of ions in a hybrid atom ion trap*. Phd thesis, Universität Heidelberg, 2016. URL https://archiv.ub.uni-heidelberg.de/volltextserver/22096/.

[85] Wolfgang Ketterle, Kendall B. Davis, Michael A. Joffe, Alex Martin, and David E. Pritchard. High densities of cold atoms in a dark spontaneous-force optical trap. *Physical Review Letters*, 70(15):2253–2256, 1993. ISSN 00319007. doi: 10.1103/PhysRevLett.70.2253. URL https://journals.aps.org/prl/pdf/10.1103/PhysRevLett.70.2253.

[86] Bastian Höltkemeier. *2D MOT as a source of a cold atom target*. Diploma thesis, Universität Heidelberg, 2011.

[87] H J Metcalf and P van der Straten. *Laser Cooling and Trapping*. Graduate Texts in Contemporary Physics. Springer New York, 2001. ISBN 9780387987286. URL https://books.google.de/books?id=i-40VaXqrj0C.

[88] F Carelli, F A Gianturco, and R Wester. Collisional state-changing of OH-rotations by interaction with Rb atoms in cold traps. *Chemical Physics*, 462:111–118, 2015. URL https://doi.org/10.1016/j.chemphys.2015.05.027.

[89] P. Langevin. Une formule fondamentale de théorie cinétique. *annales de chimie et de physique*, 5:245, 1905. URL https://gallica.bnf.fr/ark:/12148/bpt6k34935p/f242.item.texteImage.

[90] R Côté and A Dalgarno. Ultracold atom-ion collisions. *Phys. Rev. A*, 62(1):12709, jun 2000. doi: 10.1103/PhysRevA.62.012709. URL https://link.aps.org/doi/10.1103/PhysRevA.62.012709.

[91] Wolfgang Ketterle and N J Van Druten. *Evaporative Cooling of Trapped Atoms*, volume 37. Academic Press, 1996. ISBN 1049-250X. doi: https://doi.org/10.1016/S1049-250X(08)60101-9. URL https://www.sciencedirect.com/science/article/pii/S1049250X08601019.

[92] B. M. Penetrante, J. N. Bardsley, M. A. Levine, D. A. Knapp, and R. E. Marrs. Evaporative cooling of highly charged dysprosium ions in an enhanced electron-beam ion trap. *Physical Review A*, 43(9):4873–4882, 1991. ISSN 10502947. doi: 10.1103/PhysRevA.43.4873. URL https://journals.aps.org/pra/pdf/10.1103/PhysRevA.43.4873.

[93] W Fundamenski and O E Garcia. Comparison of Coulomb Collision Rates in the Plasma Physics and Magnetically Confined Fusion Litera-

ture. *Efda-Jet Report*, 00(07), 2007. URL https://scipub.euro-fusion.org/wp-content/uploads/2014/11/EFDR07001.pdf.

[94] P. Hlavenka, R. Otto, S. Trippel, J. Mikosch, M. Weidemüller, and R. Wester. Absolute photodetachment cross section measurements of the O- and OH- anion. *Journal of Chemical Physics*, 130(6), 2009. ISSN 00219606. doi: 10.1063/1.3080809. URL https://aip.scitation.org/doi/pdf/10.1063/1.3080809.

[95] T. Baba and I. Waki. Sympathetic cooling rate of gas-phase ions in a radio-frequency-quadrupole ion trap. *Applied Physics B: Lasers and Optics*, 74(4-5):375–382, 2002. ISSN 09462171. doi: 10.1007/s003400200829. URL https://link.springer.com/content/pdf/10.1007/s003400200829.pdf.

[96] Steven J. Schowalter, Alexander J. Dunning, Kuang Chen, Prateek Puri, Christian Schneider, and Eric R. Hudson. Blue-sky bifurcation of ion energies and the limits of neutral-gas sympathetic cooling of trapped ions. *Nature Communications*, 7, 2016. ISSN 20411723. doi: 10.1038/ncomms12448. URL https://www.nature.com/articles/ncomms12448.pdf.

[97] Setsuo Ichimaru and Shigenori Tanaka. Generalized viscoelastic theory of the glass transition for strongly coupled, classical, one-component plasmas. *Physical Review Letters*, 56(26):2815–2818, 1986. ISSN 00319007. doi: 10.1103/PhysRevLett.56.2815. URL https://journals.aps.org/prl/pdf/10.1103/PhysRevLett.56.2815.

[98] S. L. Gilbert, J. J. Bollinger, and D. J. Wineland. Shell-structure phase of magnetically confined strongly coupled plasmas. *Physical Review Letters*, 60(20):2022–2025, 1988. ISSN 00319007. doi: 10.1103/PhysRevLett.60.2022. URL https://journals.aps.org/prl/pdf/10.1103/PhysRevLett.60.2022.

[99] K. B. Davis, M. O. Mewes, and W. Ketterle. An analytical model for evaporative cooling of atoms. *Applied Physics B Laser and Optics*, 60 (2-3):155–159, 1995. ISSN 09462171. doi: 10.1007/BF01135857. URL https://link.springer.com/content/pdf/10.1007/BF01135857.pdf.

[100] D. J. Larson, J. C. Bergquist, J. J. Bollinger, Wayne M. Itano, and D. J. Wineland. Sympathetic cooling of trapped ions: A laser-cooled two-species nonneutral ion plasma. *Physical Review Letters*, 57(1):70–73, 1986. ISSN 00319007. doi: 10.1103/PhysRevLett.57.70. URL https://journals.aps.org/prl/pdf/10.1103/PhysRevLett.57.70.

[101] C. J. Myatt, E. A. Burt, R. W. Christ, E. A. Cornell, and C. E. Wieman. Production of two verlapping bose-einstein condensates by sympathetic cooling. *Collected Papers of Carl Wieman*, pages 489–492, 2008. doi: 10.1142/9789812813787_0066. URL https://journals.aps.org/prl/pdf/10.1103/PhysRevLett.78.586.

[102] Wade G Rellergert, Scott T Sullivan, Steven J Schowalter, Svetlana Kotochigova, Kuang Chen, and Eric R Hudson. Evidence for sympathetic vibrational cooling of translationally cold molecules. *Nature*, 495 (7442):490–494, 2013. ISSN 1476-4687. doi: 10.1038/nature11937. URL https://doi.org/10.1038/nature11937.

[103] Ralph G DeVoe. Power-Law Distributions for a Trapped Ion Interacting with a Classical Buffer Gas. *Phys. Rev. Lett.*, 102(6):63001, feb 2009. doi: 10.1103/PhysRevLett.102.063001. URL https://link.aps.org/doi/10.1103/PhysRevLett.102.063001.

[104] Pascal M. Weckesser. *Sympathetic cooling of ions in radio frequency traps*. Master thesis, Universität Heidelberg, 2015.

[105] Christoph Zipkes, Lothar Ratschbacher, Carlo Sias, and Michael Kohl. Kinetics of a single trapped ion in an ultracold buffer gas. *New Journal of Physics*, 13, 2011. ISSN 13672630. doi: 10.1088/1367-2630/13/5/053020. URL https://iopscience.iop.org/article/10.1088/1367-2630/13/5/053020/pdf.

[106] Milaim Kas, Jérôme Loreau, Jacques Liévin, and Nathalie Vaeck. Ab initio study of reactive collisions between Rb(2 S) or Rb(2 P) and OH-(1Σ+). *Journal of Chemical Physics*, 144(20), 2016. ISSN 00219606. doi: 10.1063/1.4950784. URL http://dx.doi.org/10.1063/1.4950784.

[107] Milaim Kas, Jérôme Loreau, Jacques Liévin, and Nathalie Vaeck. Ab initio study of the neutral and anionic alkali and alkaline earth hydroxides: Electronic structure and prospects for sympathetic cooling of OH-. *Journal of Chemical Physics*, 146(19), 2017. ISSN 00219606. doi: 10.1063/1.4983627. URL https://aip.scitation.org/doi/pdf/10.1063/1.4983627.

[108] Benjamin Mintz, Bun Chan, Michael B Sullivan, Thomas Buesgen, Anthony P Scott, Steven R Kass, Leo Radom, and Angela K Wilson. Structures and Thermochemistry of the Alkali Metal Monoxide Anions, Monoxide Radicals, and Hydroxides. *The Journal of Physical Chemistry A*, 113(34):9501–9510, aug 2009. ISSN 1089-5639. doi: 10.1021/jp9034826. URL https://doi.org/10.1021/jp9034826.

[109] F G Major and H G Dehmelt. Exchange-Collision Technique for the rf Spectroscopy of Stored Ions. *Phys. Rev.*, 170(1):91–107, jun 1968. doi: 10.1103/PhysRev.170.91. URL https://link.aps.org/doi/10.1103/PhysRev.170.91.

[110] Marko Cetina, Andrew T Grier, and Vladan Vuleti\ifmmode \acutec\else ć\fi. Micromotion-Induced Limit to Atom-Ion Sympathetic Cooling in Paul Traps. *Phys. Rev. Lett.*, 109(25):253201, 2012. doi: 10.1103/PhysRevLett.109.253201. URL https://link.aps.org/doi/10.1103/PhysRevLett.109.253201.

[111] E S Endres, G Egger, S Lee, O Lakhmanskaya, M Simpson, and R Wester. Incomplete rotational cooling in a 22-pole ion trap. *Journal of Molecular Spectroscopy*, 332:134–138, 2017. ISSN 0022-2852. doi: https://doi.org/10.1016/j.jms.2016.12.006. URL https://www.sciencedirect.com/science/article/pii/S0022285216303629.

[112] Shinsuke Haze, Mizuki Sasakawa, Ryoichi Saito, Ryosuke Nakai, and Takashi Mukaiyama. Cooling Dynamics of a Single Trapped Ion via Elastic Collisions with Small-Mass Atoms. *Phys. Rev. Lett.*, 120(4):43401, jan 2018. doi: 10.1103/PhysRevLett.120.043401. URL https://link.aps.org/doi/10.1103/PhysRevLett.120.043401.

[113] Christoph Zipkes, Stefan Palzer, Carlo Sias, and Michael Köhl. A trapped single ion inside a Bose-Einstein condensate. *Nature*, 464(7287):388–391, 2010. ISSN 00280836. doi: 10.1038/nature08865. URL https://www.nature.com/articles/nature08865.pdf.

[114] Stefan Schmid, Arne Härter, and Johannes Hecker Denschlag. Dynamics of a cold trapped ion in a Bose-Einstein condensate. *Physical Review Letters*, 105(13):1–4, 2010. ISSN 00319007. doi: 10.1103/PhysRevLett.105.133202. URL https://journals.aps.org/prl/pdf/10.1103/PhysRevLett.105.133202.

[115] Sourav Dutta, Rahul Sawant, and S. A. Rangwala. Collisional Cooling of Light Ions by Cotrapped Heavy Atoms. *Physical Review Letters*, 118 (11):1–5, 2017. ISSN 10797114. doi: 10.1103/PhysRevLett.118.113401. URL https://journals.aps.org/prl/pdf/10.1103/PhysRevLett.118.113401.

[116] Malcolm Simpson, Markus Nötzold, Alice Schmidt-May, Tim Michaelsen, Björn Bastian, Jennifer Meyer, Robert Wild, Franco A Gianturco, Milan Milovanović, Viatcheslav Kokoouline, and Roland Wester. Threshold photodetachment spectroscopy of the astrochemical anion CN-. *The Journal of Chemical Physics*, 153(18):184309, nov 2020. ISSN 0021-9606. doi: 10.1063/5.0029841. URL https://doi.org/10.1063/5.0029841.

[117] Olga Lakhmanskaya, Malcolm Simpson, Simon Murauer, Viatcheslav Kokoouline, and Roland Wester. Photodetachment spectroscopy of cold trapped NH 2 - Near threshold. *Journal of Chemical Physics*, 149(10), 2018. ISSN 00219606. doi: 10.1063/1.5042621. URL http://dx.doi.org/10.1063/1.5042621https://aip.scitation.org/doi/pdf/10.1063/1.5042621.

[118] D Gerlich, R Plašil, I Zymak, M Hejduk, P Jusko, D Mulin, and J Glosík. State Specific Stabilization of H+ + H2(j) Collision Complexes. *The Journal of Physical Chemistry A*, 117(39):10068–10075, oct 2013. ISSN 1089-5639. doi: 10.1021/jp400917v. URL https://doi.org/10.1021/jp400917v.

[119] Milaim Kas, Jérôme Loreau, Jacques Liévin, and Nathalie Vaeck. Reactivity of Hydrated Hydroxide Anion Clusters with H and Rb: An

ab Initio Study. *Journal of Physical Chemistry A*, 123(41):8893–8906, 2019. ISSN 15205215. doi: 10.1021/acs.jpca.9b05971. URL https://pubs.acs.org/doi/pdf/10.1021/acs.jpca.9b05971.

[120] Milaim Kas, Jérôme Loreau, Jacques Liévin, and Nathalie Vaeck. Cold reactive and nonreactive collisions of Li and Rb with C2-: Implications for hybrid-trap experiments. *Physical Review A*, 99(4):1–9, 2019. ISSN 24699934. doi: 10.1103/PhysRevA.99.042702. URL https://journals.aps.org/pra/pdf/10.1103/PhysRevA.99.042702.

List of publications covered in this thesis:

- *Thermometry in a Multipole Ion Trap*
  M. Nötzold, S. Z. Hassan, J. Tauch, E. S. Endres, R. Wester, M. Weidemüller
  Applied Sciences, 10(15):5264 (2020)

- *Autodetachment of the dipole bound electron in anion-atom reactions*
  S. Z. Hassan, J. Tauch, M. Kas, M. Nötzold, H. Lopez, E. S. Endres, R. Wester, M. Weidemüller
  (to be submitted)

- *Laser induced forced evaporative cooling of molecular anions to the Kelvin range*
  J. Tauch, S. Z. Hassan, M. Nötzold, E. S. Endres, R. Wester, M. Weidemüller
  (to be submitted)

- *Sympathetic cooling of O^- and OH^- by an ultracold heavy buffer gas*
  J. Tauch, S. Z. Hassan, M. Nötzold, E. S. Endres, R. Wester, M. Weidemüller
  (to be submitted)

ACKNOWLEDGEMENTS

An dieser Stelle möchte ich mich bei allen bedanken, die mich auf meinem Weg zu dieser Doktorarbeit begleitet und unterstützt haben. Nochmal besonders bedanken möchte ich bei:

Als erstes möchte ich mich natürlich bei dir bedanken, Matthias, dass du mir die Möglichkeit gegeben hast so viel zu lernen und zu erleben in dieser Zeit. Du hast mir die Freiheit gegeben mich weiterzuentwickeln und aus meinen eigenen Fehlern zu lernen und meistens hattest du dann doch recht gehabt. Dein Lieblingssatz,*"one day in the library, saves you three weeks in the lab"*, werde ich wohl nie wieder vergessen. Vielen Dank für die Zeit und deine Betreuung.

Ich bedanke mich ganz herzlich bei Ihnen Prof. Dr. Andreas Wolf, dass Sie sich bereit erklärt haben, meine Doktorarbeit zu begutachten.

Ein ganz besonderer Dank geht natürlich an dich Roland, ohne deine Expertise über Ionen und chemische Reaktionen wäre dieses Projekt so nicht möglich gewesen. Durch die engere Zusammenarbeit in den letzten Jahren, haben wir noch einmal einen großen Schritt gemacht. Vielen Dank dafür.

Ein ganz besonderer Dank geht an all meine Kollegen in den letzten Jahren:

I thank you so much Saba! I have a lot of fun working with you together in the Lab, as well as, in the office. I love our discussions about anything, often the project, but almost as often the VfB soap opera and some questions we just let the Radler decide. Thank you for teaching me, in the course of this thesis, how to properly use the word "respectively", after using it 20 times the wrong way. Thank you so much for all your help, especially the last couple of weeks. I have to say, I am amazed by your ambitions and resilience. Each time you say, this plant will survive and then you kill it anyway :). Thank you very much for everything.

Vielen Dank Markus, würde ich sagen, wenn du mir endlich mal das versprochene Bild schicken würdest. Du. Vokuhila! Nein Spaß, ich bin dir sehr dankbar, wie viel Zeit du in das HAITrap Projekt gesteckt hast und mir ungemein geholfen hast. Nach Meetings mit dir, ob vor Ort oder auch via Zoom, hatte man immer einen neuen Ansatz ein Problem zu bewältigen. Ich hoffe, wir sehen uns bald mal wieder, wenn es wieder möglich ist nach Tirol bzw. Heidelberg zu kommen. P.S. Vergiss das Bild nicht!

Bedanken möchte ich mich natürlich auch bei dir Eric. Wir haben so viel Fortschritt erreicht in der Zeit, in der du da warst. Aber wir haben es nur einmal ins Stadion geschafft und dann was für ein Spiel. Wie wir dann einfach mit vier Bier für eine Halbzeit da standen, weil zwei Dumme ein Gedanke :). Die allabendlichen Diskussionen über das Experiment, aber auch das laufende Fußballspiel, habe ich das letzte Jahr schon sehr vermisst.

Vermisst habe ich natürlich auch dich, Henry, und die wortwörtlich crazy Zeit mit dir im Labor. Die beste und spaßigste Zeit war wirklich mit dir im Labor, vielleicht auch ein bisschen weil ich noch nicht in der Verantwortung war :) und vielleicht auch weil ich eigentlich deine Latinomusik gar nicht so schlimm fand, wenn ein Lied nicht den ganzen Tag läuft. Ich danke dir vielmals und habe den größten Respekt vor dir, wie du das zum Schluss alles mit Familie und Doktorarbeit gewuppt hast. Ich hoffe, ich steige demnächst mal in ein Flugzeug Richtung Ecuador.

Vielen Dank Domme. Du stehst immer mit Rat und Tat zur Verfügung und das bei so vielen verschiedenen Themen. Ich finde es so faszinierend, mit wie viel Spaß du dir immer neues Wissen aneignest und deinen eigenen speziellen Karriereweg gehst. Darüber hinaus vielen Dank natürlich auch für all den Spaß neben der Arbeit, niemals vergesse ich deinen und Erics Blick nach dem ersten Bissen des von mir angepriesenen Fischweckens in Rostock.

Bei dir, Milaim, möchte ich mich natürlich auch bedanken. Es war immer genial, wenn du in Heidelberg warst. Du hast mir unglaublich geholfen, die reaktiven Verlust zu verstehen, auch wenn ich lieber von dir gehört hätte, dass OH^- mit dem Grundzustandsrubidium nicht reagiert. Aber so ist die Natur, usually ;). Komm mal wieder vorbei, wenn Sommer ist! Bissle Freibad, bissle Kicken, good old times.

Basti! Zickel? :) Ha, das waren Zeiten. Du gerade fertig und ich erst angefangen. Beide einfach die Freiheit genießen. Ich dank dir, dass du dir am Anfang so viel Zeit genommen hast, mir so viel zu erklären und zu zeigen. Das ganze Labview, Logicbox Gedöhns. Der Ordner "hidden from Labview" gibt's, glaube ich, immer noch auf dem Labor-PC. Was den UPS guy angeht, habe ich leider keine Updates, aber ich werde mich nach der Abgabe mal informieren.

Ich bedanke mich auch ganz herzlich bei allen anderen Mitgliedern der QD Gruppe. Man hat immer ein offenes Ohr für Diskussionen und Hilfe im Labor gefunden. Bei der Werkstatt, die unsere Forschung erst möglich macht und bei dir Claudia, die den ganzen Laden hier am Laufen hält.

Ein großer Dank geht an alle meine Freunde, ob hier in Heidelberg oder inzwischen auch überall verteilt. Vielen Dank Simon und Tobi, für die ein oder andere Diskussion übers Projekt oder vielleicht einfach mal ein ablenkendes Mittagessen in der Mensa. Ich hoffe unsere Wege werden sich noch mehrmals kreuzen. Ganz herzlichen Dank auch an Anne, Nils und Finn. Es hat mir unglaublich geholfen, einfach ab und zu mit euch etwas zu machen, ob es ein Spaziergang war, der gute Danteplatz, die Träume von 60 Millionen im Lotto oder auch der wöchentliche Fernsehabend. Vor allem in Coronazeiten hat das mir unendlich viel bedeutet. Ich bedanke mich auch bei all meinen Freunden, aus Schul- und Studienzeiten. Besonderer Dank auch an die Urlaubscrew. Ich hoffe wir gehen auch in 20 Jahren noch einmal im Jahr gemeinsam in den Urlaub und natürlich jedes Jahr etwas luxuriöser! Vielen Dank für die schöne Zeit neben der Doktorarbeit.

Mella, ich kann kaum in Worte fassen wie dankbar ich dir bin. Du warst mein Rückhalt in diesen Jahren. Jedes Wochenende und jeder Urlaub hat mir immer wieder viel Kraft gegeben. Vor allem bin ich dankbar für dein Verständnis in den letzten Monaten, für die wir uns wohl für den nächsten Kalender was überlegen müssen. Es freut mich, dass das aber in Zukunft kein Problem mehr sein wird. Ich freu mich auf unsere gemeinsame Zukunft und dass wir, wenn wir mal mit der Schwarzwaldbahn fahren, es zusammen tun.

Zu guter Letzt möchte ich mich bei meiner Familie bedanken. Für all die Unterstützung die ich erfahren habe, ob in Mössingen, Dublin, Konstanz und hier in Heidelberg. Ich habe mich immer auf euch verlassen können. Ganz herzlich bedanke ich mich auch bei meinen Omas und Opas, ihr habt mich unglaublich geprägt. Ich bin unfassbar dankbar und kann mir keine bessere Familie vorstellen. Vielen Dank!